Investigations of Internal Mechanical Loss Factors of Test Mass Materials for Interferometric Gravitational Wave Detectors

Peter Howard Sneddon, M. Sci.

Department of Physics and Astronomy,
University of Glasgow

Presented as a thesis for the degree of Ph.D.
in the University of Glasgow, University Avenue,
Glasgow G12 8QQ.

18th November 2001

"Look at that!"

"Yes! An interferometer!"

"What's that?"

"This one's for measuring gravitation waves."

"But we could use it on the time-curve circuits."

- *the Doctor and his companions,* Dr Who - Four To Doomsday

Contents

List of Figures

List of Tables

Acknowledgements

As regards my research work, I would like to thank my supervisors Jim Hough and Norna Robertson for all their guidance and support throughout my time as a member of the Gravitational Waves group, and laterally the Institute for Gravitational Research. Also I thank Geppo Cagnoli and Sheila Rowan without whose help I would not have been able to carry out my work, and Stephen McIntosh for some on the spot advice (such as where not to poke a cable and which button might be appropriate to press and when). Thanks are also due to group technicians Colin Craig and Alan Latta for their help with construction of equipment.

Away from the lab, I'd like to thank the other members of the IGR here in Glasgow for help, suggestions, and for introducing me to the concept of strong coffee. In particular I would like to thank those who have shared my office at various times: thanks to Morag Casey (especially when it came to working out why my computer would suddenly take on a life of its own); to Calum Torrie (without whom I would not have had to answer the phone quite so often); to David Crooks (see the above comment as regards strong coffee); to Mike Perreur-Lloyd (for not giving into Calum's calls to turn the office into a Rangers shrine); to Bryan Barr (for showing me that others can talk to themselves more than I do); and to Eoin Elliffe (for reassuring me that Irishmen are not all comical drunks). (And yes, it was a very big office.)

I would like to thank PPARC for providing the funding for the research that is presented within this thesis.

On a personal note, thanks go too to my Mum and sister for all the usual familial support.

Above all, though, I want to thank my wife Christine. Without her love and support (especially since the wedding itself) I would not have reached this far.

Preface

Chapter One of this thesis discusses the nature, sources and detection methods of gravitational waves. The work has been derived from current literature.

Chapter Two details some aspects of the theory of Thermal Noise: how it can be calculated, how it can be minimised, and how it could affect the search for gravitational waves. This work has been derived from current literature.

Chapter Three explains the experimental arrangements employed in the course of this research. It also deals with the factors that can limit the results recorded. This work is partly compiled from published information, in addition to work performed by the author in conjunction with J. Hough and G. Cagnoli.

Chapter Four gives the results of testing a range of materials that could be used in the construction of future interferometric gravitational wave detectors. This work was performed by the author, in conjunction with G. Cagnoli and S. Rowan.

Chapter Five discusses the effects of applying a dielectric mirror coating to the test substrates on their internal quality factors. The results were then extensively analysed using complex finite element modelling. The experimental results were gathered by the author, and the modelling performed by D. Crooks. Subsequent discussions on both were held between the author, D.

Crooks, G. Cagnoli, S. Rowan and J. Hough.

Chapter Six details investigations into the effect on the quality factors of test masses after they have had additional substrate pieces attached to them by differing bonding techniques. The measured results were obtained by the author, the bonding carried out by the author in conjunction with S. Rowan, J. Hough and E. Elliffe. Initial analysis of results was performed by J. Hough, and then subsequently extended by the author.

Chapter Seven gives the conclusions on the work presented, in addition to some discussion on where the work should go from here.

Appendix A details the electronic feedback systems used to allow measurement of the thermal fluctuations on the face of the test masses.

Appendix B details the data acquisition techniques used to record the decaying ringdowns of excitations that lead to the quality factors.

Appendix C details the Algor method of finite element analysis and mode shapes of relevance to the work in Chapter 5.

Appendix D discusses briefly some aspects of strain energy in relation to work in Chapter 5.

Appendix E details the methods used to create fused silica fibres as used in relation to work presented and discussed in Chapter 6.

Summary

In his 1916 General Theory of Relativity, Einstein predicted the existence of gravitational waves. These can be considered as ripples or waves in the curvature of space-time. Until now there has only been indirect evidence for their existence, and scientists around the world are working on a number of gravitational wave detectors. The direct detection of these waves will provide information about astrophysical processes and the sources that produce them.

Gravitational waves are quadropole in nature, producing a tidal strain in space. Their interaction with matter, though, is very weak, making them very hard to detect. Gravitational waves emitted by violent astrophysical events are predicted to produce strains at the Earth of the order of 10^{-21} to 10^{-22} at frequencies accessible to ground-based detectors ($\sim$ 10 Hz to a few kHz). One way to detect these strains is based on the Michelson interferometer.

The Institute for Gravitational Research at the University of Glasgow, led by Prof. J. Hough, is working with collaborators from the Max-Planck-Institut fur Quantenoptik at Hannover and Garching, the University of Hannover, the University of Cardiff and the Albert-Einstein-Institut at Golm on a project called GEO 600 to build a laser interferometer with arms of length 600 m. The GEO 600 detector is close to completion in Germany.

GEO 600 is designed to operate down to 50 Hz. The sensitivity limit at this frequency is set by the thermal noise from the internal modes of the test masses

that form the interferometer mirrors. The level of this noise is determined by the level of mechanical loss factors within the system. For GEO 600 these are constructed from fused silica. The strain sensitivity limit from thermal noise is expected to be $2 \times 10^{-22}/\sqrt{\text{Hz}}$ at 50 Hz. To improve sensitivity, the GEO 600 technology will need to be transplanted to a system of longer arm length, such as the American 4 km detector LIGO. Beyond this, any further increase in the sensitivity further will require a different material with a lower loss than fused silica to be found.

The work contained in this thesis covers the testing of the mechanical loss factors of a range of test substrates to determine their potential use in interferometric gravitational wave detectors.

In GEO 600 and all other detectors currently under construction, fused silica is being used for the test mirrors due to its high intrinsic quality factors (i.e. low loss factors). Samples of fused silica were tested and the good loss values confirmed. Different types of silica, though, resulted in a range of quality factors, highlighting the need for good manufacturing if the low loss levels were to be maintained. The intrinsic loss of fused silica currently limits the sensitivity of GEO 600, and if this limit is to be improved upon a different substrate with a higher intrinsic Q will be needed. A range of suitable contenders to replace fused silica was tested, the best results being achieved with sapphire samples. It had long been known that sapphire had an intrinsic Q almost 10 times that of the best fused silica samples, but this had not been achieved for samples tested outside of Russia. Work carried out on HEMEX samples yielded one example with a Q of 2.59×10^8, the highest intrinsic Q measured outside of Russia. This confirmed it as the front-runner to replace fused silica. (Though potential problems resulting from its relatively high thermal expansion coefficient make it less attractive.)

In order that the fused silica test masses may function as mirrors in the interferometric detectors, they are coated with dielectric mirror coatings. To discover whether the application of these coatings increased the losses of the test masses to a point where the sensitivity of the detectors would be degraded, a range of resonant modes for two coated fused silica masses were investigated. Analysis of the varying Q results from these tests, along with FEA modelling of the modes led to the conclusion that the coating would not present a problem for the current generation of detectors, but may prove significant for future detectors, such as Advanced LIGO. Tests carried out on a coated sample of sapphire were suggestive of a similar situation existing.

In order that the jointing of test mass to suspension system in GEO 600 will not contribute to the loss levels of the mass, they are suspended from fused silica fibres welded to ears that have been hydroxide catalysis bonded to the sides of the mass. It was already known that this bonding process did not affect the loss level significantly for fused silica to fused silica bonding. However it was not known whether this was true when fused silica was bonded to sapphire. A fused silica post was therefore bonded to a sapphire sample. Results suggested a drop in Q of roughly a factor of 10. The post had been bonded to the mass by a variation of hydroxide catalysis bonding where a sodium silicate solution was used in place of the traditional potassium hydroxide solution. This was done because this type of bonding appeared to result in a stronger bond. Results here suggested that the bonding with sodium silicate solution resulted in excess losses due to the bond of a similar order to those for the KOH case, when scaled to the case for GEO 600.

Chapter 1

The Nature, Sources and Detection of Gravitational Waves

1.1 Introduction

In his 1916 Theory of General Relativity [1] Einstein predicted the existence of gravitational waves. The solutions of the linearised Einstein Field Equations show that the effect of gravity propagates as a wave with the speed of light. World-wide interest in detecting these gravitational waves came about in the 1960's as a result of the experimental work carried out by Weber [2].

Indirect evidence of the existence of gravitational waves was provided after Hulse and Taylor [3] discovered the binary pulsar PSR 1913+16 and subsequently studied its orbits. They noted that the orbital period of the pulsar was decreasing with time. By using a model based on Einstein's Theory of General Relativity they showed that this decrease would be accounted for if the energy loss was attributed to the emission of gravitational waves.

Many collaborating groups around the world are now working to make direct detection of gravitational waves. This detection is important for several reasons. Firstly, it will allow some of the predictions of General Relativity to be tested. Secondly, it will provide new information on astrophysical events in the universe, such as the collapse of stars and the birth and interactions of black holes. To do so would be to generate a whole new field of astronomy.

1.2 Nature of Gravitational Waves

In order to answer the question "What is a gravitational wave?", it is useful to make a comparison with electromagnetic waves. Electromagnetic waves are generated by the acceleration of charge, whilst gravitational waves are generated by the acceleration of mass.

Equivalent to the conservation of charge in electromagnetism is the conservation of energy (and therefore mass) in gravity. This implies that there can be no monopole gravitational radiation. Also, conservation of momentum means that there can be no dipole gravitational radiation either. So, the lowest order of gravitational radiation must be quadrupole in nature, implying that only non-axisymmetric accelerations of mass will produce gravitational waves.

Gravitational waves produce ripples or waves in the curvature of space-time. They can therefore be considered as tidal strains in space. The waves arriving at the Earth from a distant source can be split into two independent polarisations of amplitudes h_+ and $h_\times$. The effect the passage of such a wave has on a ring of test samples is shown in figure 1.1. If the wave is incident perpendicular to the plane of the page, the ring of initial diameter L is distorted in one direction by an amount ΔL and compressed in the other direction by the same amount.

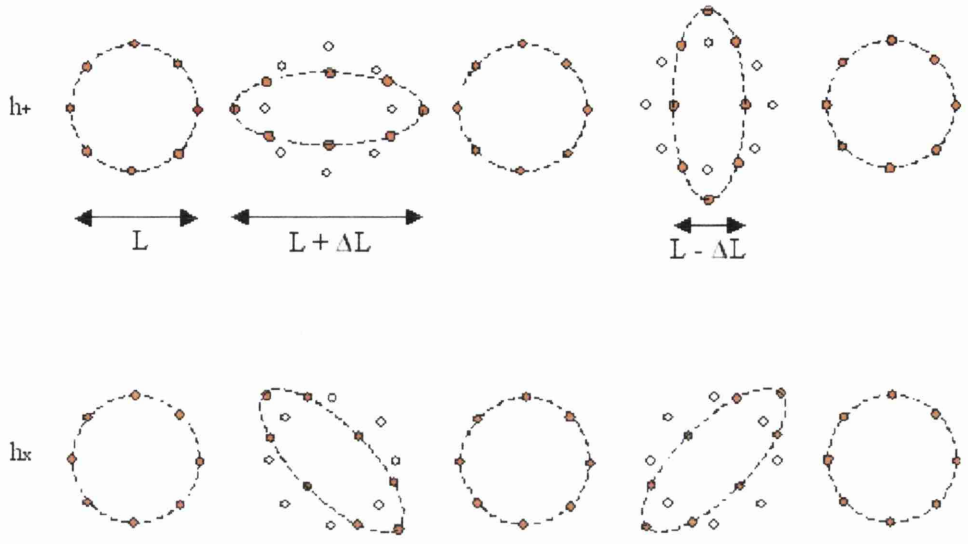

Figure 1.1: *The effect of a gravitational wave on a ring of test particles, incident perpendicular to the page.*

The amplitude of a suitably polarised gravitational wave, h, is defined in terms of the strain it produces, as detailed in equation 1.1.

$$h = \frac{2\Delta L}{L} \tag{1.1}$$

Of the four forces of nature, gravity is the weakest. Therefore, the effect of a gravitational wave is only significant when very large masses and accelerations are considered. Thus we need to work on the astrophysical scale.

1.3 Sources of Gravitational Waves

1.3.1 Introduction

Ground based gravitational wave detectors are expected to detect waves in the frequency range of a few Hz to a few kHz. This range is limited by various noise sources, as discussed later. In the following sections sources of waves in

the above frequency range are discussed.

1.3.2 Burst Sources

Supernovae

When a star becomes a supernova its brightness rapidly increases to roughly one billion times the luminosity of our own sun. Supernovae are classified into two categories, Type I and II [4]. A Type I supernova is thought to occur when a white dwarf in a binary system has gained enough mass from its companion to exceed the Chandrasekhar limit. ($M_{ch} = 1.4M_{sol} = 3$ x 10^{30}kg.) This causes the white dwarf to collapse, triggering a stellar explosion. It is believed that Type II supernovae occur when the iron core of a massive star collapses, triggering a stellar explosion. If this collapse is perfectly symmetrical, then no gravitational waves will be produced. If, due to the star's core having significant angular momentum, the collapse is asymmetric then strong gravitational waves may be produced.

Schutz [5] approximates the strain amplitude, h, expected from a supernovae to be

$$h \approx 5 \times 10^{-22} \left(\frac{E}{10^{-3} M_{\odot} c^2}\right) \left(\frac{15\text{Mpc}}{r}\right) \left(\frac{1\text{kHz}}{f}\right) \left(\frac{1\text{ms}}{\tau}\right)^{\frac{1}{2}} \qquad (1.2)$$

where E is the total energy radiated, $M_{\odot}$ is the mass of the sun, c is the speed of light, f is the frequency of the gravitational signal, τ is the time taken for the collapse to occur and r is the distance to source.

The event rate for both Type I and II supernovae, out to the Virgo cluster at a distance of $\sim$ 15 Mpc, has been estimated as several per month [4].

Coalescing Binaries

Consider a compact binary system of two high-density stars (neutron stars or black holes) rotating about their common centre of mass. As mentioned above for the case of PSR 1913+16, the orbital period of a compact binary system decays as the system inspirals, due to a loss of energy in the form of gravitational waves. As the two stars approach each other, the amplitude and frequency of the emitted waves increase. A few seconds before the two stars coalesce, the amplitude and frequency reach values that are expected to be observable by ground based gravitational wave detectors.

Schutz [6] approximates the strain amplitude, h, expected from coalescing neutron stars as

$$h \approx 1 \times 10^{-23} \left(\frac{100\text{Mpc}}{r}\right) \left(\frac{M_b}{1.2\text{M}_\odot}\right)^{\frac{5}{3}} \left(\frac{\text{f}}{200\text{Hz}}\right)^{\frac{2}{3}} \tag{1.3}$$

where $M_b = (M_1 M_2)^{3/5}/(M_1 + M_2)^{1/5}$ is the mass parameter of the binary, M_1 and M_2 are the masses of the two stars and the other symbols are defined as for equation 1.2. The timescale over which the frequency changes [6] is

$$\tau \approx \left(\frac{1.2M_\odot}{M_b}\right)^{\frac{5}{3}} \left(\frac{200\text{Hz}}{f}\right)^{\frac{8}{3}} \tag{1.4}$$

Schutz has shown that the product of h and τ is independent of mass. If h, f and τ are detected by several detectors then both the distance and the position of the source can be obtained. The accuracy will depend on the number of detectors and their respective sensitivities and signal to noise ratios.

Of the hundreds of pulsars now known, a few are located in binary systems. The number of pulsars existing in binary systems along with the estimated pulsar birth rate can be used to estimate the event rate of coalescing binary

systems. It is predicted that Advanced LIGO will have a detection rate of at the very least 2 per year, with an upper rate anywhere betweeen 300 and 1000 events per year. [7].

1.3.3 Periodic Sources

Rotating neutron stars and white dwarfs are possible sources of continuous periodic gravitational waves, provided that their rotation is non-axisymmetric. A single detector can detect such a source. For the case of an interferometer the sensitivity can be increased, once the source's frequency is known, by using signal recycling (see section 1.6) to reduce the bandwidth of the detector if the noise limit is photoelectron shot noise. Some possible sources of continuous periodic gravitational waves, detectable by ground based detectors, are outlined below.

Pulsars

The spin of a pulsar must be non-axisymmetric for it to emit gravitational waves. A typical pulsar emits waves at twice its rotational frequency, f_{rot}. An estimate of the likely amplitude from such a source is [8]

$$h \approx 6 \times 10^{-25} \left(\frac{f_{\text{rot}}}{500\text{Hz}}\right)^2 \left(\frac{1\text{kpc}}{r}\right) \left(\frac{\varepsilon}{10^{-6}}\right) \tag{1.5}$$

where ε, the equatorial ellipticity, is a measure of how asymmetric the star is.

The Crab pulsar is expected to be emitting gravitational waves at roughly 60 Hz. An upper limit of the signal from the Crab pulsar of $h \sim 10^{-24}$ is calculated for $\varepsilon = 7 \times 10^{-4}$, $r \approx 1.8$ kpc and $f_{\text{rot}} = 30$ Hz [8].

Wagoner Stars

If, as a result of accretion, a neutron star with high angular momentum reaches the Chandrasekhar-Friedman-Schutz instability point, the neutron star will become non-axisymmetric and produce gravitational waves [9]. Due to the fact that the rate of accretion of angular momentum is proportional to the rate of accretion of mass, the gravitational wave luminosity is therefore proportional to its X-ray luminosity. Recent discoveries by the Rossi X-ray Timing Explorer [10] suggest that the gravitational wave signal strength of the X-ray source SCO X-1 could be $h \sim 2 \times 10^{-26}$ at 500 Hz, at the surface of the Earth.

1.3.4 Stochastic Sources

It is expected that a random background of gravitational waves will exist, as a result of the superposition of signals from many sources. This may contain information about processes connected with the creation of the universe. One possible prediction of background radiation, from the cosmic string scenario for galaxy formation, produces an amplitude given by [11]

$$h \approx 2.4 \times 10^{-25} \left(\frac{H_0}{75\text{kms}^{-1}\text{Mpc}^{-1}}\right) \left(\frac{\Omega_{\text{gw}}}{10^{-8}}\right)^{\frac{1}{2}} \left(\frac{f}{100\text{Hz}}\right)^{-\frac{3}{2}} \left(\frac{B}{2\text{Hz}}\right)^{\frac{1}{2}} \quad (1.6)$$

in a bandwidth B about a frequency f, where Ω_{gw} is the energy density per logarithmic frequency interval required to close the universe and H_o is the present value of Hubble's Constant.

The stochastic background will be indistinguishable from other sources of Gaussian noise in one detector. It will, though, be detectable in two different detectors, when those detectors are combined to look for a common "noise" signal. Therefore, by cross-correlating the data from several detectors it should be possible to separate the stochastic background from the random

noise associated with each detector.

For periodic sources such as pulsars and Wagoner stars, and for stochastic sources, the signal to noise ratio can be increased by integrating over a long observation time.

1.4 Types of Gravitational Wave Detector

In order to detect gravitational waves, it is necessary to measure extremely small strains, h, produced in space by the waves. There are two types of ground based detectors currently being developed - resonant bar detectors and laser interferometers.

As already mentioned, ground based detectors are designed to operate in the frequency range of a few Hz to a few kHz. If a laser interferometer is put into space, it should be possible to detect gravitational waves at frequencies lower than this range. Both ground-based and space-based detectors are discussed to a certain extent in the following sections.

Other methods of searching for gravitational waves include the Doppler tracking of spacecraft and pulsar timing. The relative separation of the Earth and a spacecraft will be affected by a passing gravitational wave. This can in principle be detected from the Doppler shift in the frequency of the radio signals used to follow the spacecraft. The CASSINI mission to Saturn should be able to measure a signal of amplitude $h \sim 5 \text{ x } 10^{-17}$ at $2 \text{ x } 10^{-3}$ Hz from December 2001 [12].

Pulsar timing is similar to the Doppler tracking of a spacecraft, except that it is the radio signals from the pulsar that are used [13]. This technique is sensitive down to frequencies of order $\sim 10^{-8}$ Hz.

1.4.1 Resonant Bar Detectors

This type of detector consists of a large cylinder, typically with a mass of several tonnes, and was first developed in the 1960's by Weber [2].

If a gravitational wave signal with frequency components overlapping the fundamental longitudinal mode of the cylinder (typically $\sim$ 1 kHz) is incident on such a detector it will cause the cylinder to vibrate, inducing a mechanical strain that can be measured using a transducer and amplifier. The signal generated will be proportional to the gravitational wave amplitude.

The effects of seismic and acoustic noise on a resonant bar detector are reduced by suspending the cylinder from vibration isolation stages and placing the bar under vacuum. The sensitivity is then limited by both the thermal noise of the cylinder and the noise from the sensors. A reduction in the level of thermal noise is achieved by cooling the detector to temperatures of a few Kelvin and by constructing the cylinder from a material of low mechanical loss, or high quality factor Q, at low temperatures, typically aluminium or niobium.

Cooled resonant bar detectors have been developed by groups in Stanford University, Louisiana State University (ALLEGRO), University of Rome (NAUTILUS), CERN (EXPLORER), University of Padua (AURIGA) and Perth, Western Australia (NIOBE). Recently, groups in Italy and the USA have developed techniques to improve the strain sensitivity by cooling the bars down to temperatures of $\sim$ 50 mK. In particular, the NAUTILUS detector has measured strain sensitivities of $h \approx 6 \times 10^{-22}$ at $\sim$ 1 kHz [14].

A further increase in the sensitivity of a resonant bar detector can be achieved by increasing the mass of the detector and one way of doing this is by using a "spherical" bar. Using a "spherical" bar has two advantages. Firstly, such a bar is more massive than a cylindrical bar of the same resonant frequency

and, therefore, the effect of thermal noise is reduced. Secondly, a sphere has five usable quadrupole modes compared to one in a bar. (This, essentially, produces five detectors from one.) As a gravitational wave passes through the bar, the ratio of the amplitudes of the five modes can be used to determine the direction and polarisation of the wave. There have been several proposals for such detectors. Currently, there is one in Brazil called the Mario Schenberg Detector [15], and one called MiniGRAIL, in Leiden, Holland, seeking funding [16].

1.4.2 Ground-based Laser Interferometric Gravitational Wave Detectors

A simple interferometer detector is, in principle, a Michelson interferometer whose mirrors are suspended as pendulums. The first work on laser interferometers was carried out by Forward [17] and by Weiss [18] in the 1970's.

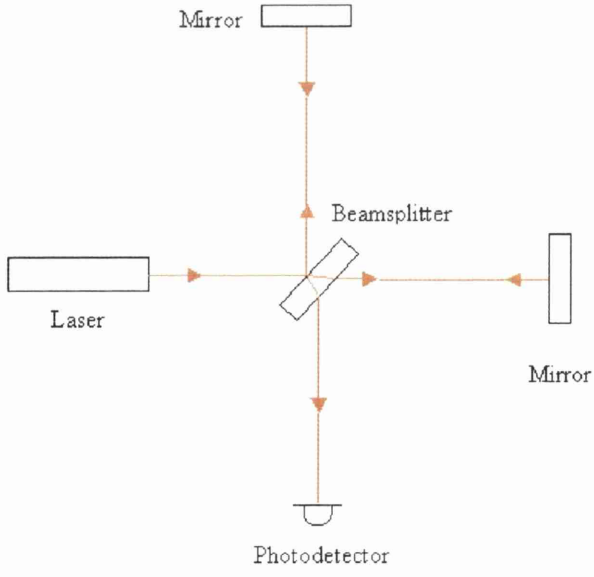

Figure 1.2: *Diagram of a simple Michelson Interferometer.*

Figure 1.2 shows a simple Michelson interferometer. Light from a laser is inci-

dent on a beamsplitter where the light beam is partially reflected and partially transmitted into the two arms, each of length L. The light is then reflected from a mirror at the end of each arm back to the beamsplitter. The combined interference pattern is then detected at the photodetector. A gravitational wave would cause a change in the intensity of this interference pattern due to the relative motion of the mirrors. To isolate the mirrors from noise sources such as ground vibrations and air pressure fluctuations, they are suspended as pendulums in a vacuum.

The effect of a gravitational wave on a ring of particles was shown in figure 1.1. The orthogonal arms of a Michelson interferometer therefore provide an ideal set-up for detecting the differential change in length caused by the quadrupole nature of gravitational waves. For example, a wave of amplitude $\delta L/L$ and of suitable polarisation propagating in a direction perpendicular to the plane of the arms of the detector will cause one of the arms to be stretched by an amount δL and at the same time cause the other arm to be compressed by δL. The result is a differential change in arm length of $2\delta L$.

As the arm length, L, increases, so too does the relative size of δL. This produces a more sensitive detector, provided the other noise sources are not also increased. The maximum sensitivity is achieved when the light is stored in the arms of the interferometer for roughly half the period of the gravitational wave [19].

For a gravitational wave of frequency 1 kHz, the corresponding arm length would be $L = \lambda_{gw}/4 \sim 75$ km [19]. An arm length of this size is not practical to construct on Earth. The longest practical length is ~ 4 km.

To solve this problem, the distance the light travels in the arms can be increased by making it travel up and down the interferometer arms several times. This

effectively increases the arm length and, therefore, the storage time of the light in the arm. The storage time is the average time the light spends in the arms of the interferometer. This effective increase in arm length can be achieved using either a delay-line or a Fabry-Perot cavity.

Delay-line Interferometer

The delay-line interferometer was first proposed by Weiss [18] in the early 1970's. The optical path length of the delay-line interferometer is increased by the use of multiple non-overlapping beams that are reflected between two curved mirrors. Each delay-line arm is illuminated via a hole in the mirror close to the beamsplitter. In an arrangement, such as that developed by the group at the Max-Planck-Institut fur Quantenoptik, Garching, Germany [20], the light exits the delay-line by the same hole.

A simplified schematic diagram of this delay-line interferometer is shown in figure 1.3. The strain sensitivity achieved in the 30 m delay line prototype interferometer at Garching was $h \sim 1 \text{ x } 10^{-19}/\sqrt{\text{Hz}}$ above 1.5 kHz achieved in 1988 [21].

Fabry-Perot Interferometer

This method of increasing the storage time inside the interferometer was first developed in Glasgow [22] in the early 1980's. Two Fabry-Perot cavities are built into the arms of the interferometer, as shown in figure 1.4. Each cavity consists of one partially and one fully reflecting mirror, with the reflected beams lying on top of each other.

The cavity is said to be on resonance, and the amount of energy in the cavity is a maximum, if the length of the cavity, L, is tuned to fit an integral number of half wavelengths of the laser light. The cavity is held on resonance using

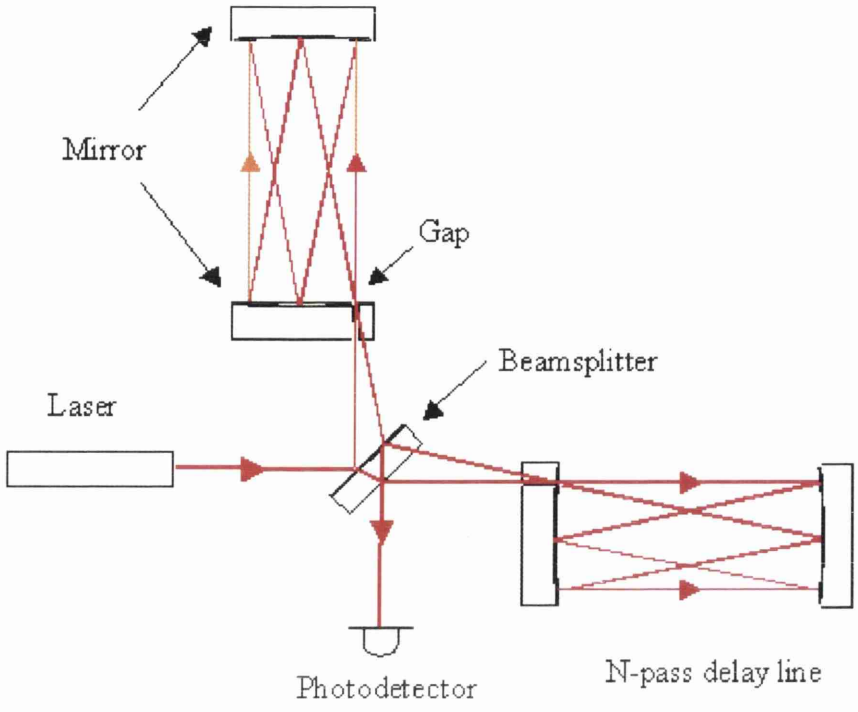

Figure 1.3: *Diagram of a delay-line interferometer.*

servo control. Under these conditions the differential displacement is increased by a factor F/π where $F = (c\pi\tau)/L$ is the finesse of the cavity and τ is the storage time.

The main advantages of a Fabry-Perot interferometer compared to a delay-line interferometer are that it is possible to use much smaller mirrors for operation, since the multiple beams overlap one another, and that the effect of scattered light within the interferometer arms is reduced [20]. The main disadvantage, though, is the need to obtain and maintain resonance [23].

The strain sensitivity achieved in the kHz region by the prototype Fabry-Perot detectors in Glasgow (10 m) and Caltech (40 m) is of the order of a few times $10^{-18} - 10^{-19}$ [13, 24, 25] for wideband bursts.

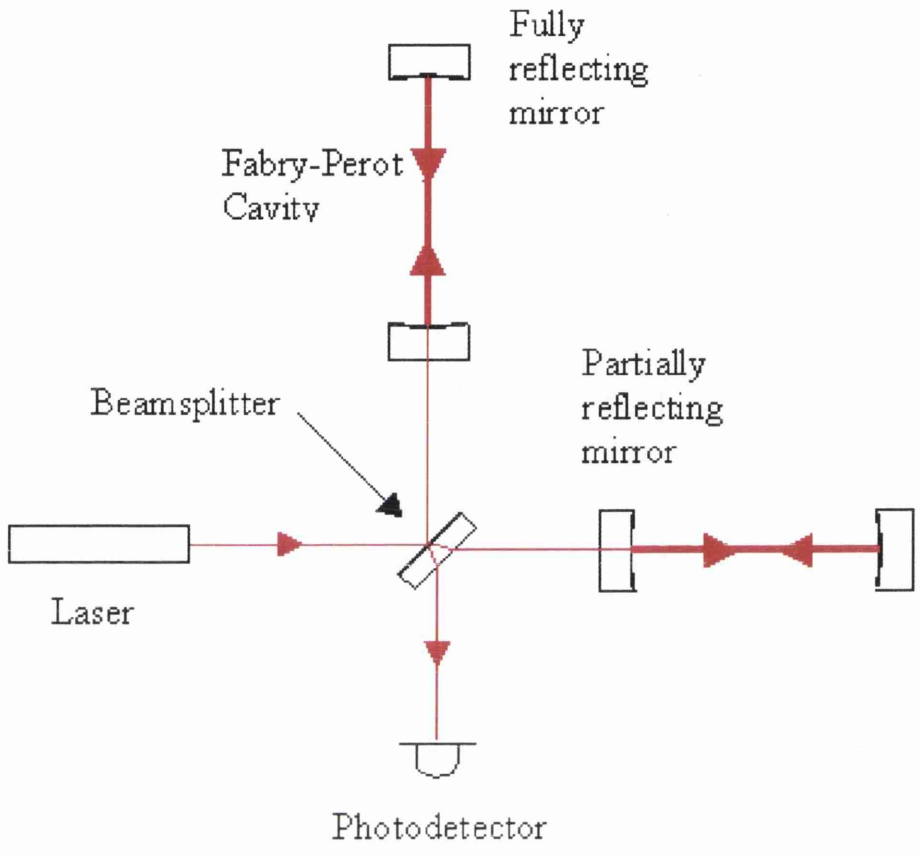

Figure 1.4: *Diagram of a Fabry-Perot interferometer.*

Ground Based Interferometers Around The World

There are several interferometric gravitational wave detectors in advanced stages of construction around the world. LIGO [26] is a project in the USA to build a 4 km detector at a site in Livingston, Louisiana and one at Hanford in Washington State, along with a 2 km one at Hanford. A French-Italian collaboration, VIRGO [27], is constructing a 3 km detector near Pisa in Italy. The Japanese are constructing a 300 m detector, TAMA 300 [28], near Tokyo and they also have plans to build a 3 km detector in a disused mine under a mountain range [29] near Tokyo. AIGO [30] is a proposed Australian project not yet funded, to build a detector at a site near Perth in Western Australia. Initially it would have an arm length of a few hundred metres, although this

could be extended up to as much as 5 km.

The Institute for Gravitational Research at the University of Glasgow is collaborating in GEO 600, a joint German-British project with 600 m arms. GEO 600 is in an advanced stage of construction at a site near Hanover in Germany. When complete, GEO should be comparable in sensitivity to the initial stages of LIGO and VIRGO. More discussion of GEO 600 follows later in this Chapter.

1.4.3 Space-based Detectors

LISA (Laser Interferometric Space Antenna) [31] is a space-based Michelson Interferometer that will observe gravitational waves in the frequency range of 0.1 mHz to 1 Hz. Space-based detectors have the advantage of not being limited by noise sources that affect ground-based detectors at low frequency. Typical sources of gravitational waves are, for example, from interactions of massive black holes and from binary systems with large separations [32]. LISA has been chosen as a cornerstone mission in the Post Horizon 2000 programme in ESA. It will consist of three identical spacecraft positioned in orbit 20^o behind the Earth, with the three spacecraft forming an equilateral triangle of side 5×10^9 m. Each spacecraft contains a test mass and a laser transponder (Nd:YAG) allowing the sides of the triangle to form two semi-independent interferometers. A gravitational wave strain sensitivity of $h \sim 10^{-21}/\sqrt{\text{Hz}}$ at 0.1 mHz is expected to be achieved. ESA/NASA are currently discussing a joint mission to launch LISA in the 2010 time frame.

Space-based detectors will be complementary to ground-based detectors and, as already stated, will extend the frequency range for observations of gravitational waves.

1.5 Noise Sources

There are a number of noise sources that limit the sensitivity achievable by laser interferometric gravitational wave detectors. These are discussed below.

1.5.1 Photon Noise

Photon noise, more properly known as photo-electron shot noise, is the statistical fluctuation in the number of photo-electrons detected in the photodiode circuit at the output of an interferometer. The signal detected at the output of the interferometer due to N detected photo-electrons will have an uncertainty of $\sqrt{N}$ associated with it due to Poisson counting statistics. This uncertainty gives rise to noise at the photodetector that will limit the sensitivity of the detector due to the fact that it is the output intensity that is used to measure the gravitational wave amplitude. For a delay-line interferometer, the shot noise sensitivity is given as [11]

$$h_{\text{shot}}(f) = \left(\frac{\pi\hbar\lambda}{2\varepsilon P_{\text{in}} c}\right)^{\frac{1}{2}} \frac{f}{\sin(\pi f\tau)} \frac{1}{\sqrt{\text{Hz}}} \tag{1.7}$$

where $\hbar$ is Planck's constant divided by 2π, λ is the light wavelength, ε is the photodetector quantum efficiency, the input power is P_{in}, c is the speed of light and τ is the light storage time. From equation 1.7 it can be seen that the shot noise can be minimised by setting the storage time equal to half of the period of the gravitational wave, i.e. $f\tau = \frac{1}{2}$. Furthermore, it can be seen that the shot noise sensitivity can be improved by increasing the level of the input power.

1.5.2 Radiation Pressure Noise

The radiation pressure noise is caused by fluctuations in the number of photons reflecting off the surface of the test mass. This can be expressed as [19]

$$h_{\mathrm{rp}}(f) = \frac{1}{mf^2L}\sqrt{\frac{\hbar P_{\mathrm{in}}}{2\pi^3 c\lambda}}\frac{1}{\sqrt{\mathrm{Hz}}} \tag{1.8}$$

where P_{in} is the input power, m is the mirror's mass, L is the arm length, c is the speed of light and λ is the laser wavelength. The level of radiation pressure noise falls off at higher frequency and at a given frequency the noise increases with P_{in}.

The photo-electron shot noise and radiation pressure noise contribute to what is known as "optical noise", the total optical noise being the quadrature sum of the two sources. From equations 1.7 and 1.8 it can be seen that radiation pressure noise dominates the optical noise spectrum at low frequency, whilst photo-electron shot noise dominates at high frequency. For a given gravitational wave frequency, f, there exists a minimum noise spectral density (due to the combined effects of photo-electron shot noise and radiation pressure noise) that occurs when the input laser power is set to an optimum level. At this optimum power it is required that $h_{\mathrm{shot}}(f) = h_{\mathrm{rp}}(f)$ [19]. The locus of points of minimum noise is called the quantum limit. This quantum limit sets a limit on the minimum differential displacement of two masses than can be determined [33]. In the interferometric detectors currently under construction, this quantum limit is significantly below the other noise sources.

1.5.3 Thermal Noise

The random motion of the atoms of the test mass mirrors and their suspensions, which are at a finite temperature and have a number of resonant modes, generates thermal noise. The magnitude of the thermal noise depends on Boltzmann's constant, k_B, and the temperature of the atoms, T. The sources of thermal noise include the pendulum modes of the suspended test masses, the violin modes of the suspension wires and the internal modes of the test

masses. For each mode, it is possible to assign k_BT of thermal energy, integrated over all frequencies. However, it is the shape of the thermal noise spectrum as a function of frequency that is important in this application. This can be derived using the complex form of Hooke's Law [34]

$$F = -k\left[1 + i\phi(\omega)\right]x \tag{1.9}$$

where the imaginary term $\phi(\omega)$ is the phase by which the displacement x lags the applied force F. The quality factor Q of a resonance, where Q is a measure of how small the dissipation is at the resonant frequency, is related to ϕ by $Q = 1/\phi(\omega_0)$, where ω_0 is the angular resonant frequency. It is possible to show, by using the Fluctuation-Dissipation Theorem, that the power spectral density of thermal motion for a mass, m is given by [34]

$$\bar{x}^2(\omega) = \frac{4k_BT{\omega_0}^2\phi(\omega)}{\omega m\left[({\omega_0}^2 - \omega^2)^2 + {\omega_0}^4\phi(\omega)^2\right]} \tag{1.10}$$

where ${\omega_0}^2 = k/m$. The maximum thermal motion occurs at the resonant frequency. By designing low loss, high Q suspensions and using high Q materials for the suspension fibres and mirrors, it is possible to ensure that the off-resonance thermal noise is kept to a minimum.

Aspects of thermal noise and its minimisation are discussed in greater depth in Chapter 2.

1.5.4 Seismic Noise

Seismic noise results from natural phenomena such as ocean waves as well as from artificial effects like traffic and machinery. The level of seismic noise varies throughout the world and also throughout the day.

Each mirror must be isolated from the seismic motion of the ground over the range of frequencies in which the detector operates. Pendulums give attenuation of ground motion above the resonant frequency of the pendulum. A single, low loss pendulum attenuates ground motion by a factor of $\sim (f_0/f)^2$, where f_0 is its resonant frequency. Suspending two or more pendulums in series increases the horizontal attenuation with each additional pendulum. Unfortunately, the isolation provided by pendulums in the vertical direction is not as good as in the horizontal. This is true because the vertical resonant frequency is much higher than the horizontal resonant frequency due to the stiffness of the wires, therefore the level of vertical isolation at a given frequency is much smaller than the horizontal isolation at the same frequency.

Vertical displacement can couple into horizontal motion at some level and so additional vertical isolation must be included in the design to minimize this horizontal motion. This can be provided by incorporating cantilever springs into the final suspension stage, as is the case for the GEO 600 triple pendulum [35].

Additional isolation is provided by suspending the triple pendulum from a series of vibration isolation stacks, consisting of alternate layers of rubber and steel. These stacks provide isolation in the vertical, horizontal and tilt directions by attenuating the seismic motion above the corresponding resonant frequencies of the stacks. Additionally, since the rubber is of intrinsically high loss, the stack does not significantly amplify the seismic motion at its resonant frequencies.

It is also possible for the test mass to couple directly to the seismic noise through local fluctuations in the gravitational field, due to matter moving in the vicinity of the detector [36, 37]. Vibration isolation has no effect on this noise source as gravity gradient noise effectively "short circuits" the stacks and

pendulums. The noise spectrum resulting from gravity gradient noise is too low to limit the sensitivity of the initial long base-line detectors, only affecting the $f \leq 20$ Hz region [38]. However, as seismic isolation designs improve and other noise sources are reduced, gravity gradient noise may ultimately determine the achievable sensitivity of a detector at low frequency.

1.5.5 Other Noise Sources

The sources of noise discussed in the above sections are the main ones. There are, though, a number of other sources that must be considered and controlled in order to reduce their effects to negligible levels.

Several of these sources are associated with the laser. These include frequency fluctuations of the laser light that introduce noise into the detector. These fluctuations can be reduced by stabilising the laser frequency to one of the arms of the detector. The effect of intensity fluctuations of the laser are reduced by modulation techniques that ensure that the change in intensity to be detected is at a frequency that is shot noise limited. This is also achieved by operating the detector at a dark fringe. Variation of laser beam position, orientation and geometry are also important. These variations can be minimised by using a mode cleaning device such as a single mode optical fibre or a mode cleaning cavity.

Fluctuations in the residual gas pressure of the vacuum system can lead to changes in the optical path length of the detector. This effect can be reduced by operating the detector at vacuum pressures of $\sim 10^{-8}$ mbar or less. Control systems are used to damp the various modes of the suspension systems. Care must also be taken so that electronic noise in these systems does not in itself cause significant motion of the masses.

1.6 GEO 600 - The Joint British/German Gravitational Wave Detector

GEO 600 is being developed by groups from the Max-Planck-Institut fur Quantenoptik at Hannover and Garching, the University of Glasgow, the University of Cardiff and the Albert Einstein Institut at Golm, together with contributions from the Laser-Zentrum, Hannover. As mentioned earlier, this project is now in an advanced state of development.

GEO 600 is an interferometer with a four-bounce delay-line in each of its 600 m arms. (The layout is detailed in figure 1.5[1].) The input laser power, of between 5 and 10 W, is provided by a stabilised diode-pumped Nd:YAG laser. Before light is sent into the interferometer it is passed through two modecleaners [39] to reduce the beam orientation and geometry noise. The mirrors within the modecleaner cavities are suspended to isolate them from the effects of ground vibrations.

To reduce random phase shifts of the light in the optical path due to fluctuations in gas density, the path lengths are entirely enclosed within vacuum systems. The target vacuum is $\sim 5 \times 10^{-8}$ mbars for H_2 and 5×10^{-9} mbars for other gases.

The suspension system for each test mass consists of a vibration isolation stack plus a triple pendulum, consisting of two layers of cantilever springs for extra vertical isolation. This vertical isolation reduces the resultant horizontal motion generated by cross-coupling with the vertical motion, by reducing the vertical motion. The cross-coupling is mainly due to the mirrors used for the second and fourth bounces being positioned one above the other (and results in the laser beam making a small angle with the horizontal) allowing the sensing

[1]Diagram drawn by M. Casey [25].

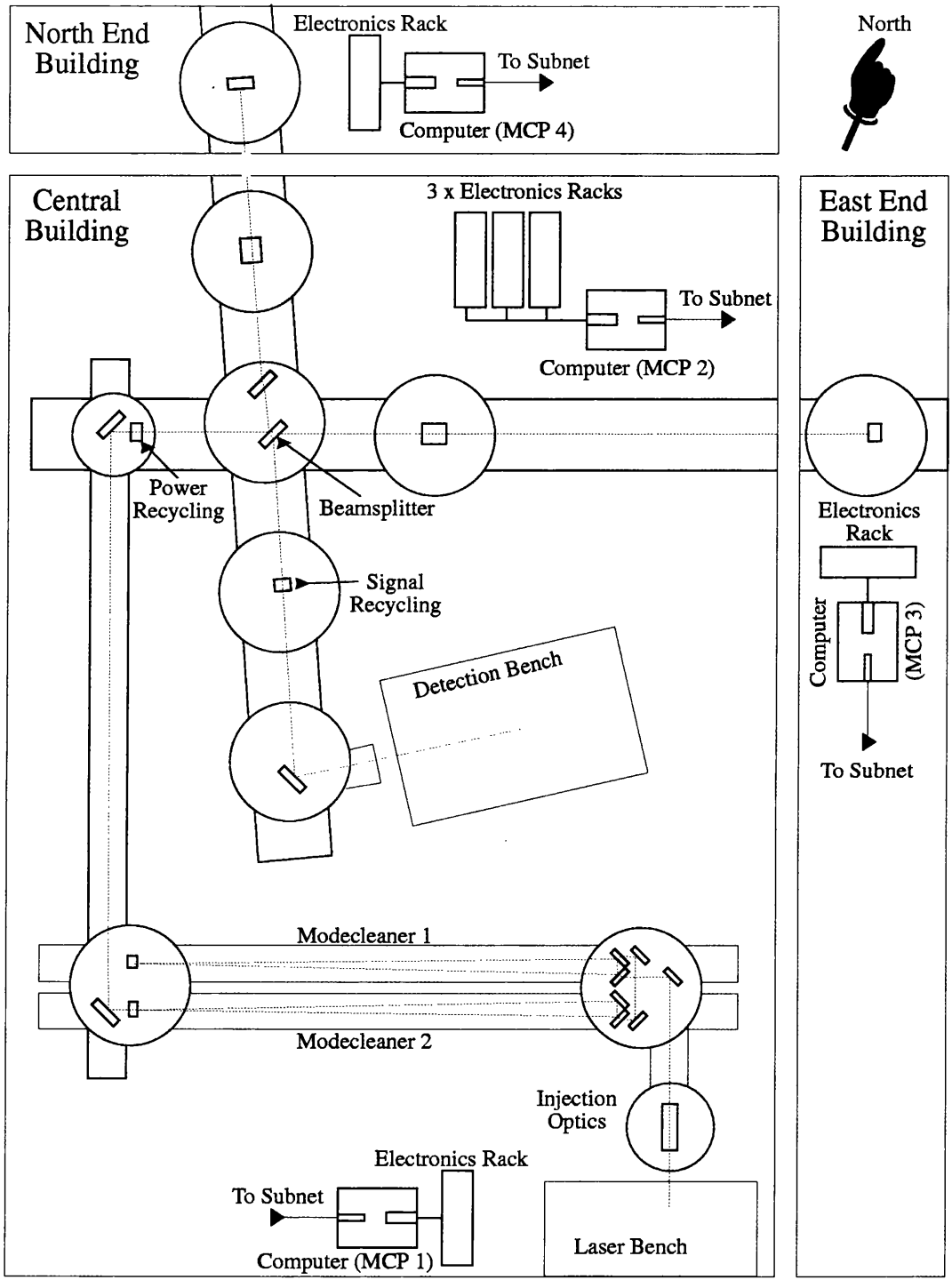

Figure 1.5: *Layout of GEO 600.*

of a small amount of vertical motion. Cross-coupling can also occur due to the curvature of the Earth - since the suspensions point towards the centre of the Earth, they are not perfectly parallel to each other. Additionally, slight mechanical differences, such as minor variation in suspension wire lengths, can contribute to the cross-coupling. The entire suspension system is also enclosed within a vacuum system.

To ensure that the sensitivity of GEO 600 is competitive with that of the first stage of LIGO and VIRGO detectors, the limitations set by the shorter arm-lengths of GEO must be compensated for by other means. The advanced optical techniques employed include high factor power recycling and signal recycling.

First consider power recycling. When the interferometer is locked to a dark fringe, all the of the recombined light at the beamsplitter is returned to the laser. To prevent this light from being lost, a mirror (known as the recycling mirror) is positioned between the laser and the beamsplitter. This forms a resonant cavity between the mirror and the interferometer [40]. The optical power circulating in the interferometer is therefore increased and the effect is equivalent to using a more powerful laser. (This technique only works for mirrors manufactured from low optical loss materials coated with low loss mirror coatings.) This recycling increases the phase sensitivity of the system. A power recycling factor of $\sim$ 2000 will be used in GEO 600, as opposed to a factor of $\sim$ 30 for LIGO.

The passage of a gravitational wave through a suitably orientated detector phase modulates the carrier frequency of the laser light. This has the effect of encoding the gravitational signal in sidebands around the laser frequency. When the detector is locked to a dark fringe the carrier frequency is returned towards the laser, whilst the sidebands are emitted at the output of the inter-

ferometer. By suitable positioning of a partially transmitting mirror between the beamsplitter and the photodiode, a cavity - known as the signal recycling cavity - can be formed for one of the sideband frequencies between this mirror and the two arms. This allows the sideband frequency to build up in the interferometer and the technique is known as signal recycling [41]. This technique has the effect of resonant enhancement of the signal of a particular frequency thus improving the shot noise limited sensitivity in narrow bandwidth operation.

One of the most important limitations to the sensitivity of a laser interferometric gravitational wave detector is thermal noise in the mirrors in the interferometer arms and their suspensions. To minimise the effect of this thermal noise in the frequency band of interest, synthetic fused silica, which has a very low level of intrinsic energy loss, is used as the mirror material. In addition, the fibres that are employed to suspend the mirrors are also made of fused silica because of this low loss. These are attached to the mirrors by a process of silicate bonding that has been shown to not degrade the levels of internal thermal noise attainable. All the other main interferometers suspend their mirrors on steel wires, at least for their first operation. Determining other materials that either have similar loss levels, or even lower ones, is part of the subject of this thesis, specifically discussed in Chapter 4.

A completed GEO 600 pendulum suspension is shown in figure 1.6.

The sensitivity curve for GEO 600 is shown in figure 1.7. The photo-electron shot noise (blue line) is calculated for a four-beam delay-line (illuminated by 5 W of laser light of wavelength 1064 nm and assumes a power recycling factor of 2000). The thermal noise (green)is plotted for a fused silica test mass of diameter 18 cm and length 10 cm, assuming an intrinsic loss factor of 2×10^{-7} and structural damping. The seismic noise curve (red) is plotted in accordance

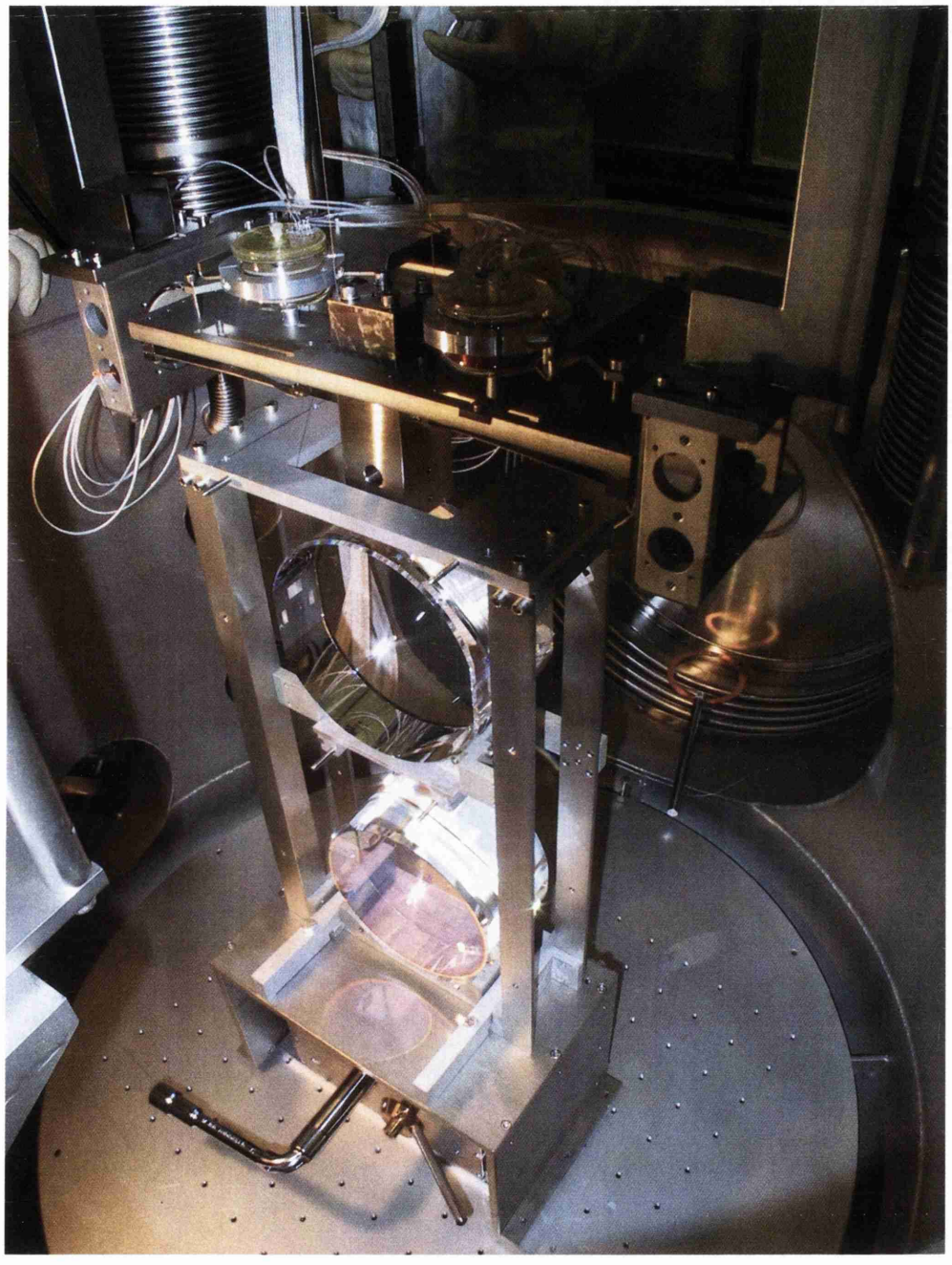

Figure 1.6: *A completed GEO 600 pendulum suspension.*

with a design specification at 50 Hz to achieve a level of seismic noise at each test mass that is a factor of 10 lower than the thermal noise associated with the internal modes at 50 Hz. The total noise curve is the black line.

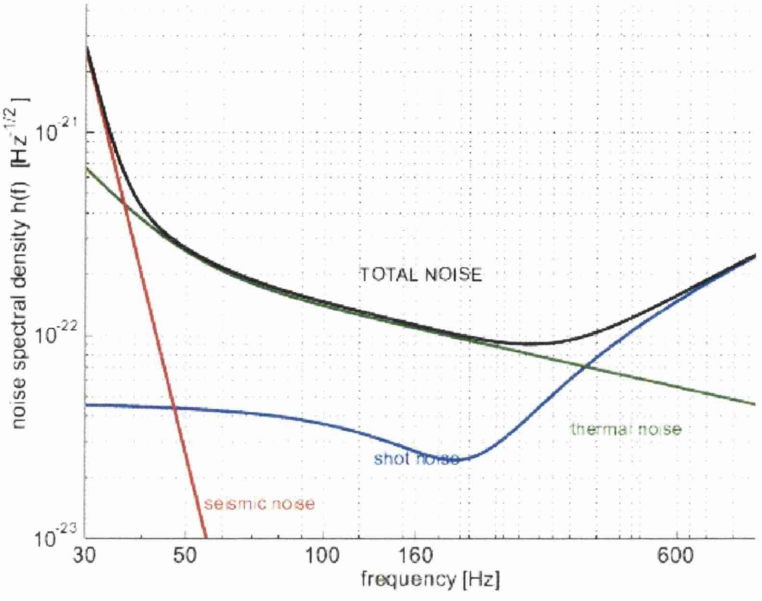

Figure 1.7: *Sensitivity curve for GEO 600.*

1.7 Conclusions

Gravitational waves were predicted by Einstein and evidence for their existence subsequently obtained by the work of Hulse and Taylor. Long base-line interferometers GEO 600, VIRGO, TAMA 300 and the 1st stage LIGO should achieve sensitivities in the range $\sim 10^{-21}$ to $\sim 10^{-22}/\sqrt{\text{Hz}}$ over a detection band between a few Hz to a few kHz.

GEO 600 should be operational within the next year and will then be able to search for continuous sources such as pulsars. GEO 600 will also work in network with the other long base-line detectors, allowing for coincidence observations of burst sources to be made. The position of such a source is determined by comparing the arrival time of gravitational wave signals at the detectors in the network. Additionally, in the fullness of time space-based detectors will complement the observations of ground-based detectors by increasing the bandwidth over which searches for gravitational waves can be made.

Chapter 2

Thermal Noise Principles

2.1 Introduction

A mirror suspended as a pendulum from wires or fibres is a mechanical system with many modes of oscillation. Each of these modes has, in accordance with the Equipartition theorem, a mean energy of $k_{\mathrm{B}}T$ joules associated with it, where k_{B} is Boltzmann's constant and T is the temperature in Kelvin. This energy appears as thermally driven motion of the mechanical system. All physical quantities that are observed are accompanied by thermal fluctuations resulting from the thermal motion of the microscopical degrees of freedom within the material, known as thermal noise.

The combined effect of this thermal noise from all the suspension system's modes means that thermally induced motion of the test mass and its suspension fibres is a serious form of displacement noise in interferometric gravitational wave detectors. It is necessary to design a suspension so that the thermal noise of the front face of the test mass is less than the expected displacement of this face by a gravitational wave.

It could be suggested that one way in which to reduce this thermally induced

motion would be to cool the mechanical system as is done in the case of resonant detectors. However, whilst this may be possible for future interferometric gravitational wave detectors, for the present it is not feasible. It is therefore necessary to employ other methods to reduce the thermal noise at the frequencies of interest for the detection of gravitational waves.

2.2 The Beginnings of Thermal Noise

In 1827 the botantist Robert Brown [42] observed vigorous, irregular motion of pollen grains in water. He also witnessed the phenomenon in dust particles. Brown assumed that this motion was associated with the particles themselves, but in 1905 Einstein [43] realised that the motion came about as a result of the fluctuation in the number of impacts between the water particles and the pollen - i.e. the motion was due to the fluid surrounding the particles, not the particles themselves.

Einstein realised that these impacts resulted in the pollen grains losing kinetic energy as they moved through the water. This was the first time that a relationship was observed between the fluctuation (which excites a system) and friction (which dissipates the system's energy).

Einstein's relation was an early example of a theorem developed later by Callen et al [44, 45] called the Fluctuation-Dissipation Theorem. This provided a general relationship between the fluctuation and dissipation for any system that is linear and in thermal equilibrium. This theorem is a useful tool in the study of thermal noise.

2.3 The Fluctuation-Dissipation Theorem

The fluctuation-dissipation theorem relates the power spectral density of the fluctuating thermal driving force, $S_F(\omega)$, of a mechanical system to the real (i.e. dissipative) part of the mechanical impedance, Z. i.e.

$$S_F(\omega) = 4k_BTRe[Z(\omega)] \tag{2.1}$$

The mechanical impedance is defined as

$$Z = \frac{F}{v} = \frac{F}{i\omega x} \tag{2.2}$$

where v is the velocity response of the system resulting from an applied force F and x is the displacement response. Using this relation, the fluctuation-dissipation theorem can be rewritten in terms of the power spectral density of thermal displacement, $S_x(\omega)$.

$$S_x(\omega) = \frac{4k_BT}{\omega^2}Re[Y(\omega)] \tag{2.3}$$

Here $Y(\omega) = 1/Z(\omega)$ is the mechanical admittance.

The fluctuation-dissipation theorem is of importance because it lets us predict the effect of manipulating the dissipation or damping (the real part of the impedance) on the thermal noise.

2.4 Damping Sources: External and Internal

2.4.1 External Damping

There are numerous sources of external damping.

- External viscous damping in the form of friction from residual gas molecules
- The loss of energy from the pendulum suspension into a recoiling support structure, known as recoil damping.
- Energy loss due to eddy current and hysteresis damping
- Frictional losses at the point of suspension and where the wires meet the test mass.

2.4.2 Internal Damping

If all sources of external damping are assumed to have been minimised to the point where they are no longer the dominant noise sources, then the largest thermal motion source within the test mass suspension system is internal friction in the material of the test mass and its suspension wires.

When an external force acts upon a body the body reacts, though not instantaneously. Rather, each of the body's affected degrees of freedom return to a new equilibrium state after an interval known as the "relaxation time". This response lag can be caused by moving defects, shifting grain boundaries, thermal currents, as well as other internal variables. It is the combined effect of these lags that is known as internal damping. By using the fluctuation-dissipation theorem the level of this internal damping can be used to predict the thermal noise level that will be present in a pendulum hanging in a gravitational wave detector at a given temperature.

A resonant mode of a pendulum system, such as an internal mode of the test mass, can be modelled as a damped harmonic oscillator represented by a mass, m, on a spring of constant, k. For an elastic spring, the restoring force is defined as

$$F = -kx \tag{2.4}$$

To include the effects of dissipation resulting from internal friction, it is necessary to rewrite equation 2.4 in a complex form. The force associated with the spring therefore takes on the form of

$$F_{\text{spring}}(\omega) = -k(1 + i\phi(\omega))x \tag{2.5}$$

$\phi(\omega)$ is known as the loss angle, or loss factor, and represents the phase lag (in radians) of the response of the system, x, to the applied force, $F_{\text{spring}}(\omega)$. This generalisation defines anelasticity.

The equation of motion for a harmonic oscillator subject to internal friction is

$$F(\omega) = m\ddot{x} + k(1 + i\phi(\omega))x \tag{2.6}$$

where $F(\omega)$ is the internal thermal driving force. An expression for the motion induced in the oscillator due to the internal friction can be derived from this equation of motion. To do so, the equation of motion must first be rewritten in terms of velocity. i.e. equation 2.6 becomes

$$F(\omega) = i\omega mv - i\frac{k}{\omega}(1 + i\phi(\omega))v \tag{2.7}$$

using $\ddot{x} = i\omega v$ and $x = v/i\omega$.

Since the fluctuating force is related to the impedance, $Z(\omega)$, by $Z = F/v$, equation 2.7 can be rearranged as

$$\frac{F}{v} = i\omega m - i\frac{k}{\omega}(1 + i\phi(\omega)) = Z$$

Therefore,

$$Z = i\left(\omega m - \frac{k}{m}\right) + \phi(\omega)\frac{k}{\omega} \tag{2.8}$$

From this the admittance, $Y = 1/Z$, can be obtained.

$$Y = \frac{\omega}{k\phi(\omega) + i(m\omega^2 - k)} \tag{2.9}$$

$$= \frac{\frac{k}{\omega}\phi(\omega) - i\left(\omega m - \frac{k}{\omega}\right)}{\left(\frac{k}{\omega}\phi(\omega)\right)^2 + \left(\omega m - \frac{k}{\omega}\right)^2} \tag{2.10}$$

Then, by substituting the real part of the admittance into the fluctuation-dissipation theorem, as shown in equation 2.3, the power spectrum of thermal motion is given by

$$S_x(\omega) = \frac{4k_BT}{\omega^2} Re[Y(\omega)] \text{ per Hz} \tag{2.11}$$

$$= \frac{4k_BT}{\omega^2} \frac{\frac{k}{\omega}\phi(\omega)}{\left(\frac{k\phi(\omega)}{\omega}\right)^2 + \left(\omega m - \frac{k}{\omega}\right)^2} \tag{2.12}$$

This expression can be simplified by substituting $k = {\omega_0}^2 m$ into it. Hence,

$$S_x(\omega) = \frac{4k_BT}{\omega^2} \frac{\phi(\omega){m\omega_0}^2/\omega}{(m^2{\omega_0}^4/\omega^2)\phi^2(\omega) + (\omega m - m{\omega_0}^2/\omega)^2}$$

$$= \frac{4k_BT}{\omega} \frac{\phi(\omega){\omega_0}^2}{m[{\omega_0}^4\phi^2(\omega) + ({\omega_0}^2 - \omega^2)^2]} \tag{2.13}$$

2.4.3 The Form of Internal Damping

There are several forms that the internal loss factor can take. One such form has the loss factor $\phi(\omega)$ proportional to frequency, ω, in the form $\phi(\omega) = \beta\omega$,

where β is a constant. In this case, the imaginary term in equation 2.5, which is the internal damping term, reduces as follows:

$$Im[F] = -ik\beta\omega x = F_{\text{friction}}$$

Hence

$$F_{\text{friction}} = -bv \tag{2.14}$$

where $v = i\omega x$ and $b = k\beta$. A loss factor of this form is described as a source of "internal viscous damping".

There is evidence which suggests that damping such as the above, namely that which is proportional to velocity, is not the most common form of internal damping in materials. Experiments [46] have shown that a loss factor that is approximately constant with frequency is more realistic. A loss factor independent of frequency is known as "structural damping". Understanding the origin of a constant loss factor, though, is complex. It is thought that the loss factor, $\phi(\omega)$, contains a number of distinct "peaks" that occur are the "characteristic frequencies" of the many contributing loss processes that happen simultaneously within the material. These peaks, known as "Debye peaks", are usually separated in frequency by many orders of magnitude. In regions of the frequency space away from the peaks of the individual loss mechanisms, the combined effect of the tails of the peaks is effectively constant with frequency [47]. The detection bands of ground based interferometers usually lie within one such frequency region.

One mechanism of internal friction which may exhibit a peak close to the detection band is thermoelastic damping. In this case, the loss factor departs from the general case of structural damping. The source of this damping is

discussed later in this chapter.

It is clear that the shape of the power spectrum for thermal displacement varies depending on which of the functional forms of loss factor is present within the suspension. The form of the loss factor must be determined if the predictions of the limits set to the detector sensitivity by thermal noise are to be accurately calculated. For the pendulum suspensions used in interferometric gravitational wave detectors the loss factors are very small and it is therefore very difficult to directly measure $\phi(\omega)$ at the frequencies of interest for gravitational wave detectors. The loss factor can, however, be measured at the resonant frequencies of the suspension and the test masses, the relationship between the loss factor and the quality factor, Q, of a resonance being used.

To obtain this relationship it is useful to note that the quality factor of a resonant system, Q, defined in terms of the damping coefficient, b, and mass, m, is [48]

$$Q(\omega_0) = \frac{m\omega_0}{b} \tag{2.15}$$

The damping present within the suspension system is given by the real part of the mechanical impedance. In equation 2.8, the real part is $\phi(\omega)k/\omega$, which is equivalent to the damping coefficient, b, in equation 2.15. (b is a constant in the case of velocity damping, but a function of frequency for structural damping.) Substituting for b (at $\omega = \omega_0$) into equation 2.15 leads to a relationship between $Q(\omega_0)$ and $\phi(\omega_0)$ of

$$Q(\omega_0) = \frac{1}{\phi(\omega_0)} \tag{2.16}$$

since $k = m{\omega_0}^2$.

2.5 Calculating the Thermal Noise Level

Consider the general expression for the power spectral density of the thermal motion of one of the modes of a suspension, $S_x(\omega)$, in terms of the internal dissipation as given in equation 2.3. The level of thermal motion can be altered by changing the level of internal damping, $\phi(\omega)$, present in the suspension.

At first consideration, the above statement appears to be at odds with the equipartition of energy theorem. This states that every velocity component of a system has an average energy of $\frac{1}{2}k_BT$ associated with it. For example, in a one dimensional oscillator, the equipartition theorem requires that

$$\frac{1}{2}m\bar{v^2} = \frac{1}{2}k_BT \tag{2.17}$$

This can be rearranged to give

$$\bar{x^2} = \frac{k_BT}{m{\omega_0}^2} \tag{2.18}$$

which is independent of the loss, $\phi(\omega)$. The fluctuation-dissipation theorem and equipartition theorem do not disagree, though. Rather, they give different information. The equipartition theorem refers to the mean square thermal displacement calculated over all frequencies. This equals the square of the thermal motion calculated at each frequency by the fluctuation-dissipation theorem summed over all frequencies. The existence of this "total" squared displacement allows us to refine the understanding of the information given by the fluctuation-dissipation theorem.

Consider the power spectral density of displacement in three regions of frequency as given by the fluctuation-dissipation theorem. These cases are $\omega \ll \omega_0$, $\omega = \omega_0$ and $\omega \gg \omega_0$. Firstly, $\omega \ll \omega_0$:

$$S_x(\omega) = \frac{4k_BT\phi(\omega){\omega_0}^2}{m\omega[{\omega_0}^4\phi^2(\omega) + ({\omega_0}^2 - \omega^2)^2]} \text{ per Hz}$$

$$\approx \frac{4k_BT\phi(\omega){\omega_0}^2}{m\omega[{\omega_0}^4\phi^2(\omega) + ({\omega_0}^4)]} \text{ per Hz}$$

$$\approx \frac{4k_BT\phi(\omega)}{m\omega{\omega_0}^2[\phi^2(\omega) + 1]} \text{ per Hz} \tag{2.19}$$

and assuming that $\phi^2(\omega) \ll 1$, this reduces to

$$S_x(\omega) \approx \frac{4k_BT}{m{\omega_0}^2}\frac{\phi(\omega)}{\omega} \text{ per Hz} \tag{2.20}$$

Now $\omega \gg \omega_0$:

$$S_x(\omega) \approx \frac{4k_BT\phi(\omega){\omega_0}^2}{m\omega[{\omega_0}^4\phi^2(\omega) + (\omega^2)^2]} \text{ per Hz}$$

$$\approx \frac{4k_BT\phi(\omega){\omega_0}^2}{m\omega{\omega_0}^4\phi^2(\omega) + m\omega^5} \text{ per Hz} \tag{2.21}$$

which reduces, if again $\phi^2(\omega) \ll 1$, to

$$S_x(\omega) \approx \frac{4k_BT{\omega_0}^2}{m}\frac{\phi(\omega)}{\omega^5}\text{per Hz} \tag{2.22}$$

Examining equations 2.20 and 2.22 shows that the levels of thermal noise can be minimised at frequencies away from the resonances of the suspension system by designing the suspension to have very low levels of mechanical loss (i.e. $\phi(\omega) \ll 1$). However, to conserve the "total" squared displacement over all frequencies (as given by the equipartition theorem) there must be a correspondingly high response at the resonant frequency, i.e. at $\omega = \omega_0$:

$$
\begin{aligned}
S_x(\omega) &\approx \frac{4k_BT\phi(\omega_0){\omega_0}^2}{m\omega_0[{\omega_0}^4\phi^2(\omega_0)]} \text{ per Hz} \\
&= \frac{4k_BT\phi(\omega_0){\omega_0}^2}{m\phi^2(\omega_0){\omega_0}^5} \text{ per Hz} \\
&= \frac{4k_BT}{m{\omega_0}^3}\frac{1}{\phi(\omega_0)} \text{ per Hz} \qquad (2.23)
\end{aligned}
$$

which results in a very large $S_x(\omega_0)$ if $\phi(\omega) \ll 1$.

Equation 2.20 can be used to calculate the thermal noise contribution from one internal mode at frequencies below the resonant frequency, within the detection band. This equation can be generalised to include all the relevant internal modes:

$$
S_x(\omega) = \sum_n \frac{4k_BT\phi_{\text{internal}_n}(\omega)}{\alpha_n m{\omega_n}^2\omega} \qquad (2.24)
$$

Here, ϕ_{internal_n} is the loss factor associated with the n^{th} order internal mode and $\alpha_n m$ is the effective mass of the same mode. α_n is an empirical factor that characterises the coupling between the internal mode and the optical mode [49]. It depends on the size of the laser beam, the mirror's mass and the resonance frequency, ω_0. Unless the losses in the test mass are homogeneous, this expression does not give the correct result for thermal noise, though [50].

An alternative technique to calculate the thermal noise for a system was presented by Levin [51]. This technique employs a different interpretation of the thermal noise spectrum as defined by equation 2.11. Levin considered the effect of applying an oscillating pressure to the face of the mass. This pressure takes the form:

$$P = F_0 \frac{e^{-r^2/r_0^2}}{\pi r_0^2} cos(\omega t) \tag{2.25}$$

F_0 is a constant force amplitude, $w = 2\pi f$ is the angular frequency at which one wants to know the spectral density of thermal noise and r_0 is the radius of the laser beam at a point where its intensity has fallen to 1/e of its maximum value. Levin then defines the real part of the admittance $Y(\omega)$ in terms of the energy fed into the test mass by the oscillating pressure P, and subsequently dissipated by thermoelastic heat flow. From this the rate of the energy dissipation, W_{diss}, is then calculated, averaged over the period $2\pi/\omega$ of the pressure oscillations.

$$Re[Y(\omega)] = \frac{2W_{\text{diss}}}{{F_0}^2} \tag{2.26}$$

Hence,

$$S(\omega) = \frac{8k_B T W_{\text{diss}}}{\omega^2 {F_0}^2} \tag{2.27}$$

This method varies from that used in the past to calculate the thermal noise for test masses. As detailed earlier, in the past the thermal noise was determined by decomposing the test mass into its normal modes, calculating the contribution of each mode to the thermal noise, $S_x(\omega)$ and then summing up those contributions. The "normal-mode decomposition" method has two main disadvantages over Levin's. Firstly, the fundamental assumption in the decomposition method is that the different normal modes have independent Langevin forces. This assumption only holds, though, if the friction sources are uniformly distributed throughout the body of the test mass. It breaks down if the defects are more concentrated in one place than in others, e.g. in the case of a lossy surface coating. This will be discussed in more detail in Chapter 5. The second advantage is that to get a good estimation for the thermal noise,

the mode-decomposition method requires many modes to be identified and calculated, which could prove time consuming and computationally expensive.

Following from equation 2.27, the power spectral density of the thermal noise at frequencies well below the first internal resonance mode of a test mass resulting from the intrinsic dissipation of a material at a temperature T can be expressed as [52]:

$$S(\omega) = \frac{4k_B T}{\omega} \frac{1-\sigma^2}{\sqrt{2\pi} Y r_0} \phi(\omega) \tag{2.28}$$

When the appropriate values from table 2.1, and the assumptions that $r_0 = 0.06/\sqrt{2}$ m, $\phi_{\text{fs}} = 5 \times 10^{-8}$, $\phi_{\text{sapp}} = 3 \times 10^{-9}$ (typical for Advanced LIGO), $T = 300$ K and $\omega = 2\pi \times 100$ s^{-1} are substituted into equation 2.28 it is possible to calculate the thermal motion, $\sqrt{S(\omega)}$, for the current detector test material fused silica and a possible replacement, sapphire. For fused silica, $\sqrt{S_{\text{FS}}(\omega)} = 1.29 \times 10^{-20}$, whilst for sapphire, $\sqrt{S_{\text{sapp}}(\omega)} = 1.43 \times 10^{-21}$. i.e. the thermal noise level is 9 times lower for sapphire than for fused silica. This suggests that sapphire would make a good replacement for fused silica as it would allow an increase in sensitivity. However, as is discussed in the next section, other factors suggest that sapphire may not be an ideal choice.

Property	Fused Silica	Sapphire
Y (Pa)	7.3×10^{10}	3.4×10^{11}
σ	0.17	0.29
C (Jkg^{-1}K^{-1})	670	790
ρ (kgm^{-3})	2200	3980
α (K^{-1})	5.5×10^{-7}	5×10^{-6}
κ (Jm^{-1}s^{-1}K^{-1})	1.4	40

Table 2.1: *Material properties for fused silica and sapphire.*

2.6 Thermoelastic Damping

Part of the thermal noise of a system arises from thermoelastic damping. The thermoelastic noise arises from fluctuations (thermodynamic in origin) in temperature throughout the body of a test mass. These temperature fluctuations cause areas of the mass to expand or contract as they heat up or cool, respectively. As the mass attempts to restore the thermal equilibrium, heat flow occurs, a source of energy loss. The temperature fluctuations are turned into motion in the test mass by the thermal expansion coefficient, $\alpha = \left(\frac{1}{l}\right)\left(\frac{dl}{dT}\right)$. The length scale of the fluctuations is dependant on the thermal diffusion over the timescale of interest, which is dependant on the thermal conductivity, κ, and the specific heat capacity, C. A laser spot interrogating the face of a test mass then averages over a number of these area of fluctuation. Braginsky et al [53] derived an expression (equation 2.29) to calculate the thermoelastic power spectral density.

$$S^{TE}(\omega) = \frac{8}{\sqrt{2\pi}} \frac{k_B T^2 \alpha^2 (1+\sigma)^2 \kappa}{\rho^2 C^2 r_0^3 \omega^2} \tag{2.29}$$

Here, k_B is Boltzmann's constant, T is the temperature of the test mass, σ is the Poisson's ratio, ρ is the density, r_0 the radius of the laser spot once its intensity has fallen to 1/e of the maximum value and α is the thermal expansion coefficient. This expression was derived for an infinite test mass. For the case of a finite test mass, Liu and Thorne [52] determined a correction factor. This factor, which is dependant on the dimensions of the test mass, is approximately equal to unity for typical test masses.

Using the values in table 2.1 it is possible to compute the value of $S^{TE}(\omega)$ for fused silica and sapphire, assuming $r_0 = 0.06/\sqrt{2}$ m (typical for Advanced LIGO), $T = 300$ K and $\omega = 2\pi \times 100$ s^{-1}. From this, the level of thermoelastic motion can be found, $\sqrt{S^{TE}(\omega)}$. For fused silica, $\sqrt{S^{TE}(\omega)} = 1.87 \times 10^{-22}$

$m/\sqrt{Hz}$, and for sapphire $\sqrt{S^{TE}(\omega)} = 4.71 \times 10^{-21}$ $m/\sqrt{Hz}$. i.e. the level of thermoelastic motion in sapphire is 25 times that for fused silica. This fact will play an important part in determining whether sapphire replaces fused silica in future gravitational wave detectors, as it will affect the achievable sensitivity.

2.7 Why Suspend the Test Mass as a Pendulum

The test mass is suspended as a pendulum so as to attenuate seismic noise in the detector's detection band. This is done by choosing the suspension length so that the pendulum mode resonant frequency is below the detection band's low frequency end.

The pendulum mode has thermal noise associated with it. It is possible, though, to construct the pendulum in such a way that this thermal noise does not contribute significantly to the overall thermal noise level in the frequency band of interest. This is achieved in two ways. Firstly, the pendulum mode has a low resonant frequency, ensuring that the maximum thermal displacement occurs at a frequency outwith the interferometer's detection band. At 50 Hz, the thermal displacement will have reached a level predicted by equation 2.20, with the loss factor associated with the pendulum mode, $\phi_{pend_{total}}(\omega)$, substituted for $\phi(\omega)$. Secondly, this loss factor associated with the pendulum mode is significantly below the intrinsic loss of the material of the suspension wires/fibres. This is detailed below.

Consider a simple pendulum of mass, m, suspension wire length l, hanging from a rigid support structure. All external damping mechanisms are assumed negligible. The test mass hangs in equilibrium at a position where the mass's weight it balanced by the elastic restoring force of the wire. The pendulum

is now pushed to the side. Two restoring forces act on the pendulum - one provided by the transverse elasticity of the tensioned wire, the other gravity. The suspension wire bends at the top [54] and, providing that the wire is thin, the gravitational restoring force plays the dominant part. Gravity provides a "spring constant", k_{grav}, defined as

$$k_{\text{grav}} = \frac{mg}{l} \tag{2.30}$$

and is lossless. The only energy loss from the pendulum is due to the small dissipative fraction of the transverse elastic spring constant of the suspension wires, which itself is only a very small fraction of the total effective spring constant.

The next step is to derive an expression for the loss factor of the pendulum mode in terms of the loss associated with wire bending. Consider the following definition for loss [48]:

$$\phi(\omega_0) = \frac{1}{Q(\omega_0)} = \frac{E_{\text{lost/cycle}}}{2\pi E_{\text{stored}}} \tag{2.31}$$

The energy lost per cycle is dissipated in the bending of the wire. The energy stored in bending the wire is:

$$E_{\text{stored wire}} = \frac{1}{2} k_{\text{wire}} x^2 \tag{2.32}$$

where x is the horizontal displacement of the pendulum from its equilibrium position. The energy lost per cycle is a fraction, α, of the total elastic energy. I.e.

$$E_{\text{lost/cycle}} = \frac{1}{2} \alpha k_{\text{wire}} x^2 \tag{2.33}$$

The total energy stored in a cycle of the swinging pendulum is

$$E_{\text{stored}_{\text{pend}}} = \frac{1}{2}(k_{\text{wire}} + k_{\text{grav}})x^2 \tag{2.34}$$

Hence,

$$\phi_{\text{mat}_{\text{total}}}(\omega_0) = \frac{\frac{1}{2}\alpha k_{\text{wire}} x^2}{2\pi \frac{1}{2} k_{\text{wire}} x^2} = \frac{\alpha}{2\pi} \tag{2.35}$$

and

$$\begin{aligned} \phi_{\text{pend}_{\text{total}}}(\omega_0) &= \frac{\frac{1}{2}\alpha k_{\text{wire}} x^2}{2\pi \frac{1}{2}(k_{\text{wire}} + k_{\text{grav}})x^2} \\ &= \frac{\alpha k_{\text{wire}}}{2\pi(k_{\text{wire}} + k_{\text{grav}})} \end{aligned} \tag{2.36}$$

Dividing equation 2.36 by equation 2.35 gives the following relationship:

$$\frac{\phi_{\text{pend}_{\text{total}}}(\omega_0)}{\phi_{\text{mat}_{\text{total}}}(\omega_0)} = \frac{k_{\text{wire}}}{k_{\text{wire}} + k_{\text{grav}}} \tag{2.37}$$

Since $k_{\text{grav}} \gg k_{\text{wire}}$, this simplifies to

$$\phi_{\text{pend}_{\text{total}}}(\omega_0) \simeq \phi_{\text{mat}_{\text{total}}}(\omega_0) \frac{k_{\text{wire}}}{k_{\text{grav}}} \tag{2.38}$$

Now, since $k_{\text{grav}} \gg k_{\text{wire}}$, equation 2.38 shows that the loss factor of the pendulum modes is reduced from the loss factor of the material of the suspension wire by a factor $\frac{k_{\text{wire}}}{k_{\text{grav}}}$, known as the dilution factor.

So far the mass has been considered to be hanging from one wire. One can now generalise to the case for n wires of length l suspending a mass, m. The elastic spring constant of a bending wire under tension is given by [34]

$$k_{\text{wire}} = \frac{n\sqrt{TYI}}{2l^2} \tag{2.39}$$

where T is the tension per wire, Y is the Young's modulus of the wire material and I is the moment of cross-sectional area. For a cylindrical wire of radius, r, $I = \pi r^4/4$. Substituting equations 2.39 and 2.30 into equation 2.38 gives

$$\phi_{\text{pend}_{\text{total}}}(\omega_0) \simeq \phi_{\text{mat}_{\text{total}}}(\omega_0)\frac{n\sqrt{TYI}}{2mgl} \tag{2.40}$$

This can be further generalised to

$$\phi_{\text{pend}_{\text{total}}}(\omega_0) \simeq \phi_{\text{mat}_{\text{total}}}(\omega_0)\frac{\xi n\sqrt{TYI}}{2mgl} \tag{2.41}$$

where ξ takes the value of 1 or 2 depending on whether the wire positions constrain them to bend at the top, or the top and bottom, respectively [55]. Although equation 2.41 is defined at the resonant frequency, ω_0, the same relationship holds for any frequency ω.

2.8 Resonance Modes of a Pendulum Suspension System

There are two main groupings of resonance modes in a pendulum suspension system:

- internal vibrational modes of the suspended test mass
- suspension modes

2.8.1 Internal Resonance Modes

For these modes, the test mass is considered to be an elastic body. When the mass resonates, its centre of mass remains unmoved whilst the mass's shape changes. There are a variety of different mode shapes that can be excited within the mass, some of which couple into the interferometer whilst others do not. Only those that involve motion of the centre of the test mass's face will contribute to the level of displacement noise in an interferometric gravitational wave detector, assuming the laser beam hits the centre of mass's face. Why it is desirable for this to be the case is dealt with later in this section.

The thermal noise associated with the combined effects of the internal modes of the test mass is intrinsic to the material have already been discussed.

The dimensions and mass of the test masses in modern interferometric gravitational wave detectors are such that the internal mode frequencies are well above the detection bands of the detectors. (Typically, the internal modes have frequencies that are tens of kHz.)

The loss factor associated with the internal modes can be increased by friction occurring between the mass and suspension wire or fibre, as well as by the method used to attach the wire/fibre to the test mass. These problems are addressed in Chapters 3 and 6.

2.8.2 Suspension Modes

In this case, the test mass can be considered to be a rigid body. The most important of these modes are those whose associated thermal noise cause the centre of mass to move. Suspension modes include:

- pendulum modes,

- transverse vibrational (or violin) modes,
- vertical, torsional and tilt modes of the pendulum.

Pendulum Modes

Thermal motion associated with the pendulum mode excited in the direction of the interferometer arm will couple directly into the interferometer signal, reducing the interferometer's sensitivity. This occurs because the thermally induced mirror motion changes the relative separation of the test masses. The suspension can be designed so that the maximum displacement can be forced to occur at frequencies below the lowest frequency of the interferometer's detection band. (See Section 2.7)

Violin Modes

The violin modes of the suspension wires or fibres form a harmonic series that unfortunately lie within the detector's detection band. The loss that is associated with these modes is reduced from that of the intrinsic loss of the suspension wire in a similar way to the loss associated with the suspension modes. If the damping is homogeneous, then the losses due to violin modes and suspension modes are related by equation 2.42

$$\phi_{\text{violin}}(\omega) = 2\phi_{\text{pendulum}}(\omega) \tag{2.42}$$

(when the rocking mode of the pendulum has been constrained [55, 56].)

The thermally induced displacement of the test mass resulting from the violin modes is the noise associated with the violin mode, suppressed by the factor $\frac{m}{m_{\text{wire}}}$, where m is the pendulum mass and m_{wire} is the wire's mass. Off resonance, the displacement is much smaller than motion resulting from the thermal noise associated with the other modes.

Since the suspension is designed to be low loss, most of the thermally induced motion due to the violin modes will be concentrated into very narrow frequency bands around the resonant frequencies. Therefore the only frequencies that will contribute significantly to the overall thermal noise level will be the resonant frequencies. Since the violin modes have low loss factors, the resonant peaks are narrow and hence the amount of the detection band they occupy is small and can be notched out of the resulting data.

Others

The thermal noise associated with the vertical spring modes, torsional modes and tilt modes can be kept to acceptable levels by ensuring that the laser beam is incident with the centre of the face of the suspended test mass.

2.9 Conclusions

One of the main limiting factors to the sensitivities of ground-based interferometric gravitational wave detectors is thermal noise. The fluctuation-dissipation theorem is a very useful equation in determining the levels of the thermal noise. By using the information it provides, interferometric gravitational wave detectors can be designed in ways that will reduce the level of this thermal noise. Prediction of the total level of thermal noise is not as simple as once thought, though. The technique of mode decomposition only works if the test mass is homogeneous. When this is not the case, greater care is required. Consideration instead of how energy transferred to the suspended mass is dissipated is required. And whilst the overall sensitivity of the detectors currently under construction will still be set by the intrinsic losses of the materials from which the suspension is constructed, in future advanced detectors the limit may come from thermal expansion effects within the materials. In particular, this will come into effect if sapphire with its very high intrinsic quality factor,

is selected to replace fused silica in these advanced detectors.

Chapter 3

The Measurement of the Quality Factors of Internal Resonance Modes of Test Samples

3.1 Introduction

The focus of the work presented in this thesis deals with the measurement and the maximisation of the quality factor of the internal resonances of substrates that will be used in the current interferometric gravitational wave detectors, as well as those that may be used in advanced detectors currently under development. In this chapter an overview of how the measurements of these Q's were carried out experimentally is presented, as well as various factors that could limit the measured values and how the effect of those factors was minimised.

3.2 Measurement of Quality Factors

In order to measure the quality factors of the internal resonance modes, a Michelson interferometer was used to measure the motion of a mechanically excited test sample. Since the low frequency bulk movements of the suspended test mass are bigger than the laser wavelength, the interferometer was set up in such a fashion as to allow the lower frequency motion of the mass to be "removed". This was done as follows. (See figure 3.1 for reference.)

One arm of the interferometer was formed by reflecting light off an aluminium mirror, evaporated on to the front surface of the test mass. The second arm was folded by means of two different mirrors. The interferometric signal, detected by the photodiode, was sent through an amplifier and filter system. (Feedback system is detailed in Appendix A.) This filtered signal was then sent back directly to mirror 2 in figure 3.1, which was attached to a piezoelectric actuator. It was also passed through an additional low-pass filter to a loudspeaker attached to mirror 1.

This feedback system allowed the loudspeaker and piezo to follow the low frequency motion of the mass, but not the high frequency thermal motion of the mass's front face. Once this low frequency motion was removed, the interferometer was said to be "locked", and excitation of the resonant frequencies could be carried out.

3.2.1 Detection and Excitation of Resonance Modes

Once the interferometer was locked, the motion of the front face of the test mass could be measured directly. By using a spectrum analyser, it was possible to detect the resonance modes of each mass.

The excitation of the resonances was achieved by means of an electrostatic

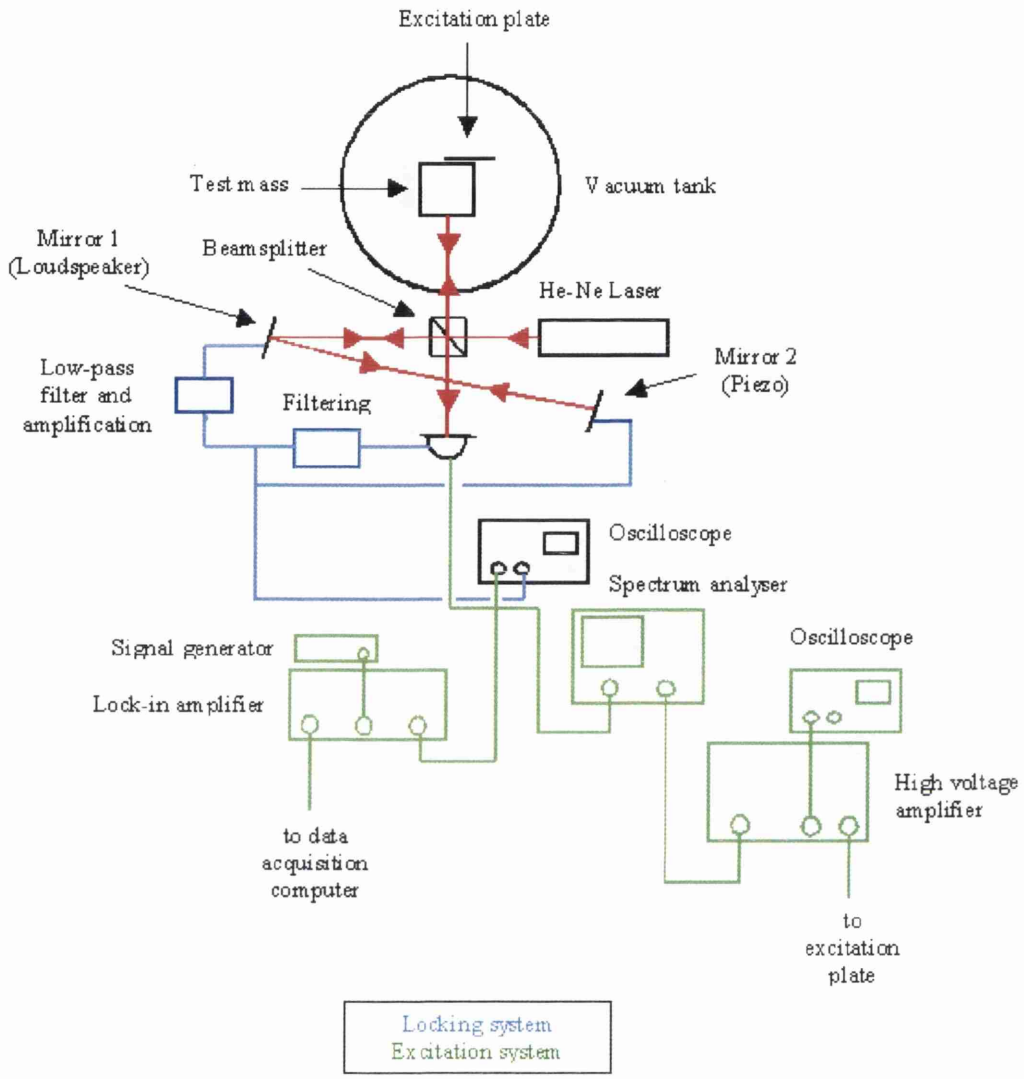

Figure 3.1: *Overview of the locking and excitation systems for the measurement of internal Q values.*

drive plate placed very close to, but not in contact with, the rear face of the test sample. (Typically 3 to 5 mm.) To this pusher was applied a D.C. voltage of roughly 750 V on top of which an A.C. signal was applied, its frequency corresponding to the resonant peak being investigated.

This electrostatic pusher was aligned off-centre horizontally and vertically as this allowed for a wider range of modes to be excited than would be possible

with the pusher directly behind the centre of the mass.

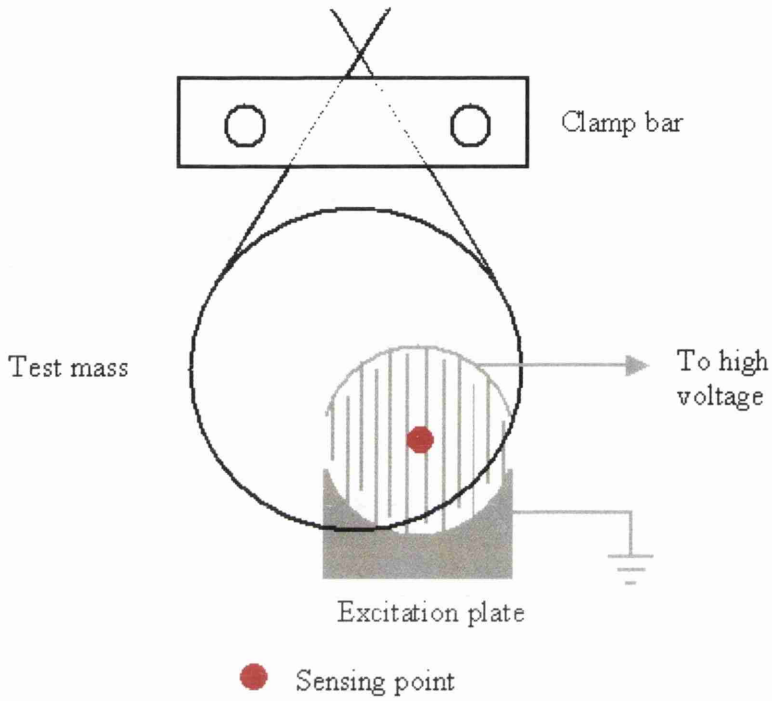

Figure 3.2: *Schematic of excitation plate and of its position, relative to the mass.*

Once the mode had been excited, the A.C. component of the drive was turned off, and the resonance allowed to decay. Since the signal was of the form of a decaying sine-wave, whose frequency was typically in the 10's of kHz range, it was passed through a lock-in amplifier before reaching a data-acquisition system. This lock-in beat the signal down to 5 Hz, low enough for the program to handle. This ringdown signal was then recorded, and the data fed into a spreadsheet that allowed the Q to be calculated. Details of this data acquisition programme are provided in Appendix B.

The full experimental set-up is shown schematically in figure 3.1. The diagram also shows that the suspended mass is contained within a vacuum tank, the laser beam shining through a port-hole to reach the mass's face. Typically, this

vacuum tank is pumped out to a vacuum of between 10^{-4} to 10^{-5} mbars, sufficient to remove the problem of gas damping of the thermal motion of the mass faces caused by the air [57]. The tank can be further pumped out to $\sim 10^{-7}$ mbars, but this took several days and produced no noticeable improvement in the subsequently measured Q value.

3.3 Measuring the Highest Possible Quality Factors

In order for the highest possible values for the internal mode quality factors of the test substrates to be measured, and so give a true indication of the intrinsic quality factor, it is necessary to isolate them as far as possible from the outside world. One way to best achieve this is to suspend the masses under investigation as pendulums.

Initially, two types of suspension were used. The first involved the suspension of the test mass using a single silk thread looped under the mass, the ends of which were clamped to a metal block, which was in turn bolted to a top plate supported on three stiff legs, as shown in figure 3.3.

A second cradle, shown in figure 3.4 was briefly used. This was also based on the suspension of a test mass in a single loop of thread, but the specifics of the design were different. In place of a large top plate supported on three legs, a narrow cross-piece was supported on two trapezoidal steel plates, in turn bolted to a broader base plate. The side plates were drilled out in set places to enable the top plate to be adjusted vertically. It was constructed from steel, and so was heavier and stiffer than the other. However, its size and weight were such that it could not be removed easily from the vacuum tank. In addition, the effectively solid sides meant that it was not as easy to make

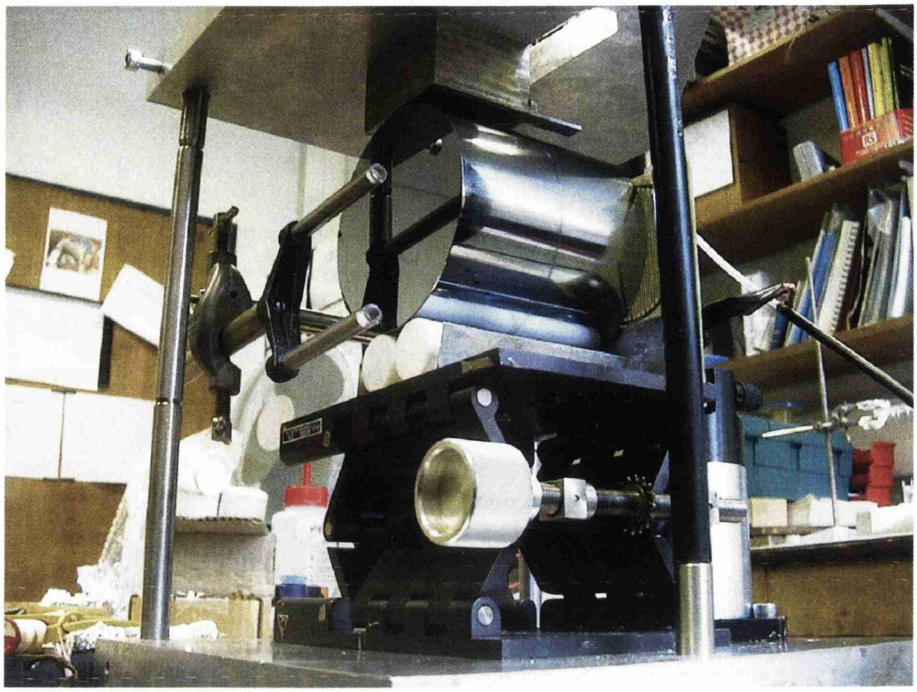

Figure 3.3: *Suspension cradle with Silicon [100] test sample.*

the precision adjustments that were required to ensure the test masses were well balanced. (See later section for the importance of this.) The cradle was, therefore, only used when testing was carried out on a large GEO 600 sized (18 cm diameter, 10 cm thickness) sample of fused quartz, which was too large for the first cradle.

Two different pendulum systems were initially used. The first was a single stage pendulum. Here, the test sample was supported by a single silk thread, passing under the centre of the mass and then crossed over and clamped, just below the cross-over point. In the second system, an intermediate stage was introduced. Here the thread was clamped within a second "mass" consisting of a series of washers held in place on a nut and bolt. The thread was then clamped above this intermediate "mass". The idea behind this two-stage suspension was to increase the isolation of the test sample from outside sources of loss. However, it was found that there was no noticeable improvement in measured quality

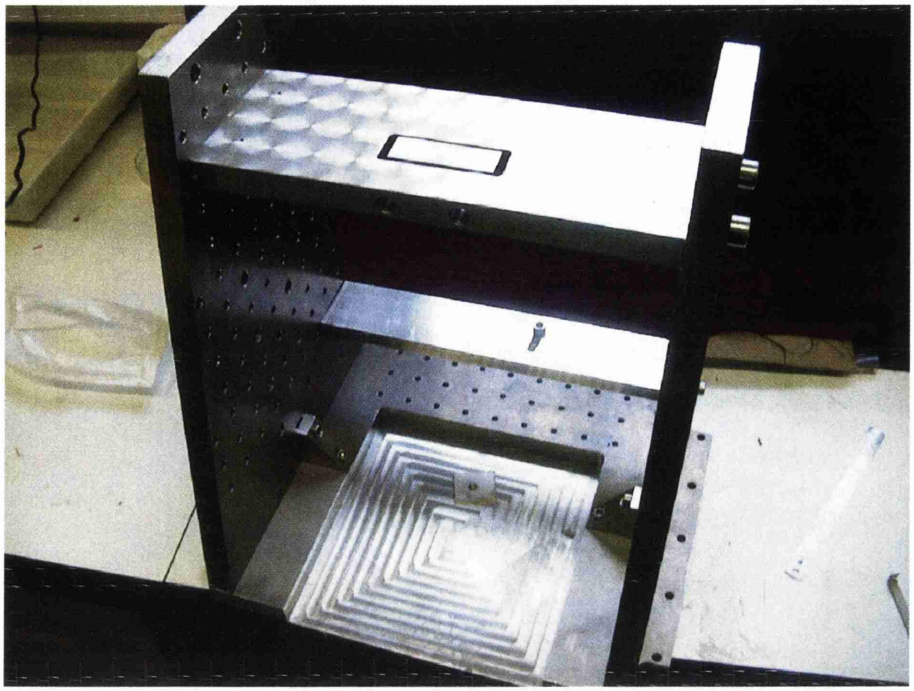

Figure 3.4: *The alternate suspension cradle.*

factors in this system over the first, simpler case. It was therefore decided to focus on the simpler, more practical system. The two systems are shown schematically in figure 3.5.

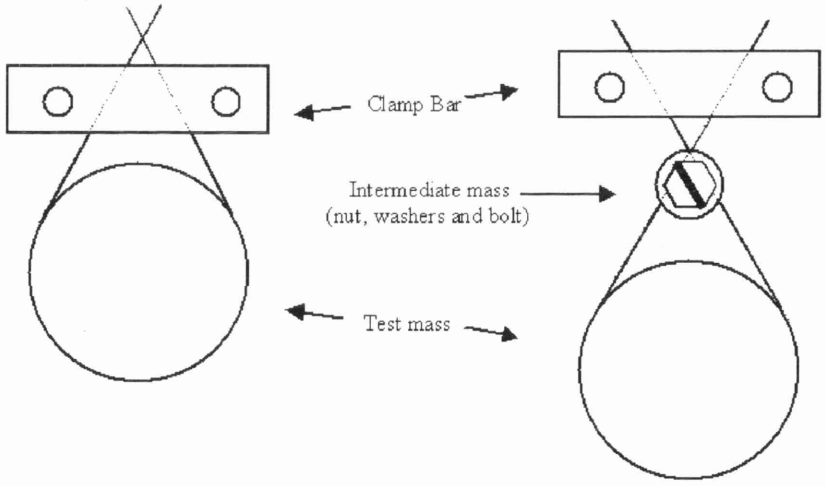

Figure 3.5: *The two different suspension systems used in initial experiments.*

At this stage some consideration of the clamps used to secure the pendulum is necessary.

3.3.1 Alignment and Condition of Clamp

The experiments used a clamp bar that was screwed into a block, both made from aluminium. Throughout the course of the experiments, various clamps were employed to improve the measured quality factors. Initially, a clamp bar of height 1 cm and width 5 cm was used. Consultation with V. Mitrofanov from Moscow State University suggested that reducing the vertical thickness of the bar would be advantageous, as it would allow the separation of mass and the cross-over point of the suspension loop to be reduced. (See the first two pictures in figure 3.6.) This in turn tightens the angle of the suspension wires and so makes the suspension length shorter. (The importance of suspension length is discussed later in this chapter.) With time, though, the faces of the clamp bar and block began to degrade. This was particularly true when wire replaced silk thread as the loop material, as the wire would cut into the clamp. Both block and bar were then replaced. The new bar was only 0.5 cm in height. Its face was partially hollowed out in an attempt to ensure that the clamp bit into the wire at the base and not further up. If clamping occurred higher up, within the clamp, then the wire could rock against the lower side, generating additional loss. This same effect would be caused if the clamp bar and block were not flush with each other. In order to avoid this, guide prongs were attached to the underside of the block, ensuring the bar was correctly aligned.

The various bars are detailed in figure 3.6, and figure 3.7 shows the hollowed out clamp face.

The deterioration of the clamping surfaces with time was corrected by polish-

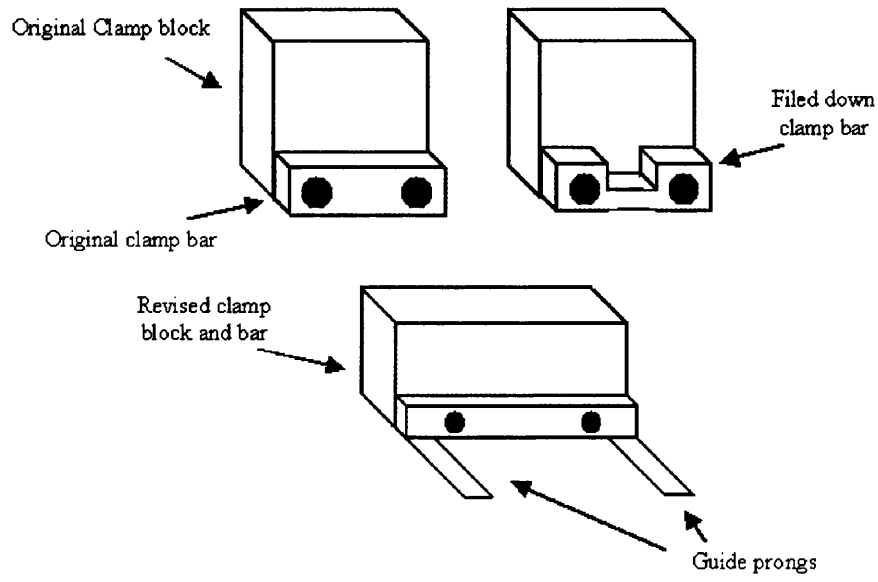

Figure 3.6: *Clamps used for suspending test masses.*

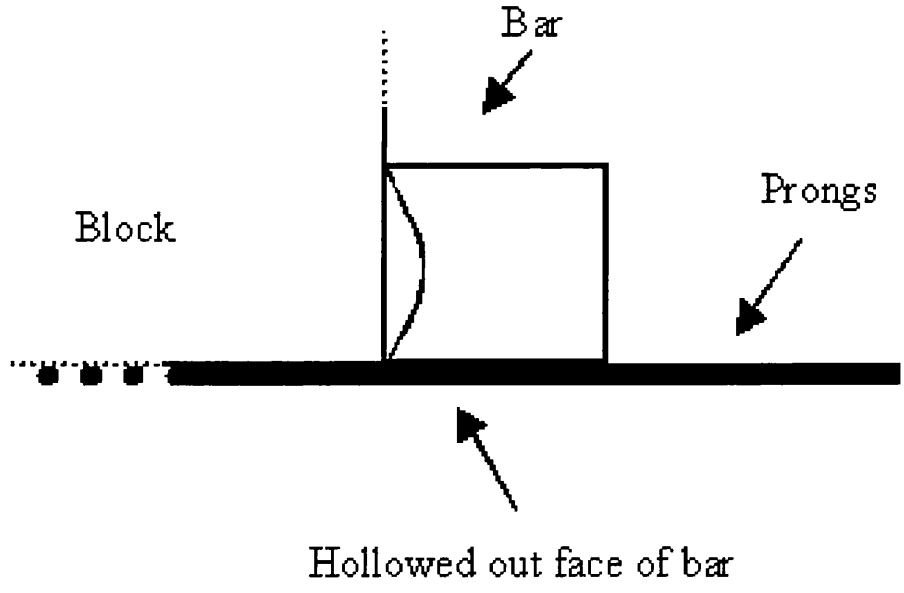

Figure 3.7: *Side view close up of the revised clamp with the hollowed out face.*

ing the surfaces flat or inserting steel shims within the clamp. These shims would protect the clamp faces and could be discarded after each completed suspension.

3.3.2 Suspension Loop

Selection of Suspension Material

The suspension loops were made of a variety of materials, falling into two categories - wires and threads. In most cases, the highest Q values gained for a particular test material were obtained when wire formed the suspension loop. These best results were obtained when the wire, usually tungsten, was polished. This polishing was a multi-stage process. Firstly, the wire was fed back and forth between two pieces of tuffnell coated in diamond paste[1]. This was carried out for typically 10 minutes. The wire was then cleaned with methanol, then fed through metal polish wadding for a further five minutes, before a final cleaning in methanol. Unpolished wire invariably produced poorer results due to friction with the surface of the mass. Figure 3.8 shows the comparison of two pieces of 150 μm tungsten wire, one polished, one not[2]. As can be seen, the surface of the polished wire is noticeably smoother than that of the original sample.

With the thread suspensions, good results could be obtained with less effort - and in certain cases it was found that wire-based suspensions could not match the results obtained for silk suspensions. The threads used were all silk. This had been found to be the best material to use to form the suspension loops [58].

Length of Suspension Loop

It has been shown before that the measured Q value has a dependence on the length of the suspension wire or thread [59]. If the frequency of the internal resonance mode of the test mass is a multiple of the violin modes of the suspension, set by the length of the suspension wire, then the violin mode is

[1]The paste used was grade 3, where the diamond particles are in the 2 to 4 μm range.

[2]SEM picture taken by J. Scott of the Solid State Physics group at University of Glasgow.

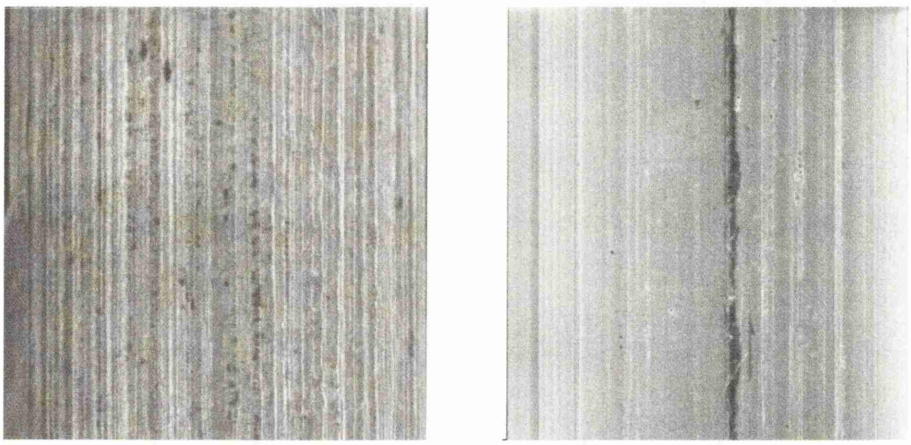

Figure 3.8: *Comparison of unpolished and polished tungsten wire. The original wire was 150 μm diameter. The photograph was taken using a Scanning Electron Microscope, magnification 625.*

excited and energy is lost. This produces an artificially low Q.

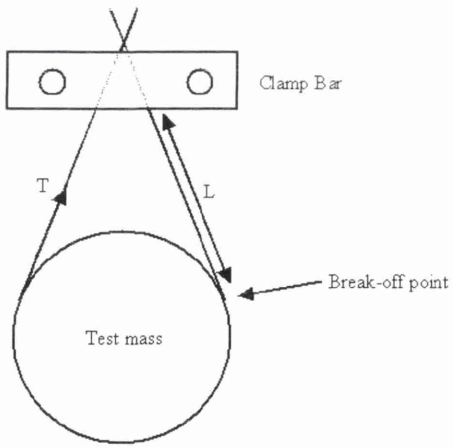

Figure 3.9: *Various parameters in a typical single loop suspension.*

The violin frequencies, ν_n, are calculated using the following approximate expression.

$$\nu_n = \left(\frac{n}{2L}\right)\left(\frac{T}{\mu}\right)^{\frac{1}{2}} \tag{3.1}$$

where n is the number of suspension wires (here taken as 2), T is the tension in the wire, μ is the mass per unit length for the suspension wire and L is that wire's length. This, as shown in figure 3.9, is the distance between the point at which the loop comes away from the surface of the mass (the break-off point) and the underside of the clamp. This relation shows that the violin frequency is inversely proportional to the wire length, L. More importantly, the spacing of the modes, $\frac{d\nu_n}{dn}$, in the frequency domain, is inversely proportional to L. i.e. the shorter the suspension length, the greater the separation (in Hz) of the resonance modes. So by minimising the suspension wire length, the risk of an overlap between the internal modes and multiples of the violin modes is reduced.

Lubrication of Suspension Loop

In their book *Systems with Small Dissipations* [60] Braginsky et al noted that the application of pork fat to the points where the suspension loop was in contact with the test mass decreased the measured losses by a factor of two. The grease acted as a lubricant, reducing the coupling between the suspension loop and the vibrating test mass. In the experiments reported in this thesis some degree of lubrication was employed. Differing types of lubricant were used - predominantly lard (animal fat), though human skin grease and mechanical grease were also used. The latter proved a poor lubricant, and the human grease varied in effect from person to person.

The behaviour described by Braginsky et al was confirmed early on in the experimental work, specifically on a piece of fused silica. When the mass was suspended on a single loop of silk thread, coated in human grease, the Q was found to be $(1.29 \pm 0.05) \times 10^7$. Whilst on the same type of thread, but without the grease coating, the Q was only $(7.36 \pm 0.04) \times 10^6$, a little over half the original value.

Whilst a certain degree of lubrication was desirable, too much proved detrimental. This was highlighted in the case for testing on a sample of gadolinium gallium garnet (GGG). The mass was first suspended on thin silk thread, a small amount of grease applied to the silk. The Q measured was $(1.46 \pm 0.06) \times 10^7$. The next time the mass was suspended, more grease was applied to the thread, resulting in an increase in the Q to $(1.88 \pm 0.03) \times 10^7$. It was then tested a final time, with yet more grease added. This time the Q fell back to $(1.67 \pm 0.02) \times 10^7$. It was therefore important that considerable care was taken when it came to the application of the lubricant. An extreme example for this problem is discussed in the next section. Additionally, there was a practical problem associated with excessive grease. If there was too much grease then the suspension of a sample was made harder as it increased the tendency for it to slip from the loop.

The application of the grease was done as follows. For the case of the suspension wire (or thread), the grease was applied by hand, running the wire up and down through greased fingers. For the mass, a two stage suspension procedure was employed. Here the mass would be hung on a thicker than ideal wire that was coated in grease. Once the mass had been suspended on this wire, the mass was rested on its supports and the wire removed, leaving a grease "track" in the position the actual suspension wire would take. The polished suspension wire would then be positioned on this track and the mass allowed to hang once more.

3.3.3 Condition of Test Mass Under Consideration

Surface Polish of Test Sample

It was found to be important that the condition of the surfaces of the mass at the point of contact was good. Rough surfaces produced friction between

them and the loop, leading to lower Q's. The best results were found for masses with highly polished barrels. This situation was well illustrated for the case of a sample of yttrium aluminium garnet. Initial testing of the YAG cylinder produced a best Q of 2.88×10^7. Once it had been further polished, however, this maximum value increased to 7.26×10^7. Figure ?? shows the range of results measured for the polished sample, compared to the best unpolished result. There is a considerable variation. This variation illustrates the care that must be taken when suspending a test mass. The lower values result from one of the factors discussed previously, or a combination of them.

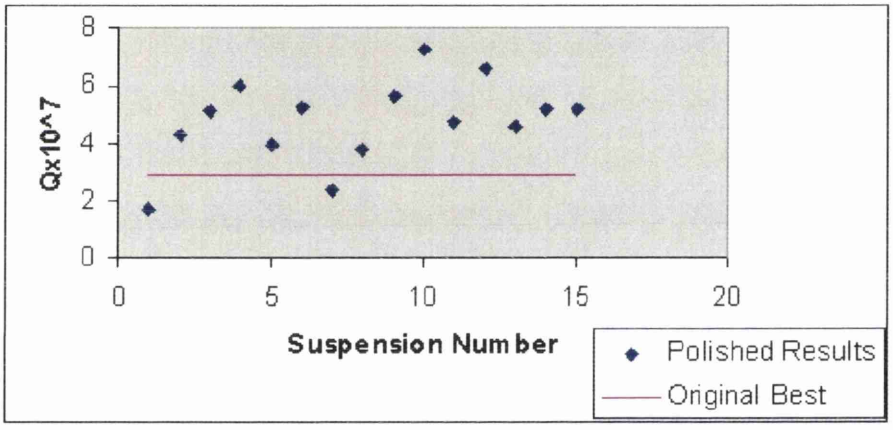

Figure 3.10: *Variation in the measured internal Q of the fundamental longitudinal mode of a polished sample of YAG compared to the best unpolished result.*

Condition of Test Sample

To ensure that the best possible results were measured, each test sample was thoroughly cleaned before each suspension. This cleaning was done by rubbing the surfaces with various liquids, typically acetone, methanol and chloroform. Chloroform was especially good at removing any grease left from the lubrication of the previous suspension wire. The removal of any dust etc, was important since any present on the surface at the time of excitation would

vibrate, providing another source for energy loss. As an extreme example of this, a Corning fused silica mass with three strips of thick grease, three magnets and two break-off bars was tested. Figure 3.11 shows schematically the distribution of the magnets, the grease and the break-off bars, whilst figure 3.12 is a photographic close-up of one of the grease bands.

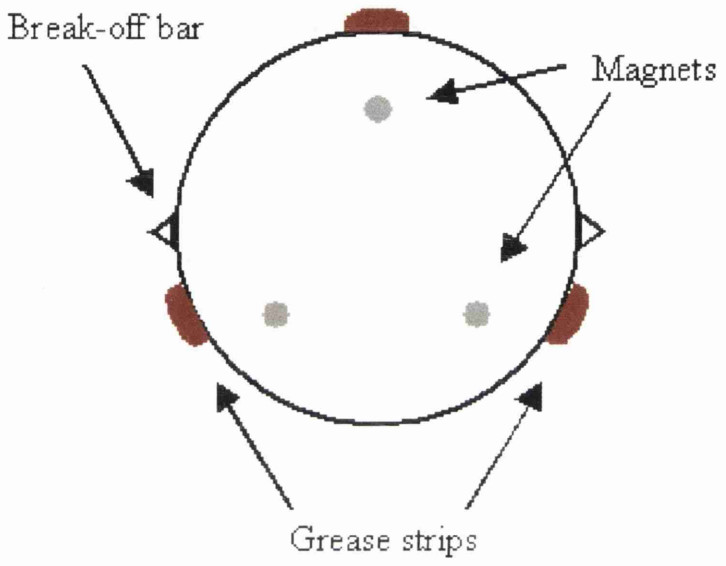

Figure 3.11: *The positioning of magnets, grease and break-off bars on the fused silica mass.*

The positioning of the grease strips put some limitations on the experimental suspension. Specifically, a strip of grease along the top of the mass limited the minimum separation of the mass from the clamp and therefore the shortness of the suspension wires.

Once the mass was suspended and under vacuum, testing could begin. It was measured initially with the grease in place. Then the mass was removed, the grease cleaned off and the mass subsequently retested. There was a marked improvement in the measured results. The fundamental mode, for instance, increased by a factor of ~ 15. All the results, though, were far lower than those

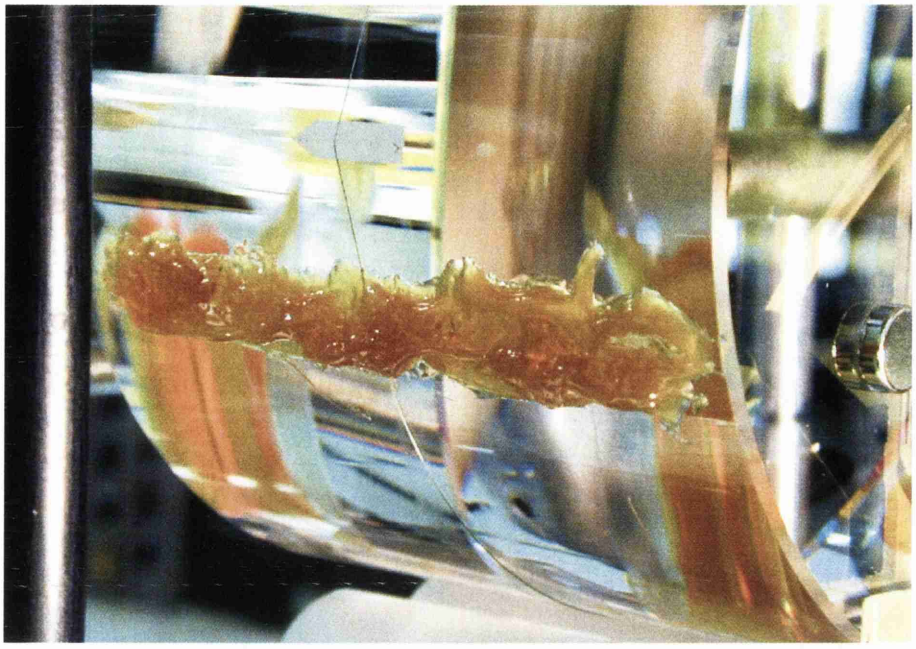

Figure 3.12: *Photographic close-up of one of the bands of grease. One of the magnets is also visible on the rear face of the mass, as is one of the break-off bars above the grease.*

measured for a perfect cylinder with no grease, break-off bars or magnets. All these results are detailed in table 3.1. The results for the uncontaminated mass are not for the same mass, but for an equivalent mass manufactured at the same time as the contaminated one. (The mode shapes are detailed in Appendix C. They are the same as for the coated masses discussed in Chapter 5.) The variation in the degree of degradation of the quality factor is not consistent from mode to mode. This was thought to be the result of the grease strips moving in different ways for each mode: symmetrically away from and towards the centre line for the fundamental, "sloshing" back and forth for the asymmetric drum, for example.

Mode	Frequency (Hz)	Q Full contamination	Q Grease removed	Q Clean cylinder
Bending	22342	1.92×10^3	2.99×10^4	6.29×10^6
Asymmetric Drum	22946	5.21×10^2	2.29×10^4	8.05×10^6
Fundamental	25365	2.62×10^3	3.75×10^4	2.02×10^7
Expansion	31681	8.33×10^2	6.63×10^4	9.91×10^6
2nd Asymmetric Drum	36055	1.41×10^3	1.13×10^5	1.07×10^7

Table 3.1: *Results of Q measurements of modes of a fused silica mass with various degrees of surface contamination.*

3.4 Conclusions

The measurement of high quality factors requires considerable care. It is important that samples under study be isolated from the outside world as far as possible. To achieve this, they are suspended as pendulums that are clamped firmly and smoothly. Selection of the material to form the suspension loop is important. The loop and point of contact should be lubricated to allow as smooth a contact as possible. (In the case of wire loops, polishing the wire further contributes to this.) Care should also be taken with the length of the suspension loop to avoid overlapping with violin resonances in the wire or thread. This is best achieved by keeping the loop as short as possible. Doing so also improves the stability of the suspended mass, ensuring a greater ease for the feedback system to "lock" to the motion of the mass. Finally, the suspended mass should be investigated under vacuum, to remove the problem of gas damping from the air.

Chapter 4

Comparison of Quality Factors of Suitable Gravitational Wave Detector Mirrors

4.1 Introduction

For all long baseline, ground-based gravitational wave detectors, both under construction and being planned, the operating frequency range lies between the pendulum resonances of the suspensions and the lowest internal resonances of the test masses. It is expected that the most significant noise source at the lower end of the operating frequency range will be the thermal noise in the tails of the relevant resonances. (That is the tails above the pendulum resonances and those below the internal mode resonances.) The narrower the resonances, the lower the off-resonance thermal noise.

By definition [61], the narrower the resonance peak, the higher its quality factor Q. In this chapter, the requirements for materials to be appropriate for use in gravitational wave detectors are discussed. Then measurements of the Q's of a range of potential mirror materials are presented and discussed.

4.2 General Requirements for a Suitable Test Material

There are a number of constraints that affect the selection of material for the test masses of long baseline gravitational wave detectors. These are:

1. The material should have a low loss factor (high Q) at room temperature.

2. It should have a high thermal conductivity and low thermal expansion in order to minimise mechanical distortion when heat is deposited in it by the laser beam illuminating the interferometer. [62]

3. The material should be transparent and have very low optical loss at the wavelength of the laser light to minimise heat deposited. [62]

4. If possible, it should have a low value of change of refractive index with temperature to minimise thermal lensing effects for transmitted laser beams. [62]

5. The material should be suitable for coating and polishing to sub-angstrom surface roughness.

6. It should be possible for the material to be produced in sizes suitable for the detectors, up to a mass of several tens of kg to reduce photon recoil effect and the effects of the Heisenberg Uncertainty Principle.

7. Finally, the material should have oxidised aluminium or silicon in the makeup so that it chemically reacts with the alkali metal hydroxides and thus can be bonded to suspension elements by the low loss hydroxide-catalysis bonding technique. [57, 63]

There are few materials that have a low enough mechanical loss at room temperature to be of any use in gravitational wave detectors, and these tend to be very pure glasses such as fused quartz or fused silica, or single-crystal materials such as sapphire and silicon.

Experiments in a number of laboratories [46, 49, 64, 65] have suggested that the Q's in fused silica, which is synthetic in origin, range between 5 x 10^6 and 5.7 x 10^7 and are higher than those in fused quartz (natural in origin) by a significant factor. Therefore it is fused silica (manufactured by Heraeus or Corning) that is being used as the test masses for LIGO [26], VIRGO [27], GEO 600 [66] and TAMA 300 [28].

Silica is also attractive because of potentially high optical quality, size of pieces available, ease of polishing and coating, and low optical absorption loss [67] in some types such as Suprasil SV from Heraeus. However, the Q of fused silica will put a limit on the thermal noise performance achievable with current detectors, and thus to improve the performances of future detectors different materials with higher Q's are likely to be needed.

Such a material that has been studied for a number of years is sapphire (Al_2O_3). Very high Q values, up to 3 x 10^8, have been measured in Russia from samples grown using the horizontal oriented crystallisation process [60]. However, for pieces to be grown to the sizes and optical quality required for gravitational wave detectors, the Heat Exchanger Method (HEM) [68] must be used. Results from Australia [69], though, had only yielded Q's of roughly 5 x 10^7, considerably lower than for the horizontal oriented crystallisation pieces from Russia, and little better than the results for fused silica. Further work on HEM samples was therefore needed, and this work is reported in section 4.4. Also reported are confirmation of the performance of fused silica and the results of tests carried out on other materials whose losses were not fully known, such as

spinel (magnesium aluminium oxide) and YAG (yttrium aluminium garnet).

4.2.1 Difficulties in the Manufacturing of Sapphire Samples

Sapphire made by the HEM process is grown most easily along the *a* and the *m* crystallographic directions and thus the largest diameter cylindrical pieces available have their axes in these directions. It should be noted that the crystal structure of sapphire results in anisotropy of its mechanical properties along the two axes at right angles to the growth axes of these boules. (See figure 4.1[1].) Both the inhomogeneity and birefringence of the uniaxial crystal may lead to constraints on the use of such cylinders as test masses for gravitational wave detectors [70]. If these effects prove insurmountable, the use of pieces of sapphire cored out along the *c* axis should get around these problems and the development of pieces of adequate size is currently under investigation for the LIGO project.

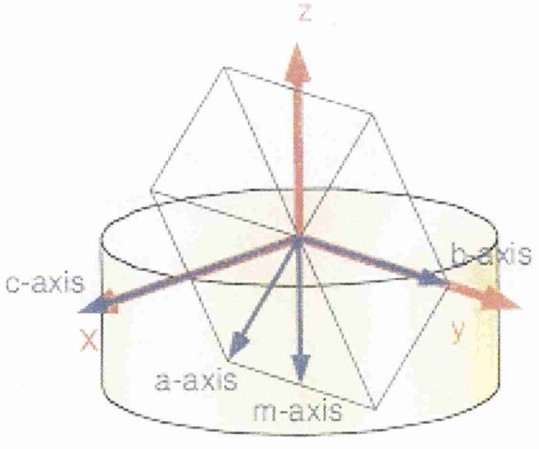

Figure 4.1: *Axes of a sapphire sample grown along the m-axis.*

[1]The diagram was drawn by K. Numata from the Department of Physics, University of Tokyo.

Measurements of the quality factors at very high frequencies (GHz) have shown that materials such as YAG and spinel can have Q's of the same order, if not higher, than sapphire [71]. These crystals are broadly similar to sapphire in mechanical properties, but are more symmetrical in crystal structure and have the advantage over sapphire of being optically isotropic, thus removing any complexity associated with using a material with inherent birefringence as a transmissive optic. The samples of YAG and spinel tested and reported below had resonances much closer in frequency to those of interest for gravitational wave detectors, therefore the results are of considerable interest.

4.3 Measuring the Quality Factor, Q, of a Damped Harmonic Oscillator at the Resonant Frequency of One of its Modes

The fluctuation-dissipation theorem allows all thermal noise sources to be treated in a similar way. If there are a number of different sources of dissipation present in a system, both internal and external, they can be considered by including their combined effects in an overall expression of the impedence of the systems as a function of frequency. The total dissipation of a given system, at a frequency ω, is effectively the sum of all the individual loss angles, i.e.

$$\phi_{total}(\omega) = \phi_1(\omega) + \phi_2(\omega) + ... + \phi_n(\omega) \tag{4.1}$$

By measuring the total loss factor exhibited by the suspension at an angular frequency ω_0 (the resonant frequency of one of the suspension's modes), and knowing the functional form of the internal loss mechanism, the level of the loss factor at a frequency ω can be determined. Substitution of this loss factor, along with the relevant parameters of the test mass into the fluctuation-

dissipation theorem allows the prediction of the thermal noise, at frequency ω, within the suspension. In this section, one method for measuring the loss factor is discussed. This method was used in the determination of the quality factors presented in this thesis.

Consider the excitation of a normal mode by some means. The mode is then allowed to decay freely, subject to the losses present in the system. The displacement of the mode can be represented by

$$x(t) = x_0 e^{-\frac{1}{2}\phi_{total}(\omega_0)\omega_0 t} e^{i\omega_0 t} \tag{4.2}$$

where $x(t)$ is the amplitude at time, t; x_0 is the initial amplitude; ω_0 is the resonant angular frequency of the mode and $\phi_{total}(\omega_0)$ is the combined effect of the loss mechanisms present. The loss can be determined by measuring the amplitude decay envelope of the free oscillations as a function of time.

Consider the amplitude decay term in equation 4.2:

$$A(t) = x_0 e^{\frac{1}{2}\phi_{total}(\omega_0)\omega_0 t} \tag{4.3}$$

This can be rearranged as

$$\phi_{total}(\omega) = \frac{2\ln(x_0/A(t))}{\omega_0 t} \tag{4.4}$$

If the relaxation time, τ taken for the amplitude to decay to $A(t) = x_0/e$ is measured, then equation 4.4 reduces to

$$\phi_{total}(\omega_0) = \frac{2}{\omega_0 \tau} \tag{4.5}$$

which is the reciprocal of the quality factor, $Q(\omega_0)$. (See French [48].) Again,

it is seen that $\phi(\omega_0) = 1/Q(\omega_0)$. Using this relation, equation 4.4 can be rewritten as

$$Q(\omega_0) = \frac{\omega_0 t}{2\ln(x_0/A(t))} \tag{4.6}$$

Since the parameters measured in the experiments are $A(t)$ and t, it is more useful to express equation 4.6 in the form

$$\ln(A(t)) = -\frac{\omega_0}{2Q}t + \ln(x_0) \tag{4.7}$$

which has the form of a straight line when the natural logarithm of the amplitude, $A(t)$, is plotted against the time, t. By calculating the gradient of the resulting graph, the Q can be evaluated at the resonant frequency using the expression

$$Q = \frac{\omega_0}{2 \times \text{gradient}}$$

These calculations were performed initially by hand and subsequently using an Excel spreadsheet, the details of which are provided in Appendix B.

4.4 Measured Quality Factors of Suitable Gravitational Wave Detector Test Materials

The experimental apparatus was as detailed in Chapter 3. To give an idea of the methodology and approach employed in the testing of these masses, a "case-study" of the testing carried out on one of the samples (a chromium-doped sapphire cylinder) is presented first. In the sections which follow this, a range of samples tested are discussed. For simplicity, these have been grouped into three parts:

- Fused silica and quartz samples
- Sapphire samples
- Other materials

The samples tested were typically cylindrical, their diameters ranging from 2.5 cm to 18 cm, their lengths from 3 cm to 11 cm.

4.4.1 Case-study: The Testing of a Chromium-doped Test Mass

The work detailed here deals with the investigation of a cylindrical sample of sapphire, 2.5 cm in width and 10.9 cm long. The sample was chromium doped, giving it a pink-ish look, and was lent to Glasgow University from Moscow State University. There were two periods of testing. The first was in January 1999, with the mass suspended a number of times until the best Q value was determined. It was subsequently re-tested in June of that same year after a visit from V. Mitrofanov from Moscow State University. During his visit to Glasgow, refinements were made to the techniques used in carrying out the suspensions. These techniques had given rise to the highest Q's ever measured in the West (as detailed later in this chapter) and so the "pink" mass was re-tested to see if these technique refinements might result in an improvement in the best quality factor measured for it.

First Period of Testing - January 1999

At this time, the experimental technique as regards the detection of resonances within the test mass was as detailed in Chapter 3, a Michelson interferometer used to interrogate the front face of a suspended test mass and an electrostatic plate used to excite the modes. The subsequent decaying ringdowns, though,

were recorded on a chart recorder, rather than a data acquisition computer. (See Appendix B for more information on the chart recorder.)

To suspend the test mass, a silk thread was clamped into a loop and the mass then fed through this loop. The position of the mass within the loop would then be adjusted until it hung approximately horizontally. A support for the mass was then jacked up under the mass to hold it whilst the suspension cradle was transferred to the vacuum tank. Once in position, the support would be lowered once more and the final, precision adjustments to the suspension loop made. With the mass hanging level, the vacuum tank would then be closed and evacuated to a pressure in the 10^{-5} to 10^{-6} mbars region. This was the procedure carried out in each of the suspensions detailed below.

Suspension 1

Prior to suspension within the loop, Radiospares [72] "multi-purpose" grease was applied to the mass by rolling the mass over a greased thread. The mass was then hung on 100 μm stainless steel wire. At a pressure of 4×10^{-6} mbars, the Q was found to be $(1.93 \pm 0.03) \times 10^7$.

Suspension 2

For this suspension, an intermediate mass was added to the suspension loop. This was in the form of two washers and a nut and bolt, screwed tight over the thread, the cross-over point being just above the bolt, inside the washers. The thread was then clamped above this point using the original clamp bar (figure 3.6). This time the thread was lubricated with skin grease. The results obtained were $(2.18 \pm 0.07) \times 10^7$ at a pressure of 3×10^{-6} mbars and $(2.2011 \pm 0.0007) \times 10^7$ at a slightly better vacuum. These were to ultimately prove to be the best results obtained, but this was not known at the time.

Suspension 3

Once more, the silk thread was human-greased. The intermediate mass was removed again, and not used again until *Suspension 9.* Result - $(6.5 \pm 0.3) \times 10^6$ at 5×10^{-5} mbars.

Suspension 4

A different silk thread was chosen for this attempt, again coated in skin-grease. Up until this stage, the mass had been supported from underneath by a pair of triangular steel prisms mounted on a jack. These could be raised into position to fix the mass in place, then lowered again when the cradle was in place. The mass under examination would rest in the "valley" created between the prisms. At this stage, this support was changed to two steel cylinders, again designed to sit either side of the mass. These had been constructed with a central groove to help position the suspension thread. At a pressure of 2×10^{-5} mbars the Q was found to be $(1.55 \pm 0.03) \times 10^7$.

Suspensions 5 - 8

At this stage, industrial grease was applied to the barrel of the cylinder about the point of contact. Over these four suspensions, the length of the loops were varied over a range of 2 cm and the level of grease on mass and thread varied. These tests resulted in Q's ranging from $(1.14 \pm 0.01) \times 10^7$ (at a pressure of 2×10^{-5} mbars) to $(1.54 \pm 0.01) \times 10^7$ (at 3×10^{-5} mbars).

Suspension 9

After the second suspension, the thread and washer employed to form the loop had been preserved. It was decided to return to these now to see if the Q really had deteriorated or whether the suspensions tried had just not been ideal. At a pressure of 3×10^{-5} mbars, the Q was found to be $(1.81 \pm 0.06) \times 10^7$ and later, when the pressure had fallen to 2×10^{-6} mbars it was $(1.89 \pm 0.07) \times 10^7$. The tank was then re-opened, the mass position adjusted and the tank repumped.

This time the Q was $(1.83 \pm 0.01) \times 10^7$ at 2×10^{-6} mbars. Whilst these values were still lower than those previously measured, they were considerably better than the most recent results. The reduction in Q from the previous value for this loop was decided to be most likely a result of the thread having been left out for some time and its condition was unlikely to have been as good as it had been at first.

Suspensions 10 - 13

Retaining the intermediate mass, various combinations of suspension loop threads were tried with a combination of skin grease from different people. This approach yielded a range of Q's from $(1.65 \pm 0.02) \times 10^7$, at 2×10^{-5} mbars, to $(2.07 \pm 0.07) \times 10^7$, at 3×10^{-6} mbars. The choice of grease appeared to be the main factor affecting this variation.

Suspensions 14 and 15

After the tank was opened at the completion of *Suspension 13* it was lifted up and the intermediate mass was clamped directly between clamp bar and block. This yielded a Q of 1.67×10^7 at 2×10^{-5} mbars. The tank was then reopened and the clamped tightened as hard as possible. This had the effect of increasing the Q to $(1.72 \pm 0.04) \times 10^7$ at 3×10^{-6} mbars.

Suspensions 16 - 21

Various combinations of grease, suspension length and loop material were tried, but no improvement in the measured quality factor were observed. The support jack was also removed entirely, in case any charge on it was damping the mass. This made no noticeable difference, and increased the risk of damage to the mass should it slip from its suspension loop. The jack was therefore not removed again. As a final attempt, a new version of the intermediate mass was created - following the same design - but this yielded a result of only $(1.73 \pm 0.02) \times 10^7$ at a pressure of 2×10^{-5} mbars. Since the maximum Q

appeared to have been found, testing ceased at this stage.

Second Period of Testing - June 1999

When V. Mitrofanov visited, he suggested several alterations/refinements to the techniques employed to measure the internal quality factors. The first was to reduce the thickness of the clamp bar so as to further minimise the separation of the mass from the cross over point of the suspension thread, thus tightening the angle of that loop. He also recommended a change to how the mass was put into the loop. Until this time, the loop had been created first and the mass fed through it. If the loop was greased, this would result in grease being applied to the sides of the mass which would then have to be cleaned off. Now, though, the thread was placed in the groove in the support blocks first, and the mass then placed above it. The thread would then be pulled up about the mass and clamped to form the loop. This ensured that any grease on the thread would remain in a narrow region about the line of suspension. Finally, it was recommended that a teflon stick was used to make any final adjustments to thread position when suspending the mass. This material would not damage the surface of the mass, nor would it leave behind any deposits. Using this refined procedure, Q's well in excess of 2×10^8 were measured on a piece of HEMEX sapphire (see later section). The chromium-doped mass was therefore retested to see if any improvement could be measured. (It was also found that a vacuum of 1×10^{-4} mbars was sufficient to result in high Q's. This reduced the time taken for each suspension considerably.)

Suspensions 1 and 2

The first run used an ungreased silk thread, Russian in origin. To the mass a track of lard was applied. The mass/clamp separation was about 0.5 cm. At a pressure of 1×10^{-4} mbars the Q's were $(1.73, 1.79) \times 10^7$. An alternate silk thread, thinner than the Russian one was then used, again ungreased.

Lard was once more applied to the mass. The level of grease and separation of mass and clamp were roughly the same as above, but the Q came out at $(1.19 \pm 0.08) \times 10^7$ at 7×10^{-5} mbars.

Suspensions 3 - 6

Much as had been done in the first period of testing, various combinations of greases and lengths were then tried, resulting in Q's of $(1.71 \pm 0.02) \times 10^7$ to $(2.10 \pm 0.11) \times 10^7$, both at 8×10^{-5} mbars.

Suspensions 7 - 9

At this stage it appeared that results were approaching the same level as before. It was therefore decided to try another of Mitrofanov's suggestions. Whilst up till now silk threads had been found to produce the best results, Mitrofanov preferred well-polished metal wires, specifically tungsten. So, a length of 100 μm was polished using diamond paste applied to tufnel blocks. Upon testing, this produced results of $(2.21 \pm 0.04) \times 10^6$ at 5×10^{-5} mbars, which were very poor. Another attempt with the same thickness of wire produced only poorer results, but when 50 μm tungsten was used instead, the Q returned to $(1.89 \pm 0.06) \times 10^7$ (6×10^{-5} mbars).

At this point it was decided that further testing was unlikely to yield higher quality factors, and testing ceased once more. Whilst the techniques Mitrofanov had provided did not have a noticeable affect on the results for this mass, they were adopted for all masses from that time on since they were more practical than earlier methods. (And for the case of wire polishing, it would lead to considerably better results for other masses.) The fact that the results for the first period of testing were on a par with the later set meant that other results found at that time could be considered as an accurate estimation for those material's intrinsic quality factors.

Summary

In order for the best possible quality factors to be measured when testing a sample suspended by a loop it is very important that great care is used. If the loop is silk thread, then it should be coated in grease to obtain the best results. If the loop is a wire, then in addition to the grease, it must be polished if high Q's are to be recorded. Choice of lubrication grease is also important - mechanical grease is a poor option, animal-based grease (e.g. lard) being far more favourable. To avoid unnecessary contamination of the sample's barrel surface the loop should be formed about the mass, then clamped. Creating the secured loop first results in grease contacting areas of the mass where it serves no beneficial purpose. Positioning of this suspension loop is made simpler by employing a suspension block that marks the central position of the mass, about which the loop will be slung. To make subsequent fine adjustments of this loop once it has been secured, a stick made from a material that will not contaminate the surface of the mass or wire/thread is best, for example teflon. It can also be seen from this case-study that use of intermediate stages in a suspension are not as important as the steps listed above, applied with great care. Patience is also important - rarely will the best result come about from the first run for a particular sample.

4.4.2 Fused Silica and Fused Quartz Test Samples

In table 4.1, the different types of fused silica, their dimensions, their method of suspension and the measured Q values for their fundamental longitudinal resonant modes are summarised.

Corning Samples

A total of five fused silica test samples manufactured by Corning [73] were tested, three 7940 and two 7980. The results quoted in table 4.1 were the best

Fused Silica Type	Frequency (Hz)	Dimension (diameter x length - cm)	Suspension material	Q (x 10^7)
Corning 7940	40456	6.5 x 7	Silk thread	2.39 ± 0.01
Corning 7980	25378	12.5 x 10	150 μm Tungsten	1.53 ± 0.4
Suprasil (i)	39381	6.5 x 7	Silk thread	0.420 ± 0.016
Suprasil (ii)	39342	6.5 x 7	Silk thread	0.403 ± 0.005
Infrasil	39393	6.5 x 7	Silk thread	0.325 ± 0.040

Table 4.1: *Results of Q measurements of the fundamental longitudinal mode for a range of fused silica samples.*

for each type. Whilst each individual mass exhibited a unique best value for its internal Q, they were all in excess of 1×10^7. This further confirmed the value in using fused silica for GEO 600 and the other modern gravitational wave detectors. Other types, though, proved to be of lower Q

Suprasil Samples

Suprasil[2] (i) was not a simple cylinder in design. As detailed in figure 4.3 it had two flats polished on the sides. To these flats, triangular break-off prisms had been bonded. These defined the break-off point of the suspension fibre or wire, but presented practical problems with regards to the suspensions. So sharp where the prisms that the usual silk threads would often break when they became tensioned. Great care was therefore required. Various orientations of this mass were tried, putting the prisms to the sides, or the top and bottom. Doing so varied the measured Q's, the highest value obtained being $(4.20 \pm 0.16) \times 10^6$ with the break-off bars on top and bottom.

[2]Suprasil is a form of fused silica manufactured by Heraeus [74]. There are a range of types available, the ones here being type 2.

Figure 4.2: *Suprasil test mass.*

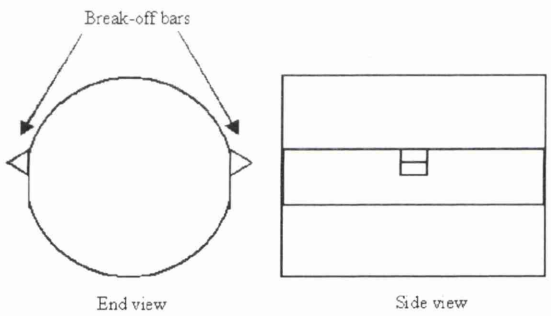

Figure 4.3: *Suprasil test mass with break-offs.*

Suprasil (ii) was a plain cylinder. When it was first tested, the barrel was rough and cloudy. When tested, the Q was found to be $(3.06 \pm 0.06) \times 10^6$. It was then sent to Heraeus for barrel polishing. Figure 4.2 shows the repolished cylinder. When it was returned, it was tested again. The Q for the fundamental mode had now increased to $(4.03 \pm 0.05) \times 10^6$. Other resonant modes were then investigated. Most yielded Q's lower than that of the fundamental longitudinal modes, with the exception of one of the bending modes, frequency 31709 Hz, which gave a Q of $(5.79 \pm 0.04) \times 10^6$. These results were still considerably less

Fused Quartz Type	Frequency (Hz)	Dimension (diameter × length - cm)	Suspension material	Q ($\times 10^6$)
GEO 600 Sized	29211	18 × 10	Nylon thread	1.73 ± 0.15
Small cylinder (i)	40051	6.3 x 7	Silk thread	1.40 ± 0.02
Small cylinder (ii)	40069	6.3 x 7	Silk thread	1.35 ± 0.03
Bonded sample	39727	6 x 7	Silk thread	1.81 ± 0.06

Table 4.2: *Results of Q measurements of the fundamental longitudinal mode for a range of fused quartz.*

than the Corning samples, and it was concluded that the samples were simply of poorer quality.

Infrasil

Only one sample of Infrasil[3] was tested. This was of the same dimensions as the sample shown in figure 4.2. Its fundamental longitudinal mode had a Q of $(3.25 \pm 0.40) \times 10^6$, suggesting that it was of poorer quality than the other fused silica samples tested.

Fused Quartz

It is very clear from the results in table 4.2 that fused quartz has a far lower quality factor than fused silica, though the condition of the samples tested was not ideal as they had been used for other applications. The GEO sized piece had two broad flats polished on to its sides and its larger bulk made extensive testing prohibitive. The bonded sample[4] was an old piece that had

[3]Infrasil is another type of fused silica manufactured by Heraeus [74]. Two types are available, the one tested here being Infrasil 301.

[4]Heraeus grade HOQ310

been used as part of work carried out to determine the effect of silicate bonding on the losses of a test mass [57]. It had a flat polished along the top of the mass. It should be noted, though, that the result obtained for the fundamental longitudinal Q (1.81×10^6) was higher than that measured at the time of the original testing (1.40×10^6). This was probably a sign of improvements made to the experimental techniques employed, or possibly through the sample's bond maturing with age. The two remaining fused quartz samples, labeled "small cylinder (i) and (ii)", were tested as part of work to determine the effect of sodium silicate bonding. The samples were nominally identical, and they yielded similar quality factors. Both masses, though, showed signs of surface scoring. More discussion of the testing on these masses is presented in Chapter 6.

4.4.3 Sapphire Test Samples

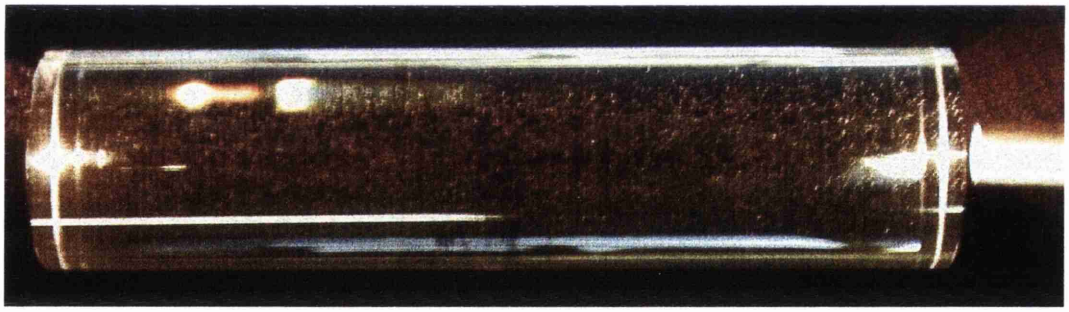

Figure 4.4: *Picture of one of the Russian sapphire samples, illuminated along its axis.*

In table 4.3, the different types of sapphire, their dimensions, their method of suspension and the measured Q values for their fundamental longitudinal resonance modes are summarised.

Sapphire sample	Frequency (Hz)	Dimension (diameter x length - cm)	Suspension material	Q (x 10^7)
HEMEX Cylinder	53591	3 x 10	50 μm Tungsten	25.9 ± 0.5
Russian (i)	37849	3.5 x 13.8	Silk thread	10.17 ± 0.35
Russian (ii)	47352	2.5 x 10	Silk thread	12.80 ± 1.17
"Pink"	47377	2.5 x 10	Silk thread	2.2011 ± 0.0007
HEMEX "Coin"	82992	8 x 3	Silk thread	5.24 ± 0.12
HEMEX Hexagonal	66947	3 x 7.5	Nylon thread	0.251 ± 0.019

Table 4.3: *Results of Q measurements of the fundamental longitudinal mode for a range of sapphire samples.*

The Best Sapphire Samples

In their book *Systems with Small* Dissipations [60], V.B. Braginsky, V.P. Mitrofanov and V.I. Panov reported results from tests they had carried out on samples of sapphire. These masses had yielded Q's in the region of 4×10^8 and set a standard not repeated for years. In the summer of 1999, V. Mitrofanov came to Glasgow University to aid in the work being carried out there. With him he brought some of the masses that had been tested back in the 1970's. It was hoped that by testing them it would be possible to determine whether the experimental set-up in Glasgow was suitable to measure Q's as high as those measured in Russia. Until these masses came to the Glasgow laboratory, the highest internal mode Q's that had been recorded were in the region of 3×10^7 [75]. After implementing minor changes to the set-up, as detailed in section 4.4.1, the Russian samples were tested. As table 4.3 shows, results were obtained of $(1.02 \pm 0.04) \times 10^8$ and $(1.28 \pm 0.12) \times 10^8$. Whilst this was lower than the original Russian results, this difference was put down to "wear and tear" on the masses since their original testing over twenty years before. Specifically, the samples had been damaged and repolished since the original

testing. This was thought to have created stresses within the masses. Since these high quality factors were measurable, a new cylindrical sample was investigated. This was an American sample, made by Crystal Systems [76] using a Heat Exchanger method. The company makes a range of sapphire grades. All those measured in these experiments were classed as HEMEX, their best quality. This mass yielded a quality factor for the fundamental longitudinal mode of $(2.59 \pm 0.05) \times 10^8$ which was the highest internal Q measured outside of Russia, thus showing that it was possible to manufacture samples that were as good as the naturally grown Russian pieces.

Hexagonal Sapphire

This was a unique test sample. Of length 8 cm, the cross section of this mass was hexagonal, of side 1.8 cm, one of which was ground. When first suspended, the sharp corners between the faces would cut through the silk thread employed in the suspensions. However, nylon thread could hold the mass, and this allowed the result quoted in table 4.3 to be recorded. The suspension problems led to the development of an alternative. Instead of hanging the mass in a loop, an attempt was made to balance the mass on the back of a aluminium cylinder lying at right angles to the sapphire mass. However, the best Q measured in this condition was only 5.6×10^5 so this method was quickly abandoned. This very low Q, especially in comparison to the other HEMEX sapphire samples, was thought to be the result of the flat faces about which the suspension loop was slung. As opposed to a smooth, continuous surface, as is the case for cylindrical barrels, this loop was effectively broken into sections by the corners between the faces. This prevented the loop from sitting as flush to the barrel as is normally the case, allowing for the possibility of violin mode vibrations along each of the sections. Additionally, the edges damaged the nylon thread at the corners. This was visible when the thread was removed after suspension - at the points corresponding to the corners the nylon was dented.

Other Sapphire Samples

The "Coin" sapphire sample was so called because of its dimensions (7.5 cm diameter by 3 cm thick). It was tested as part of work to investigate the effects of a dielectric mirror coating on the losses of a test sample. Like the very good HEMEX sapphire sample, this mass was manufactured in the same way. Its considerably poorer Q, though, was thought to be due to the poor polish on the barrel - it had a mottled appearance. This work is discussed in greater detail in Chapter 5. The testing of the "pink" sapphire is discussed earlier in this chapter.

4.4.4 Other Test Samples

Material	Frequency (Hz)	Dimension (diameter x length - cm)	Suspension material	Q (x 10^7)
YAG	38291	2.5 x 10	Silk thread	7.26 ± 0.04
Spinel	66196	2.5 x 10	Silk thread	0.80 ± 0.07
Silicon [100]	39949	9.8 x 10	Silk thread	1.41 ± 0.02
Silicon [111]	43186	9.8 x 10	Silk thread	1.30 ± 0.03
GGG	67297	2.5 x 6	50μm Tungsten	2.62 ± 0.06

Table 4.4: *Results of Q measurements of the fundamental longitudinal mode for a range of other materials.*

In table 4.4, the materials, their dimensions, their method of suspension and the measured Q values for their fundamental longitudinal resonant modes are summarised.

The quality factors for both the YAG and spinel are lower than that for sapphire, but are still encouraging since they are in the $\times 10^7$ region. Initially,

when the YAG was tested, it achieved a Q of only 2.9×10^7. It was observed that the surface qualities of the YAG and spinel samples appeared different from that of the sapphire or the fused silica samples normally tested. Examination of the YAG and the sapphire under an atomic force microscope suggested that the roughness of the sapphire sample over a scale of approximately 40 microns was around 10 nm rms over a spatial bandwidth of approximately 6 cycles per micron, whilst the roughness of the YAG sample was close to two times greater than this, with the addition of many scratches of 80-90 nm depth separated by around 2 microns. It was therefore sent for polishing, and subsequent testing produced the result in table 4.4. The surface of the spinel sample was broadly similar to that of the YAG, but it also had many pits and surface tearouts, roughly 20 nm deep by 20 μm wide, seemingly due to material flaws that occurred during polishing. Unfortunately, it was not possible to re-polish the spinel in the same way as the YAG, but it is believed that its Q would have shown a similar improvement.

The gadolinium gallium garnet (GGG) sample produced results comparable to those measured in the good fused silica samples, though it is unclear whether samples of the required size and consistency could be produced at this time.

Investigating Different Resonant Modes - Silicon Test Samples

Up to this stage, the quality factors presented have been for the fundamental longitudinal mode. In this section, some aspects of other internal resonant modes is discussed.

As can be seen from table 4.5 there was a considerable variation in the measured quality factors between the various modes excited for this mass. This range is indicative of the varying degrees to which the suspension loop is affected by the motion excited in the masses' barrels. Additionally, as discussed

Mode	Frequency (Hz)	$Q \times 10^6$
Bar	30587	4.91 ± 0.04
Bar	30588	5.55 ± 0.09
Bending	34850	16.00 ± 0.45
Bending	39948	12.8 ± 0.12
Fundamental Longitudinal	39949	14.10 ± 0.15
Asymmetric Drum	45388	5.45 ± 0.08
Symmetric Drum	46314	3.12 ± 0.02
2nd Asymmetric Drum	56179	7.56 ± 0.11

Table 4.5: *Results of Q measurements of modes of the Silicon [100] mass.*

in Chapter 3, the varying resonant frequencies would be affected to a greater or lesser effect by the suspension length, depending on the violin modes in that length.

In most examined test masses, the highest quality factor measured was for the fundamental longitudinal mode. For this mode, the only motion generated at the mid-point of the mass's length is radial compression and expansion (due to the Poisson's ratio effect). There is no motion along the direction of the mass's central axis, therefore the suspension wire and mass do not rub past each other, promoting friction. It is believed that this radial motion produces considerably less friction, and so less energy loss. The fundamental longitudinal mode therefore has the potential to yield high Q's [77]. Other modes, though, can also excite motion in such a way as to leave the centre line undisturbed.

For the case of the silicon [100], the fundamental longitudinal mode did not provide the highest internal mode Q. This may have been a result of the mode splitting (evidenced by the second mode just below the fundamental) resulting in energy being lost into this mode, thereby reducing the Q of the

fundamental. It is also possible that the optimum suspension was not found for the fundamental mode in the time that was available for testing.

Investigation of other modes, where motion at the centre line is not minimised can provide useful information. A particular instance is the investigation of the behaviour of the faces of the test masses, as each mode distorts these faces in a different way and to a different extent. This is the basis behind work presented in the next chapter, where the effect of applying a dielectric mirror coating to the test masses is investigated.

A second silicon sample, this one cut along the [111] axis was also tested. In this orientation, the mass exhibited anisotropy about the axis, making identification of the modes more complicated. It should be noted though that a similar spread in Q's as measured for the various modes excited, the results ranging from 1.38×10^6 to 1.30×10^7. This maximum value is close to the best recorded for the other silicon sample, suggesting that the differing cuts do not affect the potential intrinsic Q of the material, though this is not certain.

4.5 Conclusions

For a ground-based interferometric gravitational wave detector to be sensitive enough there are certain requirements that must be satisfied by the various components for the detector. In the case of the test mirror materials, that requirement is that it possesses a low internal loss, or high quality factor Q. For GEO 600, the required Q is 5×10^6.

It is already known that fused silica had a high enough quality factor for initial detectors, and the work presented here confirmed this, the best samples giving a Q of 2.39×10^7. Other samples, though, yielded far lower Q's, highlighting the need for care to be taken in the manufacturing of the pieces to maintain

their low losses.

Tests carried out on YAG showed that it had losses considerably lower than fused silica. This was only achievable though when the sample was well polished. The re-polishing carried out more than doubled the measured Q, showing that surface condition is very significant. Other samples, such as GGG and spinel also look like promising alternative detector mirror materials, though it may not be practical to produce large enough samples.

The current front-runner for possible replacement for fused silica in later stage interferometers is sapphire. It has been known for some time that samples grown using the horizontal oriented crystallization growth have Q's in excess of $\times 10^8$. Tests carried out on samples manufactured by the Heat Exchanger Method, a process that should be able to produce samples of sufficient size, have shown that they can match the earlier loss measurements. The sample tested in Glasgow yielded a Q of 2.59×10^8, the highest quality factor measured outside of Russia. Once again, though, not all HEMEX samples performed as well as this, highlighting once again the importance of the condition of a sample when measuring it. That aside, these very high quality factors suggest that this type of sapphire could be used for the test masses in the advanced stages of interferometric gravitational wave detectors. However, its relatively high thermal expansion coefficient means that its attractiveness as a mirror substrate is not as clear-cut since this results in a higher level of noise as a result of thermoelastic effects, which will limit the sensitivity.

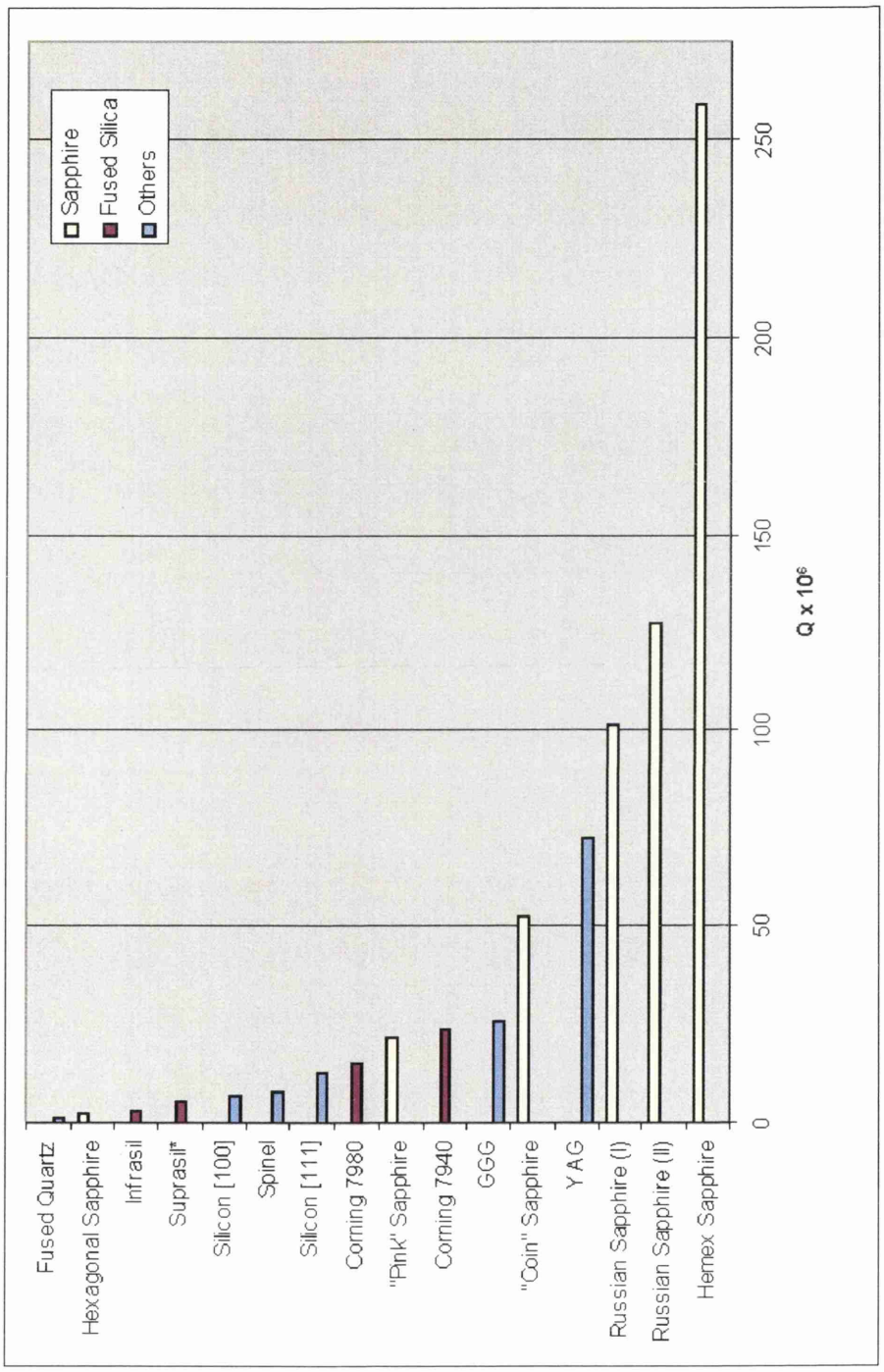

Figure 4.5: *Overview of the results for a range of potential test mass materials.*

Chapter 5

The Effect of Mirror Coatings on the Losses of Test Masses

5.1 Introduction

Interferometric gravitational wave detectors use laser interferometry to sense the position of test masses that have been coated to form mirrors. These masses are suspended as pendulums and are highly isolated from external disturbances. Across part of the frequency range of interest for gravitational wave detection, thermal noise from the test masses and their suspensions forms a limit to achievable detector sensitivity. To minimise the thermal noise resulting from the test masses, substrate materials of low intrinsic loss are desirable. To benefit from the low intrinsic dissipation of the substrates all sources of excess mechanical loss associated with using the substrates as suspended pendulums should be minimised. The multi-layer dielectric coatings that are applied to each substrate to form the mirror coatings are a potential source of excess dissipation, and in this chapter the losses resulting from this are discussed. The work focusses on fused silica, the current material in use for gravitational wave detectors under construction, though some discussion is included on work

carried out on sapphire.

5.2 Experimental Background

All interferometric gravitational wave detectors currently under construction use fused silica as the material for their test mirrors, due to a combination of properties including relatively low mechanical loss, availability in suitable sized pieces and ease of surface polish. For the experiments to determine the coating losses, two samples of fused silica were chosen, one Corning 7940 (grade 3G) and the other Corning 7980 (grade 0C). Both of these were of the same dimensions (diameter 12.5 cm and height 10.2 cm). Figure 5.1 shows one of these in the suspension cradle. Each sample was polished by General Optics Inc. [78], having super-polished faces and inspection polished barrels. The same company applied dielectric coatings to the faces of both cylinders. One face had a mirror coating designed to be highly reflecting at 1064 nm and an anti-reflection coating (at the same wavelength) was applied to the other face. From analysis of the coating it is believed that the high reflective coating on the 7980 mass consists of approximately 43 alternating quarter wavelength layers of aluminium oxide and tantalum pentoxide, with a geometrical thickness of 6.3 μm. For the 7940 mass it is believed there are 59 layers with a geometrical thickness of 8.6 μm.

It is assumed that the loss in the coating is proportional to the total coating thickness and that the loss is homogeneous throughout the coating, thus it is assumed that the anti-reflecting coating (which has only ~ 2 layers) does not add appreciably to the total loss.

The relatively large size of these test masses prevented suspension on silk threads as they could not support the larger mass. (Each mass was 2.88 kg.) Suspensions, therefore, focused on tungsten wires. Initially, 200 μm tungsten

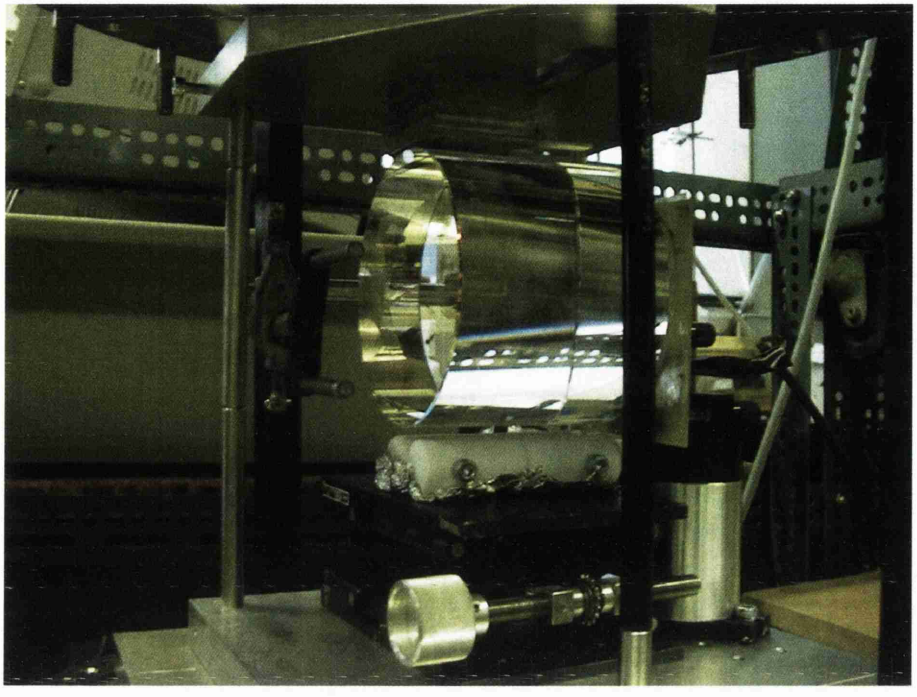

Figure 5.1: *Coated Corning fused silica mass in suspension cradle.*

was used, as the stress in this wire would be less than the breaking stress of the tungsten. The stress was calculated from equation 5.1.

$$Stress = \frac{mg}{n\pi r^2} \tag{5.1}$$

where m is the mass of the sample (2.88 kg), g is gravity, r is the radius of the wire and n is the number of wires, taken as two here. For the 200 μm diameter wire, this gave a stress of 450 MPa, c.f. breaking stress of tungsten of 1920 MPa [79]. This wire was polished in the manner described in Chapter 3. This wire and the surface of the mass at the suspension point were then greased and various lengths of suspension wire tried. Results, though, were considerably poorer than was typical for fused silica. It was therefore decided to use 150 μm tungsten instead, and the results improved noticeably. (Stress in 150 μm wire was 800 MPa.) It should be noted that the tested samples were suspended multiple times ($\sim$ 30 separate suspensions in each case), the lengths

of the suspension wires varied each time. This was in accordance with previous work [57, 59] detailed in Chapter 3 regarding the effect of violin resonances in the suspension wires when they were of certain lengths. The losses quoted in table 5.1 are the lowest measured for each resonant mode, though these did not generally occur in the same suspension.

5.3 Results

Mode	Frequency (Hz)	Coated 7980 Measured Loss $\times 10^{-7}$	Coated 7940 Measured Loss $\times 10^{-7}$	Uncoated 7980 Measured Loss $\times 10^{-7}$
Bending (8, n=1)	22105	1.37 ± 0.04	1.60 ± 0.01	0.95 ± 0.05
Asymmetric Drum (1, n=0)	22977	1.16 ± 0.02	1.23 ± 0.05	1.00 ± 0.03
Fundamental (1, n=2)	25378	0.65 ± 0.01	0.50 ± 0.02	0.89 ± 0.02
Butterfly (16, n=2)	26176	1.61 ± 0.03	1.89 ± 0.04	0.95 ± 0.05
Symmetric Drum (4, n=0)	28388	3.10 ± 0.12	3.60 ± 0.29	0.95 ± 0.01
Expansion	31710	1.09 ± 0.01	1.01 ± 0.01	0.94 ± 0.04
2nd Asym Drum (3, n=0)	36045	0.86 ± 0.01	0.94 ± 0.03	0.87 ± 0.02

Table 5.1: *Losses of various modes measured for coated and uncoated fused silica test samples.*

It can be seen from table 5.1[1] that there is a considerable variation in the level

[1]The frequencies quoted are for the coated Corning 7980 sample. The frequencies for the

of measured loss factor between the modes[2], some modes showing a loss factor as much as four times higher than others. It was postulated that this variation was due to losses associated with the coatings. Experiments carried out on an uncoated sample of Corning 7980 of the same dimensions showed a much lower variation from mode to mode. These results are also presented in table 5.1. Here the variation from mode to mode was at most 10 percent. From this the assumption was made that the substantial variation in Q measurements seen from the modes of the coated samples was predominantly due to the effects of the dielectric coating and that suspension losses are insignificant since all the masses were measured using the same experimental set-up. It should be noted, though, that the best loss factor measured was not as low as the best losses measured for the coated masses .

For each of the coated masses a small amount of coating spilled over on to the barrel of the mass. The effect this had is discussed later.

5.4 Analysis

Assuming that all other losses have been reduced to a negligible level, the total measured loss may be expressed as

$$\phi(\omega_0)_{\text{coated mass}} = \phi(\omega_0)_{\text{sub}} + \phi(\omega_0)_{\text{coating}} \tag{5.2}$$

where $\phi(\omega_0)_{\text{sub}}$ is the intrinsic loss of the substrate material and $\phi(\omega_0)_{\text{coating}}$ is any loss associated with having the mass coated.

Equation 5.2 can be generalised for the case of coating on both the face and

other two masses were essentially the same.

[2]Numbering denotes the symmetry classification of the modes following G. McMahon [80]

the barrel to

$$\phi(\omega_0)_{\text{coated mass}} = \frac{E_{\text{sub}}}{E_{\text{total}}}\phi(\omega_0)_{\text{sub}} + \frac{E_{\text{face coating}}}{E_{\text{total}}}\phi(\omega_0)_{\text{face coating}} + \frac{E_{\text{barrel coating}}}{E_{\text{total}}}\phi(\omega_0)_{\text{eff}} \tag{5.3}$$

Now, assuming that $E_{\text{face coating}} \ll E_{\text{sub}}$ and $E_{\text{barrel coating}} \ll E_{\text{sub}}$, this becomes

$$\phi(\omega_0)_{\text{coated mass}} \approx \phi(\omega_0)_{\text{sub}} + \frac{E_{\text{face coating}}}{E_{\text{sub}}}\phi(\omega_0)_{\text{face coating}} + \frac{E_{\text{barrel coating}}}{E_{\text{sub}}}\phi(\omega_0)_{\text{eff}} \tag{5.4}$$

$\frac{E_{\text{face coating}}}{E_{\text{sub}}}$ is the fraction of the energy of the mode stored in the coating compared with the substrate and $\frac{E_{\text{barrel coating}}}{E_{\text{sub}}}$ is the fraction of the energy of the mode stored in the barrel compared with the substrate. (A discussion of how this energy comes about is presented in Appendix D.) $\phi(\omega_0)_{\text{eff}}$ represents the effective loss due to the coating material on the barrel of the sample. It is assumed here that the distribution of the coating on the barrel is essentially even and of the same thickness as the coating on the faces.

In order to determine values for the energy ratios in equation 5.4 a finite element analysis package from Algor [81] was used to model the displacement of the test masses for each of the studied modes. These modes are shown in Appendix C. By using the maximum displacements, and therefore maximum strain values, the values for the relevant energy ratios for the faces and barrels for each of the modes could be calculated. For these calculations, it was assumed that the coating followed the contours of the fused silica mass. Additionally, in calculating the energy associated with the coating layers, an equivalent value for the Young's modulus and Poisson's ratio for the coating was used, determined using the technique described in [82]. These values, and those for the fused silica substrate are given in table 5.2.

Material	Young's modulus	Poisson's Ratio
Aluminium oxide	3.6×10^{11} [83]	0.27 [84]
Tantalum pentoxide	1.4×10^{11} [82]	0.23 [82]
Calculated multilayer [82]	2.6×10^{11}	0.26
Fused silica	7.2×10^{10} [84]	0.17 [84]

Table 5.2: *Material properties for coatings and subtrate.*

Great care was taken in carrying out the ratio calculations as results for the ratio values depended on the refinement used in the FE analysis model. The modeling work was carried out by D. Crooks and details of the models used are discussed fully in Crooks, Sneddon et al [85].

5.4.1 Regression Analysis

To determine the values for the energy ratios initially, it was assumed that $\phi_{\text{eff}} = 0$ in equation 5.4. (i.e. the mechanical losses associated with the coating on the sample's barrel were of a negligible level.) This allowed for an examination of the variation of ϕ_{coated} against front surface energy for both 7940 and 7980 masses. Using this technique, though, a linear fit for ϕ_{coated} against front face energy could only be found if the asymmetric drum mode results were ignored. However, for this mode, confidence in the measured result was high since it is unlikely that experimental measurements will result in losses that are significantly too low. It was therefore clear that this simple approach was not going to be accurate, and so ϕ_{eff} had to be included in the calculations. A multivariable linear regression algorithm for the parameters ϕ_{sub}, $\phi_{\text{face coating}}$ and ϕ_{eff} was therefore adopted.

Provided that the symmetric drum mode results were ignored, there was a good linear fit for both masses, giving the results in table 5.3. The measured losses for this mode were noticeably higher than that predicted by the linear

For the Corning 7940 mass:	$\phi(\omega_0)_{\text{substrate}}$	$= (3.7 \pm 0.5) \times 10^{-8}$
	$\phi(\omega_0)_{\text{coating}}$	$= (6.4 \pm 0.6) \times 10^{-5}$
	$\phi(\omega_0)_{\text{eff}}$	$= (6.9 \pm 0.4) \times 10^{-5}$
For the Corning 7980 mass:	$\phi(\omega_0)_{\text{substrate}}$	$= (5.6 \pm 0.9) \times 10^{-8}$
	$\phi(\omega_0)_{\text{coating}}$	$= (6.3 \pm 1.6) \times 10^{-5}$
	$\phi(\omega_0)_{\text{eff}}$	$= (6.3 \pm 0.9) \times 10^{-5}$

Table 5.3: *Values of bulk, coating and barrel losses for the Corning 7940 and 7980 masses.*

fit in each mass, therefore it must have been a real effect. It was not possible to determine the reason behind this. It has been assumed that there is some unmodelled loss associated with the shape of this mode, perhaps due to edge effects at the chamfers between the coated mirror faces and the barrels.

It should be noted that both the theoretical values for the uncoated loss (3.7×10^{-8} and 5.6×10^{-8}) are lower than the lowest loss measured for the uncoated fused silica mass (8.7×10^{-8}). So, the calculated values are of the same order as the measured results. The fact that they are lower than the measured result agrees with what would be expected from a theoretical prediction.

5.5 Consequences for future detectors

As discussed in Chapter 2, until relatively recently the method of predicting the thermal noise in the test masses of gravitational wave detectors, at frequencies well below the first internal resonant modes of the mirrors, involved a normal mode expansion of the acoustic modes of the mirrors. The expected thermal noise was calculated by adding incoherently, with suitable weighting factors, the noise in the tails of the resonances of the test masses. Alternative approaches to the problem have been developed by Levin [51], Liu and

Thorne [52], Nakagawa et al [86] and Bondu et al [87], and Levin has pointed out that in the cases where the spatial distribution of the loss in the mirror is non-uniform, using a modal expansion approach may lead to an incorrect estimation of the thermal noise.

Nakagawa et al [86] have developed a formalism where the fluctuation-dissipation theorem can be expressed in terms of the static Green's function to calculate the distribution of the thermal motion on the front face of a semi-infinite mirror. This work has been extended to allow estimation of the effect of having a coating layer of finite thickness and different material properties on the front face of the mass. It is calculated [88] that the spectral density of the thermal noise, $S_\phi^{\text{coated}}(f)$, is increased over that of the uncoated mass, $S_\phi^{\text{substrate}}(f)$, by the factor shown in equation 5.5.

$$\frac{S_\phi^{\text{coated}}(f)}{S_\phi^{\text{substrate}}(f)} = 1 + \frac{2}{\sqrt{\pi}} \frac{(1-2\sigma)}{(1-\sigma)} \frac{\phi_{\text{coating}}}{\phi_{\text{substrate}}} \left(\frac{d}{w}\right) \tag{5.5}$$

where d is the coating thickness, w is the radius of the laser beam interrogating the test mass and σ represents the Poisson's Ratio of the substrate material of Young's Modulus, Y. This assumes that the substrate and the coating have the same mechanical properties but different loss factors. If it is allowed that σ and Y for the coating and substrate are not the same, then the ratio in equation 5.5 becomes

$$\frac{S_\phi^{\text{coated}}(f)}{S_\phi^{\text{substrate}}(f)} = 1 + \left\{ \frac{1}{\sqrt{\pi}} \frac{(1+\sigma_{\text{coating}})}{(1-\sigma^2{}_{\text{substrate}})(1-\sigma_{\text{coating}})} \frac{\phi_{\text{coating}}}{\phi_{\text{substrate}}} \frac{Y_{\text{substrate}}}{Y_{\text{coating}}} \right\} \times$$

$$\left\{ \left[(1-2\sigma_{\text{coating}}) + (1-2\sigma_{\text{substrate}})^2 \frac{(1+\sigma_{\text{substrate}})^2}{(1+\sigma_{\text{coating}})^2} \left(\frac{Y_{\text{coating}}}{Y_{\text{substrate}}}\right)^2 \right] \left(\frac{d}{w}\right) \right\} \tag{5.6}$$

To calculate a value for the increase in predicted power spectral density the

following values can be substituted into equation 5.6: from table 5.2 the calculated values for the moduli of elasticity and Poisson's ratios for the coating material, $Y_{\text{coating}} = 2.6 \times 10^{11}$ and $\sigma_{\text{coating}} = 0.26$, and the values for the substrate, $Y_{\text{substrate}} = 7.2 \times 10^{10}$ and $\sigma_{\text{substrate}} = 0.17$; from table 5.3 the average values for ϕ_{coating} and $\phi_{\text{substrate}}$, 6.4×10^{-5} and 4.7×10^{-8} respectively; a laser beam whose spot has a radius of 5.5×10^{-2} m on the coating surface [89] where the coating has a thickness of 7.5×10^{-6}.

Making the above substitutions gives the result that the predicted power spectral density of the thermal noise is found to be increased by a factor $(1 + 0.27)$. This means that the amplitude spectral density of the noise is increased by 1.13 over that which would be predicted without evaluating the effect of the mechanical loss of the coating. It should be noted that it has been assumed that the losses in the coating and the substrate are structural in nature, i.e. they have the same value at low frequency as they have at the resonant mode frequencies where they were measured. This seems reasonable as calculations [90] suggest that thermoelastic damping, which is often non-structural in nature, is at a lower level than the losses we have measured.

5.6 On to sapphire

To investigate the effects of applying a dielectric mirror coating to a sapphire substrate, a small sample of diameter 8 cm and height 3 cm was tested. This time, it was possible to test the sample before and after coating, allowing for a direct comparison of the losses in both conditions. The mass was a Crystal Systems HEMEX sample. The coating was applied by REO [91]. It was designed to be high reflecting at 1064 nm and was made up of 30 $\lambda/4$ layers of silicon dioxide and tantalum pentoxide. The uncoated mass is shown between crossed-polarisers in figure 5.2, and the results of the before and after testing

are in table 5.4.

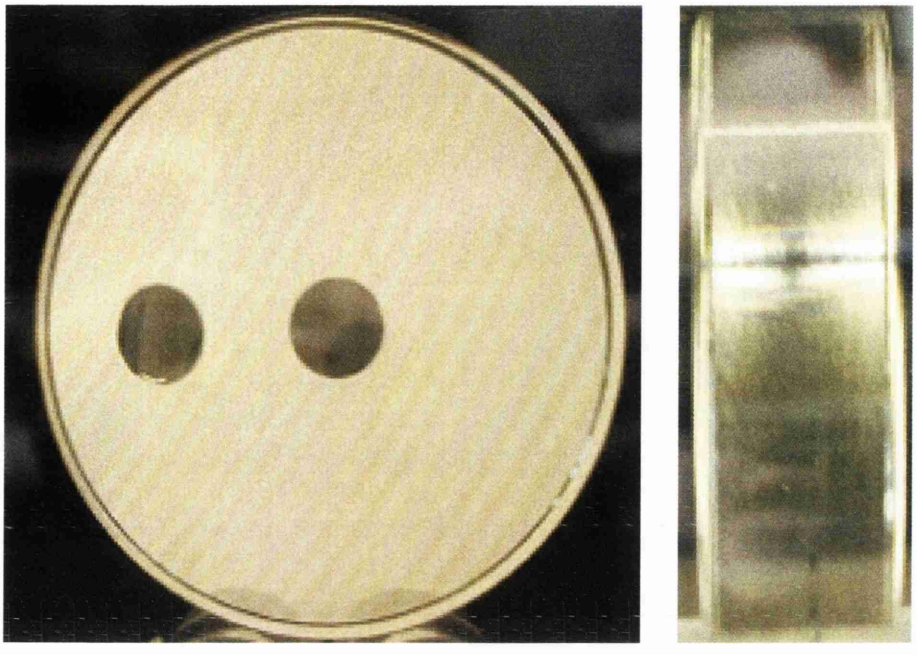

Figure 5.2: *Picture of the "Coin" sapphire sample showing front and side views. The photograph was taken through cross polarisers.*

Mode	Frequency (Hz)	Uncoated measured loss $\times 10^{-8}$	Coated measured loss $\times 10^{-8}$
Clover 4	35679	3.47 ± 0.08	8.33 ± 0.07
Asymmetric Drum	54855	4.52 ± 0.08	15.02 ± 0.22
Bar	68629	11.14 ± 0.20	13.81 ± 0.44
Fundamental longitudinal	82987	1.91 ± 0.04	6.41 ± 0.08
Clover 6	87275	3.65 ± 0.11	9.43 ± 0.18

Table 5.4: *Losses of various modes measured for sapphire sample before and after mirror coating.*

Full analysis of this mass has not been completed due to complications in this case as a result of the mass being cut along the anisotropic m-axis. However, it is useful to examine the case for the asymmetric drum mode analytically.

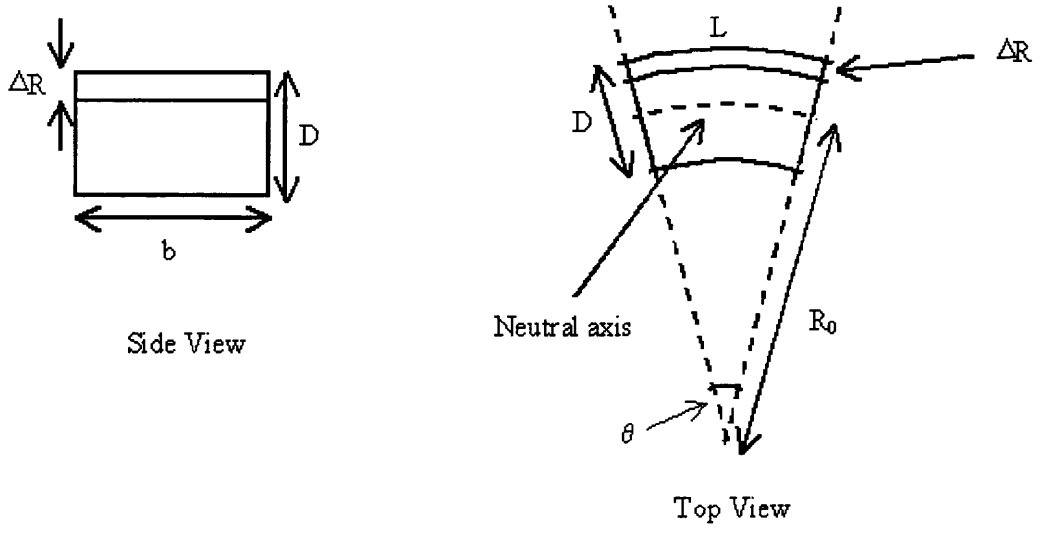

Figure 5.3: *Schematic of a bent bar.*

Simple Case - A Bar

First consider the case of a bar of length L, height D and width b. Assume one of the faces of the bar has a coating applied to it, of thickness ΔR. As the bar flexes, the coating is stretched. The amount of energy stored as the coating is stretched by a length ΔL can be expressed as

$$E = \frac{1}{2}k(\Delta L)^2 = \frac{1}{2}\frac{Y_c \Delta R b}{L}(\Delta L)^2 \tag{5.7}$$

where $k = Y_c A/L$ is the spring constant, Y_c is the Young's modulus of the coating and $A = \Delta R b$ is the cross-sectional area over which the force F is applied. To evaluate ΔL, recall that $L = R_0\theta$ and $L + \Delta L = (R_0 + D/2)\theta$. Hence,

$$\Delta L = (R_0 + D/2)\theta - R_0\theta = \frac{D}{2}\theta \tag{5.8}$$

So,

$$E_{\text{coating}} = \frac{Y_c \Delta R b D^2 \theta^2}{8L} \tag{5.9}$$

In order to compare this with the energy stored in the whole bar, first consider the energy stored in a thin section, dE of the bar, then integrate over the whole bar. The thin bar section has thickness dr at a distance r from the origin.

For the small element, $dE = \frac{1}{2}k(\Delta L)^2$. Here $k = Y_b A/L = Y_b b dr/L$, where Y_b is the bar's Young's modulus, and the cross-sectional area, $A = bdr$. Also, $L = R_0\theta$ and $L + \Delta L = r\theta$. Therefore, $\Delta L = (r - R_0)\theta$. So, the energy stored in stretching a section of the bar is

$$dE = \frac{1}{2}\frac{Y_b b dr}{L}(r - R_0)^2\theta^2 \tag{5.10}$$

To get the total energy in the bar, this expression is integrated over the height. First note that we have calculated the energy stored in stretching an element of the bar above the neutral axis. Below this axis, the bar is compressed. It is assumed that an equal amount of energy is stored in compressing an element compared with stretching it. Therefore, the integration will be performed for the region above the neutral axis to get the total energy stored in stretching, then double it to get the total energy in the bar. So, from equation 5.10,

$$\begin{aligned}
\frac{E}{2} &= \frac{Y_b b\theta^2}{2L}\int_{R_0}^{R_0+D/2}(r - R_0)^2 dr \\
&= \frac{Y_b b\theta^2}{2L}\frac{1}{3}\left(\frac{D}{2}\right)^3 \\
&= \frac{Y_b b\theta^2 D^3}{48L}
\end{aligned} \tag{5.11}$$

Hence,

$$E = \frac{Y_b b \theta^2 D^3}{24L} \tag{5.12}$$

So the ratio of the energy stored in the coating in comparison to that stored in the bulk is then:

$$\frac{E_{\text{coating}}}{E_{\text{bulk}}} = 3\frac{Y_c}{Y_b}\frac{\Delta R}{D} \tag{5.13}$$

Case for Cylinder

The analysis in the previous section is now extended to the case for the ratio of energy stored in a coating to that stored in the bulk of a cylindrical mass for the case of a mass excited in its asymmetric drum mode.

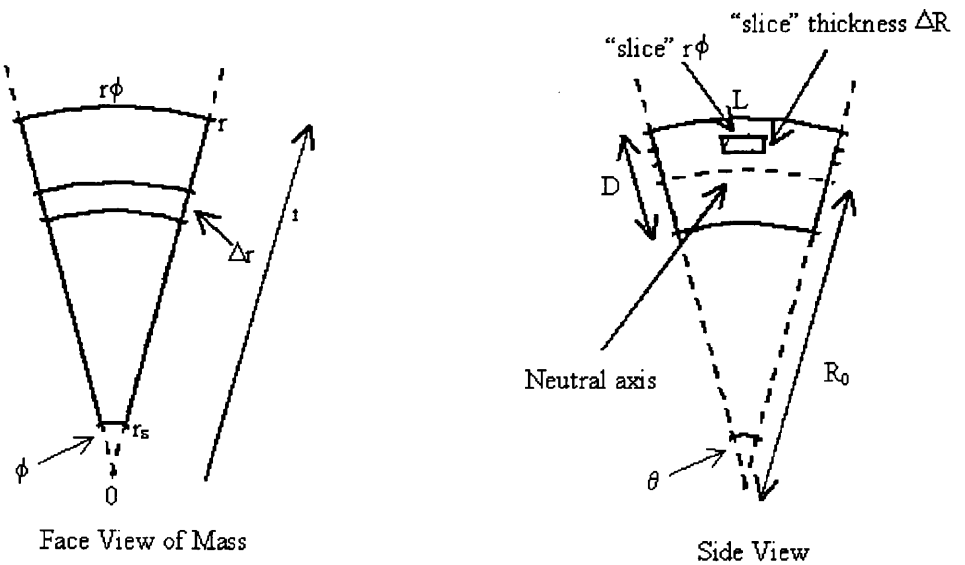

Figure 5.4: *Schematic of a mass distorted into its asymmetric drum mode.*

Consider the cylinder to be divided into a large number of very thin "pie" shaped slices that go almost, but not quite, to the centre of the mass. (Refer to figure 5.4.) The first step is to calculate the energy associated with the stretching of a "pie" segment of the mass (above the neutral axis).

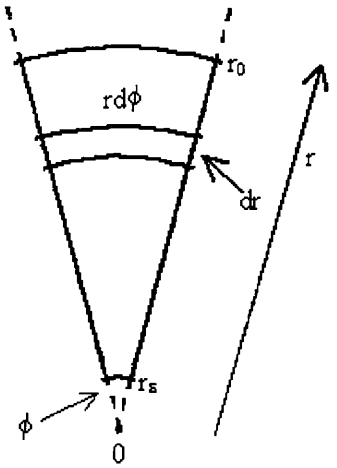

Figure 5.5: *Close up of "pie" segment.*

Let each "pie" be divided into a large number of segments, each of thickness dr. Let the "pie" itself be of thickness ΔR. (See figure 5.5.) Recall again that $dE = \frac{1}{2}k(\Delta x)^2$ with $k = Y_b A/L$. Here $A = rd\phi\Delta R$ and $L = dr$. So, each segment has an individual spring constant, k_n, given by:

$$k_n = \frac{Y_b r d\phi \Delta R}{dr} \tag{5.14}$$

To get the overall spring constant for the pie it is necessary to add the spring constants of the individual segments. These add as shown in equation 5.15

$$\frac{1}{k_{\text{total}}} = \frac{1}{k_1} + \frac{1}{k_2} + \frac{1}{k_3} + ... \tag{5.15}$$

So we add the inverse of k, known as the compliance, C. i.e.

$$C_n = \frac{1}{k_n} = \frac{dr}{Y_b r d\phi \Delta R} \tag{5.16}$$

So the total compliance, C, is:

$$C = \frac{1}{Y_b d\phi \Delta R} \int_{r_\varepsilon}^{r_0} \frac{1}{r} dr$$

$$= \frac{1}{Y_b d\phi \Delta R} log\left(\frac{r_0}{r_\varepsilon}\right) \tag{5.17}$$

Hence,

$$dE = \frac{1}{2} Y_b d\phi \Delta R \left[log\left(\frac{r_0}{r_\varepsilon}\right)\right]^{-1} (\Delta x)^2 \tag{5.18}$$

Here, $L = R_0\theta$ and $L + \Delta x = R\theta$, therefore $\Delta x = (R - R_0)\theta$. Therefore,

$$dE = \frac{1}{2} Y_b d\phi \Delta R \left[log\left(\frac{r_0}{r_\varepsilon}\right)\right]^{-1} (R - R_0)^2\theta^2 \tag{5.19}$$

Now, to find the energy stored in stretching a pie shaped slice of the mass, equation 5.19 is integrated over the thickness of the mass. So,

$$dE_{\text{slice}} = \int_{R_0}^{R_0+D/2} dE = \frac{1}{2} Y_b d\phi \Delta R \left[log\left(\frac{r_0}{r_\varepsilon}\right)\right]^{-1} \theta^2 \int_{R_0}^{R_0+D/2} (R - R_0)^2 dR$$

$$= \frac{1}{48} Y_b d\phi D^3 \left[log\left(\frac{r_0}{r_\varepsilon}\right)\right]^{-1} \theta^2 \tag{5.20}$$

Finally, to get the energy stored in the mass due to stretching, the above expression is integrated over ϕ from 0 to 2π, which is equivalent to multiplying equation 5.20 by 2π. To then take the compressional energy into account, the result is multiplied by 2. So, the total energy stored in the bulk of the mass is:

$$E_{\text{bulk}} = \frac{\pi}{12} Y_b D^3 \left[log\left(\frac{r_0}{r_\varepsilon}\right)\right]^{-1} \phi^2 \tag{5.21}$$

To calculate the energy stored in the coating, consider the pie slice to now be on the surface of the mass. Then, the energy stored in stretching the pie is $dE = \frac{1}{2}k(\Delta x)^2$, where $\Delta x = (R_0 - D/2)\theta - R_0\theta = (D/2)\theta$. Hence, from equation 5.18,

$$dE = \frac{1}{2}Y_c d\phi \Delta R \left[log\left(\frac{r_0}{r_\epsilon}\right)\right]^{-1} \frac{D^2}{4}\theta^2 \tag{5.22}$$

where Y_c is the Young's modulus of the coating material. To get the energy stored in stretching a layer of thickness ΔR on the front of the mass, equation 5.22 is integrated over ϕ. This results in

$$E_{\text{stored in coating}} = \frac{\pi}{4}Y_c \Delta R D^2 \theta^2 \left[log\left(\frac{r_0}{r_\epsilon}\right)\right]^{-1} \tag{5.23}$$

Then the ratio of energy stored in coating to that in the bulk is given by equation 5.24, which is equivalent to the ratio derived for the case of the bar (equation 5.13).

$$\frac{E_{\text{coating}}}{E_{\text{bulk}}} = 3\frac{Y_c}{Y_b}\frac{\Delta R}{D} \tag{5.24}$$

Assuming a Young's modulus for the coating and bulk as 1.05×10^{11} and 3.4×10^{11} respectively, a mass thickness of 2.5 cm and a coating thickness of 6 μm results in a ratio of 2.22×10^{-4}. This value can then be substituted into a rearrangement of equation 5.4 (generalised for the case where the losses due to barrel coating as negligible). Using the loss values for the asymmetric drum mode in table 5.4, the coating loss can be estimated:

$$\begin{aligned}
\phi_{\text{coating}} &= \frac{\phi_{\text{total}} - \phi_{\text{bulk}}}{E_{\text{coating}}/E_{\text{bulk}}} \\
&= \frac{10.5 \times 10^{-8}}{2.22 \times 10^{-4}} \\
\phi_{\text{coating}} &= 4.73 \times 10^{-4} \qquad (5.25)
\end{aligned}$$

Preliminary calculations [92] for this mass have so far estimated the ratio of the energy stored in the coating to that in the bulk as 1.41×10^{-4}, which results in a coating loss of 7.45×10^{-4}. This is of the same order as the analytical result. Both methods of calculation, though, assume that the sapphire mass is isotropic, which it is not. Further work is therefore required before the specific loss can be estimated.

5.7 Conclusions

Experiments suggest that the effect of argon-sputtered dielectric coatings on the level of thermal noise associated with silica test masses in advanced interferometric gravitational wave detectors will be significant. Preliminary experiments on sapphire suggest a similar damping effect by the coating. Initial analytical calculation of the coating loss suggests that the loss is roughly 8 times higher than that for fused silica. There is clear need, though, for a series of experiments to be carried out, in which coating parameters are systematically varied as this will allow the source of the coating losses to be investigated.

Chapter 6

The Effect of Bonding on the Losses of Test Masses

6.1 Introduction

As was discussed earlier in Chapters 2 and 3, the thermal noise associated with the test masses in a interferometric gravitational wave detector can be increased due to frictional effects between test masses and their suspension fibres or wires. In the laboratory, this friction can be overcome to an extent by techniques such as polishing of suspension wires and lubrication of wire and test mass surface at the line of contact. For actual gravitational wave detectors, though, this is not sufficient. Low loss jointing techniques are therefore required. It has been shown previously that the process of hydroxide-catalysis bonding does not have a significant detrimental effect on the measured quality factors [57], and therefore the losses, of a test mass. This technique, therefore, has been chosen to attach fused silica "ears" to the test masses, to which fused silica suspension fibres are then welded. In this instance, the bonding is between two samples of fused silica. It was not known, though, whether the same effect would hold for bonding between two different materials, such

as bonding between fused silica and sapphire. This could be of importance as sapphire is a possible contender for the test masses in future gravitational wave detectors. Work to determine the effect of such "cross-bonding" is presented here. Additionally, a different type of bonding - sodium silicate bonding - was tried and how it effects the losses of a suspended mass investigated.

6.2 Hydroxide-catalysis Bonding

The jointing technique called hydroxide-catalysis bonding was developed by D.-H. Gwo at Stanford University for assembling the fused quartz star-tracking telescope of the Gravity Probe-B Relativity Mission [93]. This application required a jointing that was very strong, mechanically, as well as being relatively insensitive to temperature changes. Experiments have shown that hydroxide-catalysis bonding satisfies these requirements [94]. For the process to be applicable to the construction of low loss suspensions, it is also necessary for the joints formed to have very low mechanical loss. It is also necessary that the materials to be bonded have OH^- on the surface and the ability to form metallic salt (e.g. silicate, aluminate). (The chemical model of the bonding is discussed below.)

The typical processes and techniques involved in this type of bonding will now be discussed for bonding two pieces of fused silica. The surfaces of pieces of fused silica to be joined should ideally be of optical flatness of approximately $\lambda/10$, and free of all particulate and chemical contamination. A volume of an aqueous solution of potassium hydroxide (1:500 molecular number ratio of $KOH:H_2O$) appropriate to the surface area to be bonded (of the order of $0.4\mu l/cm^2$) is introduced between the fused silica surfaces and the surfaces then brought together.

How the bonding process works, chemically, is discussed here and detailed in

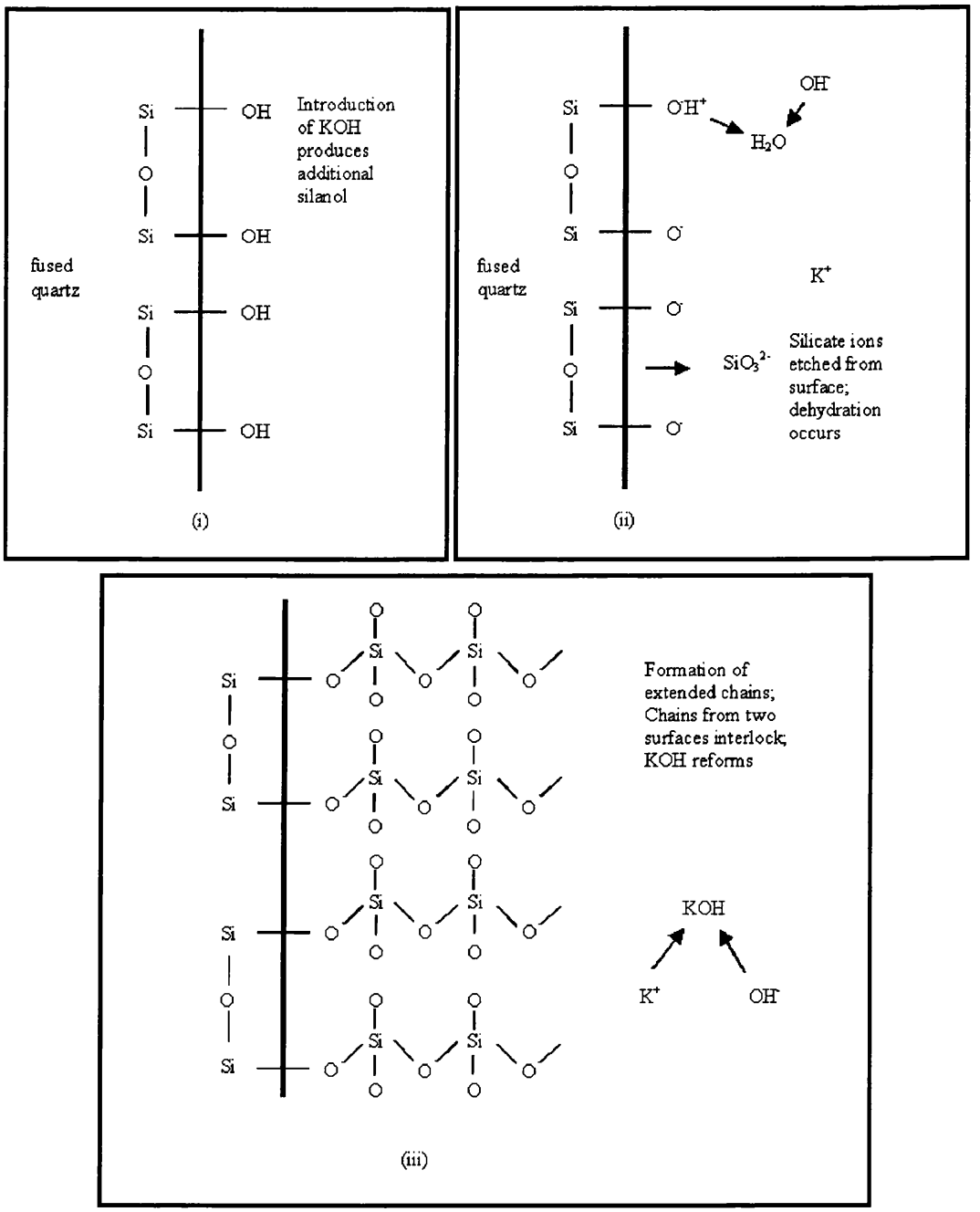

Figure 6.1: *Model of the chemistry involved in hydroxide catalysis bonding.*

figure 6.1. A number of siloxane bridges (Si-O-Si) are exposed on the polished surfaces of the fused silica. Water in the atmosphere causes the formation of a small number of silanol groups (Si-OH) from these siloxane bridges. In-

troducing the KOH solution to these bonding surfaces causes hydration, and increases the number of silanol groups present, forming 2 per exposed siloxane bridge. (See figure 6.1(i).) The KOH also reacts with the surface of the fused silica (SiO_2). The simplest form this reaction can take is

$$SiO_2 + 2KOH \rightarrow K_2SiO_3 + H_2O$$

i.e. the KOH etches the SiO_3^{2-} ions from the bonding surface, depositing them into the solution along with the K^+ ions. The KOH also strips the H^+ ion from each of the silanol groups. These then bond with the hydroxide ions (OH^-) present in the solution to form H_2O - i.e. dehydration occurs (see figure 6.1(ii)). A silicate ion is then attracted to the O^- remainder of each silanol group. Further silicate ions then bond to the free O^- present on each subsequent silicate ion to form an extended silicate chain. The K^+ ion is not involved in the bond formation and the potassium hydroxide is therefore returned to the solution at the end of the reaction (6.1(iii)). A similar process occurs on the other bonding surface when it is brought into contact with the first, KOH-coated surface. The activated pieces are then brought into contact and a complicated interlocking structure is formed.

Readjustments of the pieces being jointed are possible within roughly 30 to 40 minutes of the start of the jointing process. The maximum bond strength is achieved after several weeks, with the exact time depending on the concentration of the KOH solution and any mismatch of the surface figures of the bonded pieces; however after only a few hours the bond has sufficient strength to allow the fused silica pieces to be handled in regular environments.

The same chemical model holds for a process called sodium silicate bonding. Here, a sodium silicate solution replaces the KOH solution as the trigger for the bonding. The ratio of the sodium silicate to water is 1:6, the sodium silicate

itself consisting of 14 percent NaOH, 27 percent SiO_2 and 51 percent H_2O. Experiments to determine whether this technique would have no detrimental effects on the quality factors of a bonded mass are presented later in this chapter.

6.3 Sapphire to Fused Silica Bonding

One of the front running materials that may replace fused silica as the test mirror substrates is sapphire (Al_2O_3). It has been shown that the internal losses associated with this material are considerably better than those for fused silica. It has also already been shown that fused silica masses could be suspended in a low loss way from fused silica fibres, welded to fused silica ears that are bonded to the mass. To see if this was also true for bonding a fused silica ear to a sapphire mass, work on a known sapphire sample was carried out. The sample chosen was that which had yielded the very high quality factor of 2.59×10^8. After the initial testing had been completed, it was sent to General Optics [78] to have a flat polished along its length. (This flat was 1 cm wide, and the surface was polished to $\lambda/10$.) When the mass returned, it was tested again, much as it had been before, using a range of wire and thread suspensions. The best Q measured this time was only 1.91×10^8. This was down from the original mass, but still very high. It was therefore concluded that the polishing work performed on the mass had not significantly damaged the mass, and so work could continue.

A fused silica post, of circular cross-section, was bonded using the hydroxide-catalysis technique described above with a sodium silicate solution. The same chemical reaction was triggered in the sapphire as in the fused silica through the presence of O_3^- in the sapphire. The post was bonded to the middle of the flat of the mass and left to cure for a month. Once again, the quality factor

Test Mass Condition	Suspension	Lubrication	Frequency (Hz)	Pressure (mbars)	Q $\times 10^7$
Original Cylinder	Tungsten (50μm)	On mass	53591	5×10^{-6}	25.9 ± 0.5
With flat	Tungsten (50μm)	On both	53596	1×10^{-5}	19.10 ± 0.53
With post (before welding)	Fused silica	N/A	53597	2×10^{-5}	2.76 ± 0.03
With post (after welding)	Fused silica	N/A	53598	4×10^{-5}	0.824 ± 0.002

Table 6.1: *Results of Q measurements of the fundamental longitudinal mode at the various stages for the bonded sapphire test mass.*

of the mass was then tested. The plan was to construct a monolithic fused silica suspension, but to begin with the mass was again suspended on thread. The best Q result measured at first was only 1.7×10^7. It was thought that this might be a result of limitations in the suspension system - because of the post atop the mass, which was roughly 2 cm in height, there was a limit on how close the mass could get to the clamp, and so a limit on how short the suspension loop could be made. A new clamp was therefore needed. Taking the original clamp block as detailed in figure 3.6, a new bar was fashioned. This had a recessed arch cut into it, allowing the post to sit within the clamp bar, and also bring the clamp point closer to the mass. Figure 6.2 shows this new clamp and how the mass sat within it.

Initial testing with this new clamp yielded lower Q's than those already found. Upon inspection of the clamp, it was found that instead of clamping the loop at the bottom (indicated by the blue dots on figure 6.2) it was clamping further up, within the clamp (green dots). The clamp was filed in the region of the

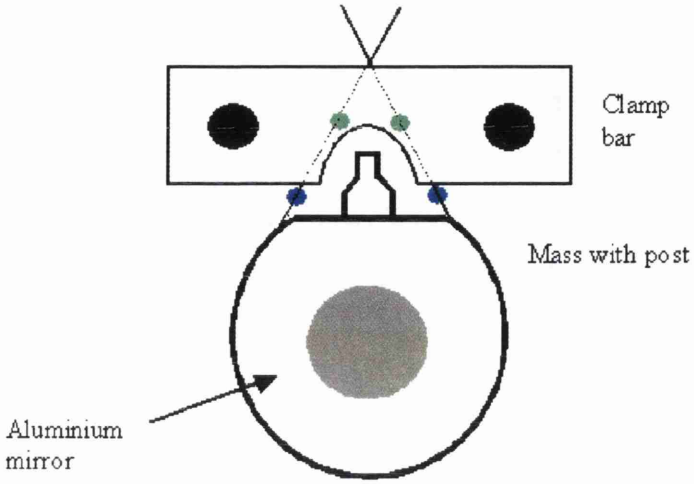

Figure 6.2: *The revised clamp with recessed arch for the bonded post.*

green dots and then testing resumed. Instantly, the Q improved, eventually peaking at 2.76×10^7. Whilst the testing was carried out, it was observed that there was some increase in the measured Q over time. Three suspensions were allowed to hang for roughly a day within the vacuum tank. Figure 6.3 shows how the quality factor developed. The largest change exhibited was a $\sim$ 25 percent improvement.The level of change varied from suspension to suspension, indicating a dependence on the quality of the suspension. The change was thought to be due to the mass settling into the silk loop.

Since it was apparent that the mass was not going to yield Q's of the order of $\times 10^8$ on normal loops, it was decided to attempt a fused silica suspension. The first suspension is detailed schematically in figure 6.4, whilst figure 6.5 shows the suspended mass. To the top of the fused silica post, a short piece of fused silica rod (diameter 3 mm) was welded using a hydrogen torch. To the tapered ends of this rod, which formed the top of a "T" piece, two fused silica fibres were welded. These fibres were pulled from 1 mm rod by hand, again using the hydrogen torch. The other ends of the fibres were then welded to a fused silica slide, which in turn was clamped within the recessed clamp. The

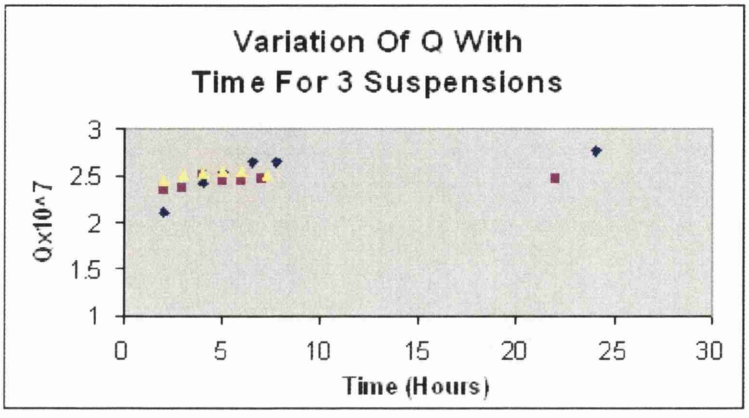

Figure 6.3: *The time-variation of measured Q for three suspensions of the bonded sapphire mass.*

fibres were angled outward to minimise the rotation of the mass once it was hanging.

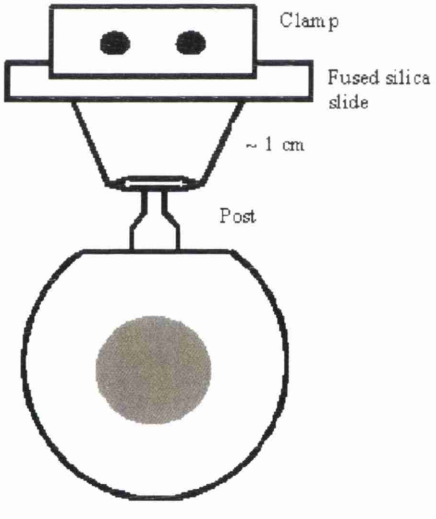

Figure 6.4: *Schematic of the fused silica suspension.*

When the mass was then tested again, the Q was found to be 1.83×10^6. It had again shown some variation with time, which could not be attributed to the same cause as before since the mass could not "bed in" to the suspension. The variation was thought this time to be temperature dependent and so a heat

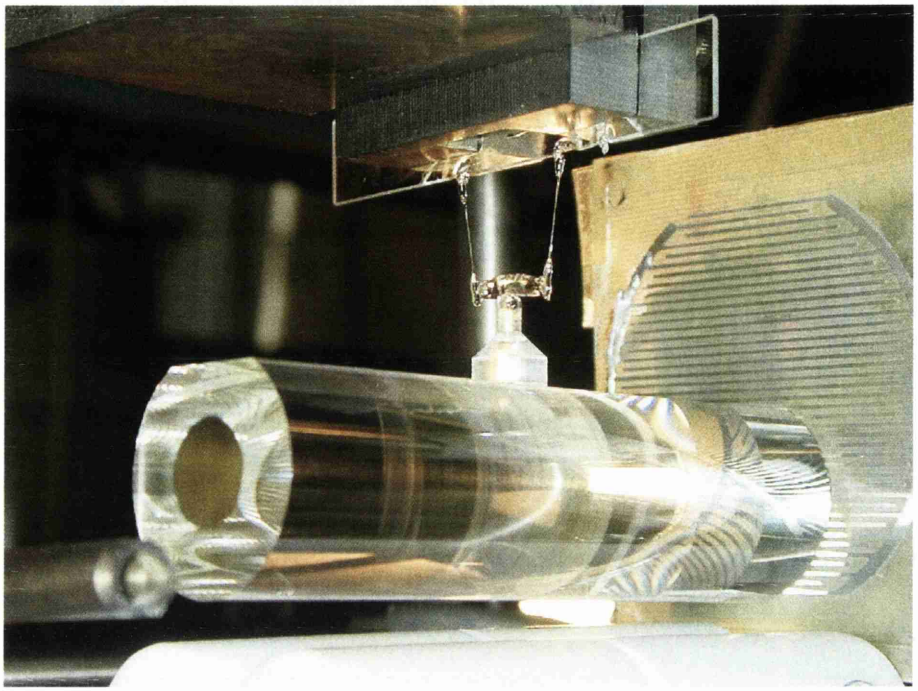

Figure 6.5: *Photograph of the bonded sapphire sample, suspended from a fused silica suspension.*

lamp was placed next to one of the vacuum tank's port holes. Initially, this had the effect of lowering the Q, but after more heating it increased to 2.10×10^6. Over subsequent suspensions, the thin fused silica slide was replaced by a thicker block and the fibres cut from longer ones pulled using the fibre-puller detailed in Appendix E. Different lengths were also tried, as were different angles, but the Q's peaked at 8.24×10^6.

Since this value was considerably lower than the quality factors measured before the fused silica suspensions had been attempted, the mass was retested on silk thread. The best result achieved this time was only 1.17×10^7, suggesting that the initial welding had damaged the mass in some way, most probably by putting stresses into the mass at the bond. The results measured with a thread suspension were still better than those for fused silica suspensions, though, so further attempts were made.

To increase the amount of isolation in the system, thereby reducing any potential coupling of the suspension to the outside world (and hence damping), an intermediate fused silica mass was incorporated within the suspension. This took the form of a cylinder, roughly 2.5 cm thick and 1.5 cm (later increased to 3 cm) long. The "T" piece was also replaced with a complete "T" made from 2 mm rod which sat atop the post. The fused silica block that was clamped was replaced with a cylindrical piece, and the clamp replaced with a "V" to hold it in place. The clamp block was also moved to the top of the cradle stand to allow for longer first stage fibres to be employed. The best Q measured with these changes was 9.74×10^6. This approximate value was recorded several times and it was accepted that this was the best result likely to be measured. The results are summarised in figure 6.6 and the changes made to the suspension are sketched in figure 6.7.

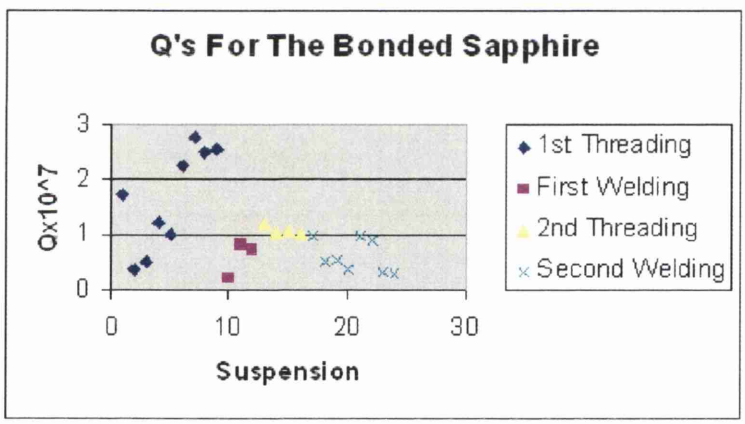

Figure 6.6: *Graph showing the sapphire results after bonding.*

Due to the damage that was caused to the mass by the heat stresses, it is not possible to confidently reach conclusions regarding the effect of cross-bonding sapphire to fused silica. The results obtained prior to the application of the first "T" piece suggest that the quality factor was degraded by a factor of 10 over the original condition, but whether or not this is a true measure of the

intrinsic Q, or whether this was limited by suspension losses is unknown.

If it is assumed that the difference in measured Q's before and after bonding is a result of the bonding alone, it is possible to estimate the excess loss due to the bonding, $\phi_1(\omega_0)_{\text{excess}}$.

$$\phi_1(\omega_0)_{\text{excess}} = \frac{1}{Q_{\text{after bonding}}} - \frac{1}{Q_{\text{before bonding}}} \tag{6.1}$$

$$= \frac{1}{2.76 \times 10^7} - \frac{1}{2.59 \times 10^8}$$

$$= 3.23 \times 10^{-8} \tag{6.2}$$

This loss can be scaled to provide an estimate of the loss associated with the bond on another mass, $\phi_2(\omega_0)_{\text{excess}}$, using the relation shown below in equation 6.3 [57]:

$$\phi_2(\omega_0)_{\text{excess}} = \phi_1(\omega_0)_{\text{excess}} \frac{A_2 m_1}{A_1 m_2} \tag{6.3}$$

where A_1 and A_2 are the bond areas for the two masses m_1 and m_2. For the case of the mass tested here, $m_1 = 0.28$ kg and $A_1 = 0.79$ cm^2. If this is scaled up to the case for a sapphire mass of GEO scale ($m_2 = 6$ kg and $A_2 = 6$ cm^2), the estimate of the expected excess loss due to the bond is found to be 1.23×10^{-8}. The estimated loss for a GEO fused silica mass using KOH bonding is $\sim 2 \times 10^{-8}$ - derived using the method from [57] for current GEO specifications. So the cross-bonding result is roughly twice as good as that for fused silica, though whether this can be further improved upon is not known given the problems that were subsequently encountered.

To estimate the worst case of the loss of the sodium silicate bond, the following

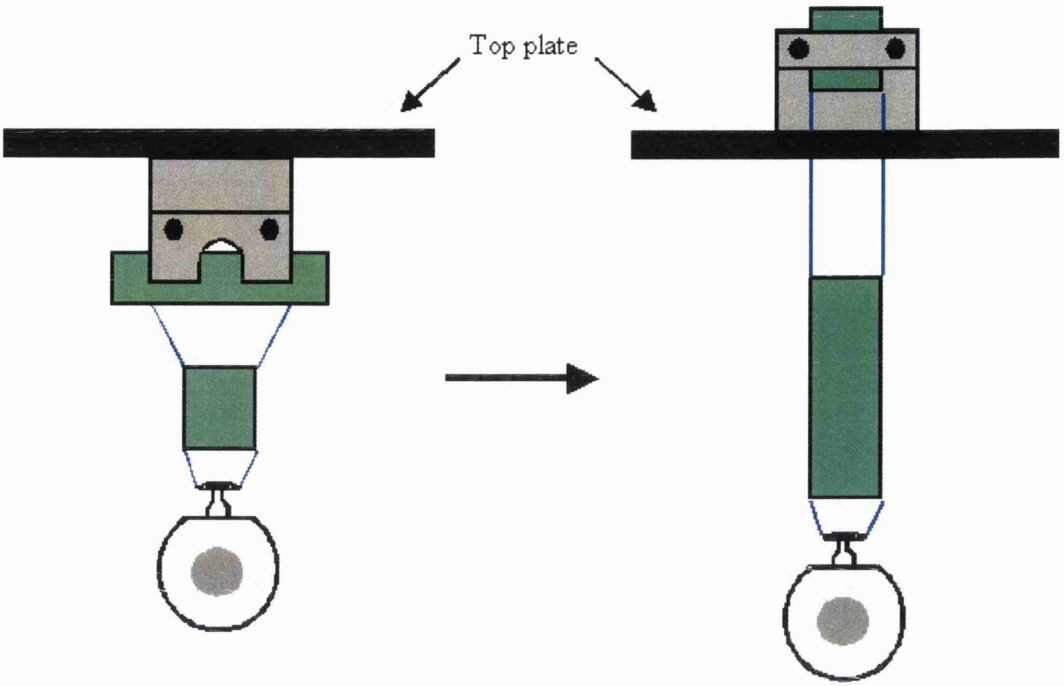

Figure 6.7: *Summary of the changes made to the fused silica suspension.*

analysis can be performed. Consider the fundamental longitudinal mode. Let the length of the sapphire mass be L, cross-sectional area $S = \pi r^2$ and Young's modulus Y. Now, the energy density $= \frac{1}{2}$stress $\times$ strain. Consider an element at x, of thickness dx.

$$\text{Strain} = \frac{d\psi}{dx} \tag{6.4}$$

and

$$\text{Stress} = Y \times \text{Strain} = Y\left(\frac{d\psi}{dx}\right) \tag{6.5}$$

Hence, the energy in a volume element is

$$\begin{aligned}\Delta E &= \frac{1}{2}Y\left(\frac{d\psi}{dx}\right)\left(\frac{d\psi}{dx}\right)Sdx \\ &= \frac{1}{2}YS\left(\frac{d\psi}{dx}\right)^2 dx \end{aligned} \tag{6.6}$$

Now, let $\psi = Asin(kx)$, so $\frac{d\psi}{dx} = Akcos(kx)$ therefore,

$$\begin{aligned}\Delta E &= \frac{1}{2}YSA^2k^2cos^2(kx)dx \\ &= \frac{1}{2}YSA^2k^2 \times \frac{1}{2}[1 + cos(2kx)]dx\end{aligned}$$

So, the energy in a distance Δx from 0, the midpoint of the mass, is

$$\begin{aligned}E &= \frac{1}{4}YSA^2k^2\int_0^{\Delta x}[1 + cos(2kx)]dx \\ &= \frac{1}{4}YSA^2k^2\left[x + \frac{sin(2kx)}{2k}\right]_0^{\Delta x}\end{aligned} \tag{6.7}$$

Now, let $\Delta x = L/2$. Hence,

$$E_{\text{half bar}} = \frac{1}{4}YSA^2k^2\frac{L}{2} = \frac{1}{4}YSA^2k^2 \times 0.05 \tag{6.8}$$

The energy stored in half the bond (where the bond is of diameter 1 cm) is

$$
\begin{aligned}
E &= \frac{1}{4}Y'S'A^2k^2 \int_0^{5\times10^{-3}} [1 + cos(2kx)]dx \\
&= \frac{1}{4}YSA^2k^2 \left[x + \frac{sin(2kx)}{2k}\right]_0^{5\times10^{-3}} \\
&= \frac{1}{4}Y'S'A^2k^2 \times 9.92 \times 10^{-3} \qquad (6.9)
\end{aligned}
$$

From this and equation 6.8, the ratio of energy stored in the bond to that in the bar can be estimated:

$$\frac{E_{\text{bond}}}{E_{\text{bar}}} = 2.26 \times 10^{-7} \qquad (6.10)$$

This assumes that the Young's moduli of the mass and the bond are the same, and that thickness of the bond is 80 nm. (This thickness is based on examination of a sodium silicate bond under an atomic force microscope - more details of which are discussed in the following section.) The loss of the bond is therefore $\phi_{\text{bar}}/2.26 \times 10^{-7}$. So the loss is 0.14. This result is unphysical, though, and can only serve as a worst case scenario estimate. The result suggests that either the assumption that $Y = Y'$ or the thickness of the bond was incorrect.

Further work is clearly required to determine the full effect of cross-bonding, and at present the bonded post has been successfully removed without damaging the mass. Work can now begin again, taking account of lessons learned from the first attempt.

6.4 Further Loss Measurements

In this section bonding pieces of fused silica to fused silica using sodium silicate bonding is discussed. Here sodium hydroxide taking the place of the potassium hydroxide and silica filler being present. Two different samples were investigated to determine whether this variation on the bonding technique was as good, in terms of mechanical loss as the KOH bonding. The interest stems from the fact that the sodium silicate bonding is stronger by a factor of ~ 2 over KOH bonding [95].

Bonding Flats to a Mass

This first mass was of fused quartz, 6.3 cm in diameter and 7 cm long. Along its length a flat had been polished to which a fused silica post had previously been bonded. This mass had been used in the original tests to see what effect hydroxide-catalysis bonding had on the internal losses [57]. The original bond had put the post in the centre of the flat, and to this two optical fused quartz flats would be added, to either side of the original post. 0.5 μl of sodium silicate solution was used for the first bond. As this cured, though, a dry patch became evident (and is visible under the left hand flat in figure 6.8). When the second flat was added, 1 μl of solution was used, and the bond showed no signs of dry patches.

Before the bonding was carried out, the mass was retested. The best result obtained was 1.80×10^6, which was higher than the best recorded during the original testing (1.40×10^6). This was probably a sign that the suspension techniques had improved over the earlier condition or that the bond had matured with age. The mass was again cleaned, then bonded. (Again, bonding was performed by E. Elliffe and J. Hough.) The resulting combination is shown in figure 6.8.

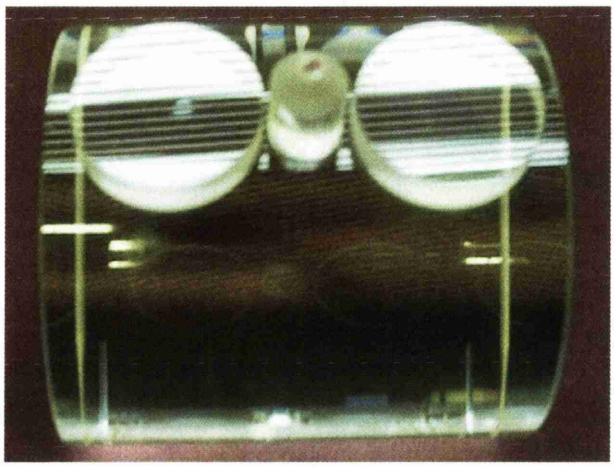

Figure 6.8: *Picture of the posted mass.*

Once more, the Q of the fundamental longitudinal mode was found to have fallen from the previous levels. In this case, the highest quality factor was 7.15×10^5. Again, other modes were then tested, the best of them yielding a Q of 8.20×10^5, this mode again thought to be the asymmetric drum mode. Once again, McMahon [80] was used for initial mode identification. The highest results for each of the modes are shown in table 6.2.

Mode	Frequency (Hz)	Q $\times 10^5$
Fundamental	39108	7.15 ± 0.08
Bar	39639	1.71 ± 0.05
Asymmetric Drum	47820	8.20 ± 0.08
Symmetric Drum	49040	6.86 ± 0.03
Bar	58457	3.85 ± 0.16
Bar	59214	3.48 ± 0.01

Table 6.2: *Results of Q measurements of several modes of the posted quartz mass.*

As with the case for the bonded sapphire in the earlier section, the excess loss associated with the bond for the measured sample and a GEO-sized mass can

be estimated. Using equations 6.1 and 6.3 these are 8.44×10^{-7} and 7.55×10^{-8} respectively. This latter result is of the same order as that for the estimated loss for a KOH bonded GEO-mass.

The same approach to determine the worst case scenario for the loss of the bond as used for the case of the sapphire mass can also be used again here. Again, the fundamental longitudinal mode was considered. Figure 6.9 shows the various parameters related to this calculation.

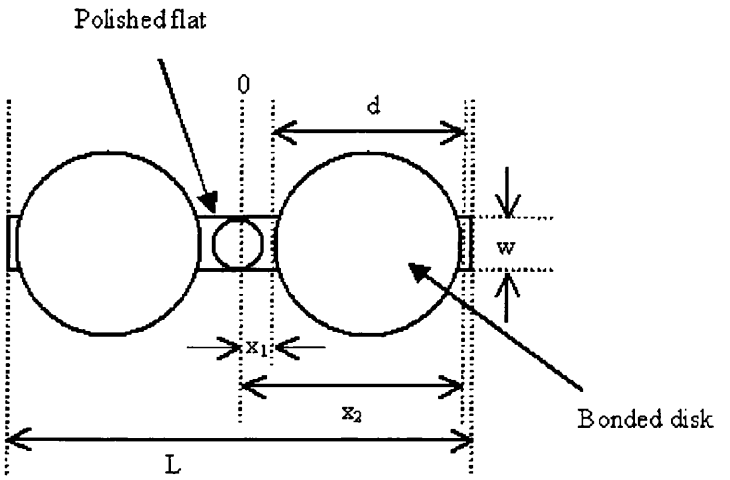

Figure 6.9: *Schematic of the "posted" mass.*

As before, consider the half bar. (i.e. that to the right of the "0" line.) In this case, the bond can be taken as a cuboid of length d, width w, thickness t and cross-sectional area S'. The energy stored in the bond, $E_{\text{in bond}}$, can be expressed as

$$
\begin{aligned}
E_{\text{in bond}} &= \frac{1}{4}S'A^2k^2Y' \int_{x_1}^{x_2} [1 + cos(2kx)]dx \\
&= \frac{1}{4}S'A^2k^2Y' \left[x + \frac{sin(2kx)}{2k}\right]_{x_1}^{x_2} \\
&= \frac{1}{4}S'A^2k^2Y' \left[(x_2 - x_1) + \frac{1}{2k}(sin(2kx_2) - sin(2kx_1))\right] \quad (6.11)
\end{aligned}
$$

Now, as before, $k = \frac{\pi}{L}$, where this time $L = 7$ cm. Also, $x_1 = 6$ mm and $x_2 = 31$ mm. Hence, equation 6.11 becomes

$$
E_{\text{in bond}} = \frac{1}{4}S'A^2k^2Y' \times 0.0254 \quad (6.12)
$$

As for the case for the sapphire mass, the energy stored in half the bar, $E_{\text{half bar}}$ is given by

$$
\begin{aligned}
E_{\text{half bar}} &= \frac{1}{4}SA^2k^2Y\frac{L}{2} \\
&= \frac{1}{4}SA^2k^2Y \times 0.035 \quad (6.13)
\end{aligned}
$$

Hence,

$$
\frac{E_{\text{bond}}}{E_{\text{bar}}} = 0.73\frac{S'}{S}\frac{Y'}{Y} = 0.73\frac{S'}{S} \quad (6.14)
$$

once again assuming that the Young's modulii of the bond and bar are the same. Now, $S' = wt$ and $S = \pi r^2$, where $w = 1.15$ cm and $r = 3.15$ cm, the radius of the test mass. So, equation 6.14 becomes

$$\frac{E_{\text{bond}}}{E_{\text{bar}}} = 2.34t \tag{6.15}$$

Again, if t is taken to be 80 nm, this results in

$$\frac{E_{\text{bond}}}{E_{\text{bar}}} = 1.87 \times 10^{-7}$$

and

$$\phi_{\text{bar}} = \frac{1}{7.15 \times 10^5} - \frac{1}{1.8 \times 10^6} = 8.44 \times 10^{-7}$$

then,

$$\phi_{\text{bond}} = \frac{8.44 \times 10^{-7}}{1.87 \times 10^{-7}} = 4.5 \tag{6.16}$$

This result is unphysical. This suggests that either the assumption that $Y = Y'$ was wrong, or that the bond thickness was incorrect.

New Mass from Old

So far bonding of two fused silica/quartz samples has always taken place with a small bonding area (typically 1 - 2 cm^2). As part of the investigation of sodium silicate bonding, it was decided to attempt a bonding employing a much larger area. For this, two nominally identical fused quartz masses were used. Each mass was 6.3 cm in diameter and 7 cm long. They were to be joined together at their ends, thereby creating a 14 cm long mass. This meant that the bonding area would be $\sim$ 30 cm^2. Once the faces to be jointed were thoroughly cleaned, five measures of 2.5 μl of sodium silicate solution were placed about the centre of the face of one of the masses, then the faces brought together and the bond then left to cure. Before the masses were bonded, though, their

internal quality factors were measured. For this, the fundamental longitudinal modes for the pair (at 40050 and 40070 Hz respectively) were excited in the usual fashion. Six suspensions were conducted for each mass, and the highest Q's were $(1.40 \pm 0.02) \times 10^6$ and $(1.35 \pm 0.03) \times 10^6$. The masses were then cleaned and bonded (by E. Elliffe and J. Hough). The resultant, "doubled" fused quartz mass is shown in figure 6.10.

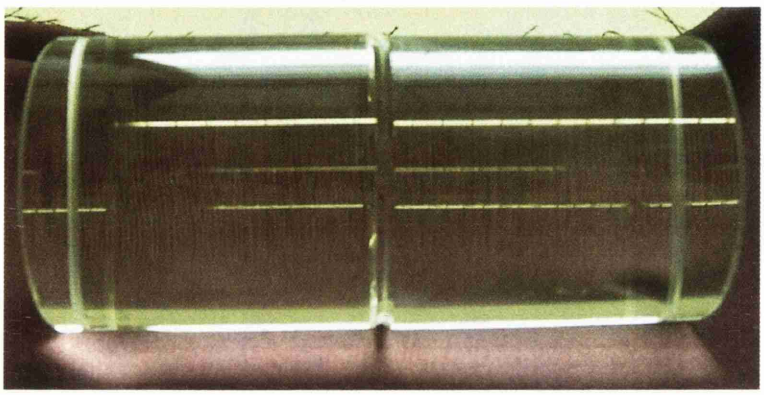

Figure 6.10: *Picture of the doubled fused quartz mass.*

Once the mass's bond had been allowed to cure, testing resumed. It should be noted that, as can be seen in 6.10, both the original masses had pronounced chamfer at the corners of the mass. This produced a trench at the mid-point of the doubled mass where the suspension thread would sit. Initial tests showed that the fundamental mode had fallen by roughly a factor of 10 over the original results, the highest value being 1.78×10^5. Other modes were then tested, and these results varied. One of them, thought to be the asymmetric drum, had a Q that peaked at 1.21×10^6. The highest results for each of the modes tested are shown in table 6.3. The modes were initially identified by using the work of McMahon [80]. The aspect ratio of this mass was beyond the range covered by McMahon, and so modes had to be extrapolated. Correlation was therefore hard to achieve conclusively. Subsequently, Algor was used to model the mass and it was from this that the mode allocation in table 6.3 was made.

At first look, the Q results suggest that sodium silicate bonding does not significantly increase the losses. The fundamental mode's very low Q may be a result of the thread sitting within the trench formed by the mass chamfers. Visual inspection showed that the bond had not reached the very edges of the overlapping faces - implying that not enough bonding solution was used. It was therefore possible that the thread slipped partially between the masses, making the contact more lossy than would have been the case had the line of suspension been as smooth as is usually the case.

Mode	Frequency (Hz)	Q $\times 10^5$
Fundamental	20411	2.68 ± 0.03
Bar	35440	3.86 ± 0.07
Asymmetric Drum	50995	12.08 ± 0.05
Higher Order Drum	53437	9.23 ± 0.04
Higher Order Drum	61462	11.15 ± 0.39

Table 6.3: *Results of Q measurements of several modes of the doubled fused quartz mass.*

To again estimate a worst case of the loss of the sodium silicate bond itself, the same approach employed for the bonded sapphire mass was applied. Again consider the fundamental longitudinal mode. Let the combined mass be of length L, cross-sectional area $S = \pi r^2$ and Young's modulus Y. Here the are of the bond, $S' = \pi r^2$ and the Young's modulus is again Y'. So, the energy in half the bar is

$$
\begin{aligned}
E_{\text{half bar}} &= \frac{1}{4}YSA^2k^2\int_0^{L/2}[1+cos(2kx)]dx \\
&= \frac{1}{4}YSA^2k^2\left[x+\frac{sin(2kx)}{2k}\right]_0^{L/2} \\
&= \frac{1}{4}YSA^2k^2\frac{L}{2} \qquad (6.17)
\end{aligned}
$$

Now let the thickness of the bond be B, where $B \ll L$. So, if $\Delta x = B/2$, then

$$E_{\text{half bond}} = \frac{1}{4}Y'SA^2k^2B \qquad (6.18)$$

So,

$$
\begin{aligned}
\frac{E_{\text{bond}}}{E_{\text{bar}}} &= \frac{\frac{1}{4}Y'SA^2k^2B}{\frac{1}{4}YSA^2k^2\frac{L}{2}} \\
&= \frac{2B}{L}\frac{Y'}{Y} = \frac{2B}{L} \qquad (6.19)
\end{aligned}
$$

if the Young's moduli of the bond material and the mass is the same. Now, if ϕ_B is the loss of the bond material, then

$$\phi_{\text{bar}} = \frac{2B}{L}\phi_B \qquad (6.20)$$

Now, as can be seen from table 6.3, for the fundamental mode $\phi_{\text{bar}} = (2.68 \times 10^5)^{-1} - (1.40 \times 10^6)^{-1}$. Measurement of the bond with a atomic force microscope (performed by E. Elliffe) gave the thickness as 100 nm. Substituting these values into equation 6.20 gives

$$\phi_B = \frac{4.23 \times 10^{-7}}{200 \times 10^{-9}} = 2.11 \tag{6.21}$$

So once again, an unphysical result is produced, close to that found for the previous fused quartz mass. This further confirms the suspicion that either the assumption that $Y = Y'$ or that $t = 100$ nm are incorrect.

Subsequent modelling of the doubled mass by D. Crooks using the same techniques as those described in Chapter 5 have found that the higher order drum mode at 53437 Hz has a similar energy ratio to that of the fundamental mode. When this is then converted into a loss, it yields a loss for the bond of 0.27, an improvement over the initial calculation, though still unphysical. Investigations by S. Bull from the University of Newcastle also suggest that the Young's modulus of the bond is in fact 10 GPa rather than 72 GPa (for fused silica). Incorporation of this improves the loss to 0.038. Further analysis is continuing.

6.5 Conclusions

Previous experiments had shown that KOH bonding of a fused silica post to a fused silica cylinder resulted in a joined sample with internal losses not significantly increased. Initial testing of a piece of sapphire with a fused silica post bonded to it using sodium silicate showed a factor of 10 decrease in the measured quality factor of the mass. When this translated into an estimate for the excess loss related to the bonding for a 6 kg mass, as used in GEO, it suggested that the loss of the bond was a factor of 2 better than for the case of two fused silica pieces bonded together using a KOH solution. However, extensive testing of this mass was not feasible at it appeared that it had suffered damage through welding of fused silica fibres to the bonded post. This highlighted the need for considerable care when undertaking welding.

When the effect of jointing fused silica to fused silica with a sodium silicate solution was investigated measurement of the internal Q's before and after showed a decrease again. Analysis of the excess loss due to the bond again gave results within an order of magnitude for the result for KOH bonding. Calculations to try to estimate directly the loss of the bond itself resulted in unphysical answers. Since both results gained were unphysical, it suggests that assumptions made common to both calculations may not have been correct. Possible problems were that the Young's modulus of the bond and mass were very different and the thickness of the bond was not accurately represented by the atomic force microscope. Further work on both masses is required before a firm conclusion can be reached for this technique.

Chapter 7

Conclusions

Predicted at the beginning of the last century by Einstein in his General Theory of Relativity, gravitational waves were indirectly proven to exist by Hulse and Taylor in the 1970's. Across the world, ground based long baseline interferometers (GEO 600, VIRGO, TAMA 300 and the first stage LIGO) may detect them directly within the next year or so, having sensitivities in the range $\sim 10^{-21}$ to $10^{-22}/\sqrt{\text{Hz}}$ over a detection band between a few Hz to a few kHz. In particular, GEO 600 should be operational within the next year and will be able to search for continuous sources of gravitational waves, such as pulsars. GEO 600 will also form a part of a network of long baseline detectors that will allow for coincidence observations of burst sources to be made. The position of such a source is determined by comparison of the arrival time of the gravitational wave signals at the various detectors in the network. In the fullness of time, this ground-based network will be augmented by space-based detectors, such as LISA. These will increase the bandwidth over which the gravitational waves search can be carried out.

One of the main limiting factors to the sensitivities of ground-based is thermal noise. The fluctuation-dissipation theorem is a very useful equation in determining the levels of the thermal noise. By using the information it provides,

interferometric gravitational wave detectors can be designed in ways that will reduce the level of this thermal noise. Prediction of the total level of thermal noise is not as simple as once thought, though. The technique of mode decomposition only works if the test mass is homogeneous. When this is not the case, greater care is required. Consideration instead of how energy transferred to the suspended mass is dissipated is required. And whilst the overall sensitivity of the detectors currently under construction will still be set by the intrinsic losses of the materials from which the suspension is constructed, in future advanced detectors the limit may come from thermal expansion effects within the materials. In particular, this will come into effect if sapphire with its very high intrinsic quality factor, is selected to replace fused silica in these advanced detectors.

To measure the high quality factors that are desirable to minimise the effects of thermal noise requires considerable care. Samples under study must be isolated, as far as is possible from the outside world. This is best achieved by suspending the samples as pendulums. The loop that supports the masses must be clamped firmly and smoothly. It must be made from a suitable material, preferably silk thread or polished wire. The polishing is important as it improves the smoothness of the metal. The loop and line of contact it makes with the mass must be lubricated, and its length should be selected with care so as to avoid any overlapping between the excited internal mode and multiples of the violin modes in the wire. The easiest way to achieve this is to keep the suspension length as short as possible. This procedure has the added advantage that it makes the balance of the suspended mass more stable as it keeps the break off point of loop and mass well above the centre of mass of the sample. This means that the bulk motion of the mass is minimised, making it easier for the electronic feedback system in the interferometer that interrogates the mass to "lock". Finally, the mass should be investigated under vacuum in

order to remove the problem of gas damping from the air.

In order for ground-based gravitational wave detectors to be sensitive enough they must meet certain requirements. One of these is that the materials from which the interferometer mirrors are manufactured are have a low mechanical loss, or equivalently a high quality factor, Q. For GEO 600, this requirement Q is 5×10^6. It is already known that fused silica has a quality factor in excess of this requirement. The best sample recorded in Glasgow and presented in this thesis is a Q of 2.39×10^7, and this material is being used in all current ground-based detectors. Some of the samples tested, though, did not yield Q's of this order. This highlighted the importance of great care when the samples are being manufactured and polished if their losses are to be maintained.

Tests carried out on yttrium aluminium garnet (YAG) have shown that it possesses a Q considerably higher than that of fused silica, though this was only achievable when the barrel of the samples was well polished. When this mass was repolished, improving the surface smoothness, it had the result that the best measured result more than doubled, from an initial value of 2.9×10^7 to 7.3×10^7. Other materials, such as gadolinium gallium garnet (GGG) and spinel also look like promising contenders for future detectors, though it has yet to be determined whether large enough samples can be produced.

The current front-runner to replace fused silica, though, is sapphire. It has been known since the 1970's that samples grown using the horizontal oriented crystallization growth have Q's in excess of $\times 10^8$. Tests carried out on samples manufactured by the heat exchanger method, a process which should be capable of producing samples of the size needed for ground-based interferometric gravitational wave detectors, have shown that they can match these earlier very high Q's. The best sample measured in Glasgow yielded a Q of 2.59×10^8, the highest quality factor measured outside of Russia. Once again, though,

not all HEMEX samples performed as well as this, highlighting once again the importance of the condition of a sample when measuring it. That aside, these very high quality factors suggest that this type of sapphire could be used for the test masses in the advanced stages of interferometric gravitational wave detectors. However, its relatively high thermal expansion coefficient means that its attractiveness as a mirror substrate is not as clear-cut since this results in a higher level of noise as a result of thermoelastic effects, which will limit the sensitivity.

In order for these test substrates to be employed as mirrors in interferometric gravitational wave detectors, they must have a dielectric coating applied to their front faces. Experiments performed on coated samples of fused silica suggest that the effect of these coatings on the thermal noise of silica masses will be significant for advanced detectors. Preliminary experiments on sapphire suggest a similar damping effect by the coating. Initial analytical calculation of the coating loss suggests that the loss is roughly 8 times higher than that for fused silica. There is much more work to be done in this area, though. Specifically, systematic testing of samples before and after coating and variations in coating types and thicknesses is required for both fused silica and sapphire.

Another factor that can cause a reduction in the quality factor of a test sample is the technique used to suspend it, as mentioned above. For the case of the actual interferometric detectors, the process used to join the sample to its suspension must be very low loss. For GEO 600 the technique being used is hydroxy-catalysis bonding. It has been shown previously that using this type of bonding between two pieces of fused silica does not have a large effect on the intrinsic Q of the samples. Initial testing of a piece of sapphire with a fused silica post bonded to it using sodium silicate showed a factor of 10 decrease in the measured quality factor of the mass. When this translated into

an estimate for the excess loss related to the bonding for a 6 kg mass, as used in GEO, it suggested that the loss of the bond was a factor of 2 better than for the case of two fused silica pieces bonded together using a KOH solution. However, extensive testing of this mass was not feasible at it appeared that it had suffered damage through welding of fused silica fibres to the bonded post. This highlighted the need for considerable care when undertaking welding.

When the effect of jointing fused silica to fused silica with a sodium silicate solution was investigated measurement of the internal Q's before and after showed a decrease again. Analysis of the excess loss due to the bond again gave results within an order of magnitude for the result for KOH bonding. Calculations to try to estimate directly the loss of the bond itself resulted in unphysical answers. Since both results gained were unphysical, it suggests that assumptions made common to both calculations may not have been correct. Possible problems were that the Young's modulus of the bond and mass were very different and the thickness of the bond was not accurately represented by the atomic force microscope. Further work on both masses is required before a firm conclusion can be reached for this technique.

The work presented in this thesis has highlighted the need for great care in the selection and manufacturing of test materials for interferometric gravitational wave detectors. Whilst there are a number of materials that meet the low loss requirements for a test mirror, the effect of turning them into mirrors by the application of dielectric coatings must be taken into account. For fused silica the effect is reasonably well understood, but this is not so for sapphire. Work to clarify this will continue in Glasgow, as will further testing of sodium silicate bonding and cross bonding.

Appendix A

Details of Interferometric Feedback System

As discussed in Chapter 3, in order to detect the thermal motion in the front face of a test mass, a two-stage feedback system was used to remove the bulk, low-frequency, higher amplitude, motion of the test masses. This allowed the internal resonance modes to be located and excited. Here the specifics of the feedback filtering is presented.

A.1 First Stage Filtering

The circuit detailed in figure A.1 is a series of active filters. These take the interferometric signal from the photodiode and invert it (Part (i) in figure A.1). It is then filtered by a two-filter combination (Part (ii)). The circuit also allows for the signal to be amplified or reduced as required, as well as its D.C. level adjusted. The signal is then sent to a piezo loudspeaker, and via a second stage of filtering to a moving coil loudspeaker.

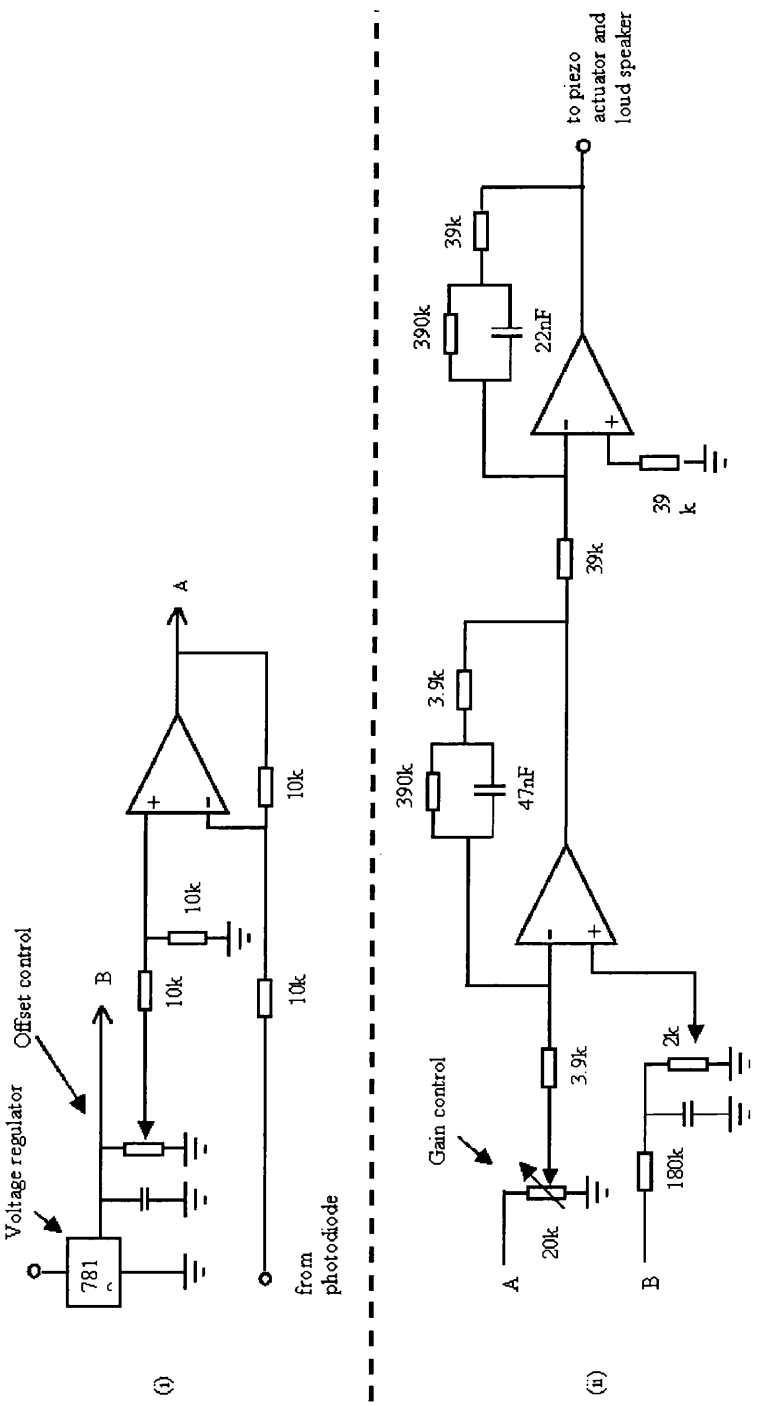

Figure A.1: *Circuit Diagram for feedback filtering.*

A.2 Second Stage Filtering

The second stage in the feedback system was a simple low-pass filter. This was created using a Stanford Research Systems [96] SR560 low-noise pre-amplifier. This could be set to act as a range of filters whose corner frequencies and gains could be adjusted to suit the individual situation. Typically, the low-pass filter corner frequency was 3 Hz and the gain between 1 and 10.

Appendix B

Recording Ringdowns of Resonances

As is detailed earlier in this thesis, the method for measuring the quality factors of the internal resonance modes of a test mass was to excite each individual mode and then allow them to decay. This decaying signal was fed through a lock-in amplifier that beat the signal against a constant source set at $\sim$ 5 Hz above the resonant frequency. This resulted in a decaying signal with frequency $\sim$ 5 Hz. This was done because neither of the two systems detailed below could record a signal with a frequency in the 10's of kHz range.

Chart Recorder

Initially, the decaying output was recorded on a Graphtec Linearcorder [97] chart recorder, the recording rate adjusted as required by the speed of the decaying sine wave signal, i.e. related to the Q of the mode. By measuring the amplitude of this ringdown at various stages, and plotting these as per equation 4.7, the quality factor could be calculated. Figure B.1 shows three such ringdowns. These were for a resonance of 25402 Hz and resulted in Q's of 7.32×10^6 , 7.13×10^6 and 7.25×10^6 respectively. This method could lead

to inaccuracies in the results since it was dependent on accurate measuring of the amplitude by hand. It also used only a small amount of the recorded data to calculate the Q. This method was therefore replaced in time with a computer-based data acquisition programme.

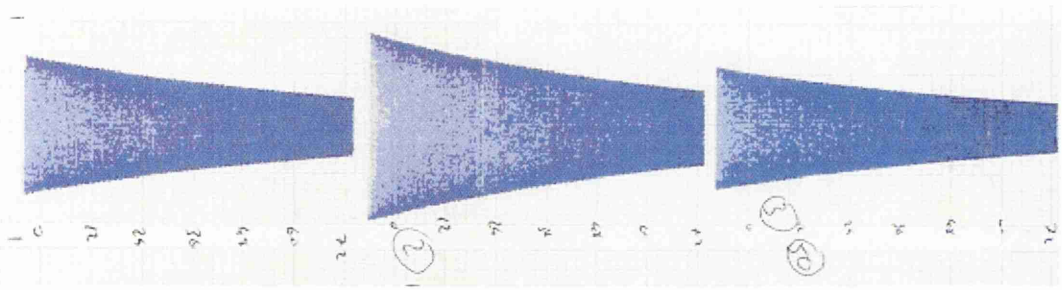

Figure B.1: *Three typical ringdowns recorded on the chart recorder. Each ring is measured over 72 seconds.*

Data Acquisition Programme

In this set up, the decaying signal from the lock-in amplifier was fed through an Industrial Instruments [98] ADC board to a PC running a LabView program[1]. The front panel of this programme is shown in figure B.2.

This acquisition programme allows for variation in the number of data points recorded per second, up to 250. The number of these points plotted is also variable. This data is recorded in a text file, which was then analysed in an Excel spreadsheet. The spreadsheet takes the raw data (first column in figure B.3) and calculates the total average of these points. The absolute value of the difference of the data from this average is then calculated (column 3), and then a running average of this plotted, each point being averaged over the fifty to either side. (Column 4) The gradient of the best fit straight line through these points is then found, its gradient being used to determine the Q of the decay.

[1]Program written by Jenifer Lotz

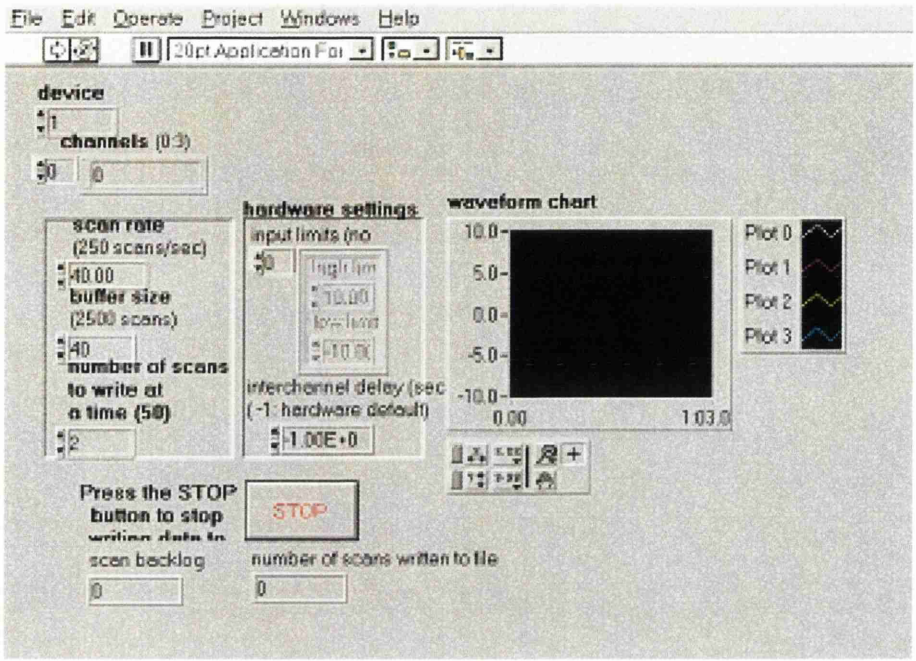

Figure B.2: *Front panel of the data acquisition programme.*

This technique allowed for the use of all recorded data in the calculation of the quality factor. Whilst both techniques would result in the same Q for a particular decay, the computer programme was more efficient in time.

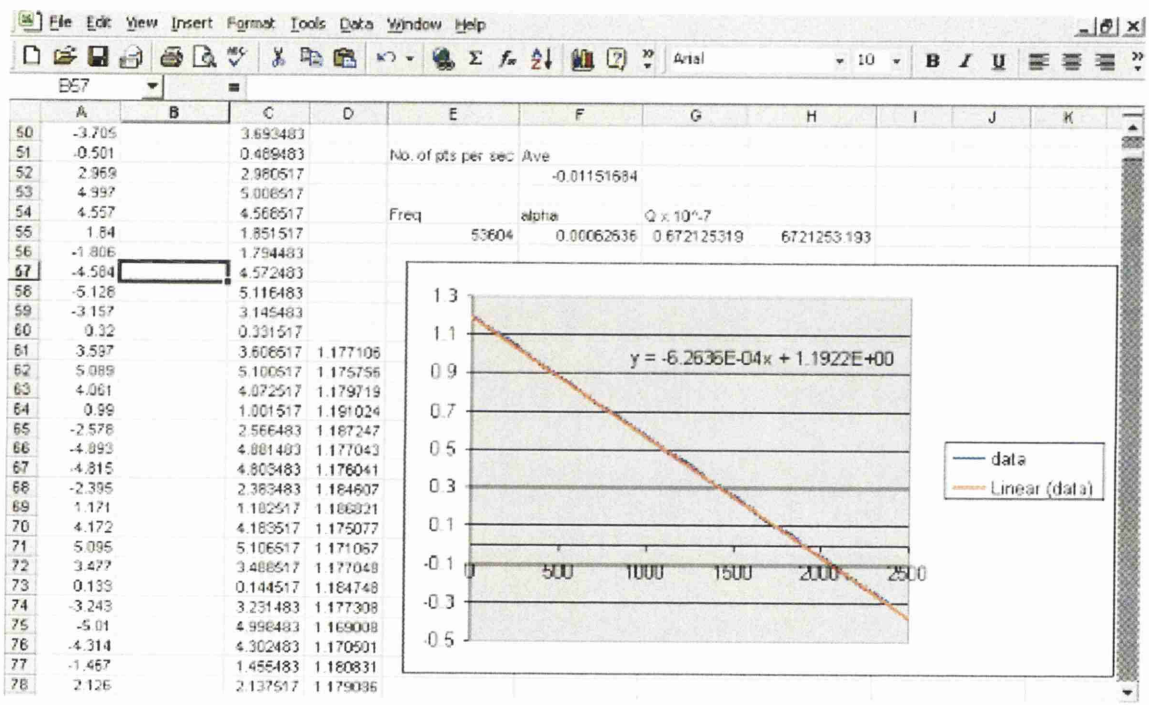

Figure B.3: *Analysis spreadsheet.*

Appendix C

Algor

C.1 Introduction

Algor [81] is a finite element analysis programme that employs linear static and dynamic stress analysis capabilities to determine stresses, displacements and natural frequencies. Additionally, it can predict the dynamic response to static and dynamic loading.

C.2 Building up an Algor Model

To model a particular test sample, a three dimensional mesh must be constructed. This is built up in stages. For the case of a cylindrical test mass, this is done as follows. Firstly, a line equal in length to the diameter of the mass is drawn. This is subdivided into n sections. This line is then revolved about its midpoint, creating a disc. Each point along the diameter lines is connected to the equivalent in the next one. Once the disc is complete, it is then copied in the "z-direction", stacking the discs until a cylinder is formed of the desired height. Again, each point in the discs is connected to its counterparts above and below. Once the cylindrical mesh is complete, the natural resonance frequencies can be determined. The number of points in the mesh

can be increased or decreased, depending on the level of accuracy required; the more points used, the more accurate the calculated frequencies.

In the section that follow, final mode pictures for various resonances for a fused silica test mass (diameter 12.5 cm and height 10 cm) are shown. These highlight the fact that as well as generating the mode frequencies and shapes, Algor can also determine the relative amount of movement throughout the mass. It was the determination of this movement, specifically in the faces of the mass, that allowed the calculation of the energy ratios quoted in Chapter 5.

C.3 Example Mode Shapes

The modes shown in the following figures were those excited as part of the tests to investigate the effect of coating the Corning fused silica test mirrors, detailed in Chapter 5.

Figure C.1: *Bending mode at 22105 Hz.*

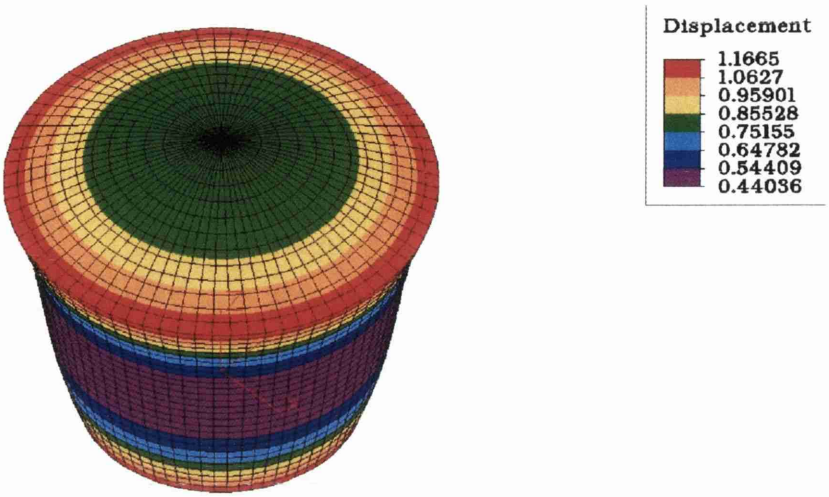

Figure C.2: *Asymmetric drum mode at 22977 Hz.*

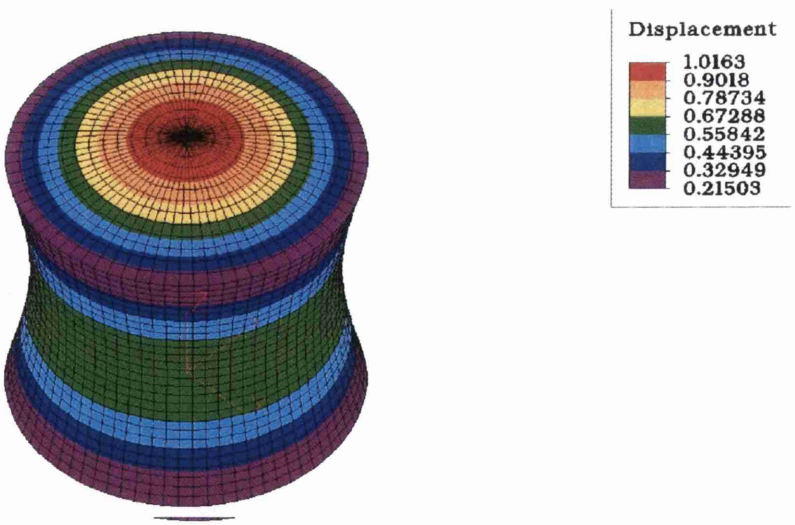

Figure C.3: *Fundamental longitudinal mode at 25378 Hz.*

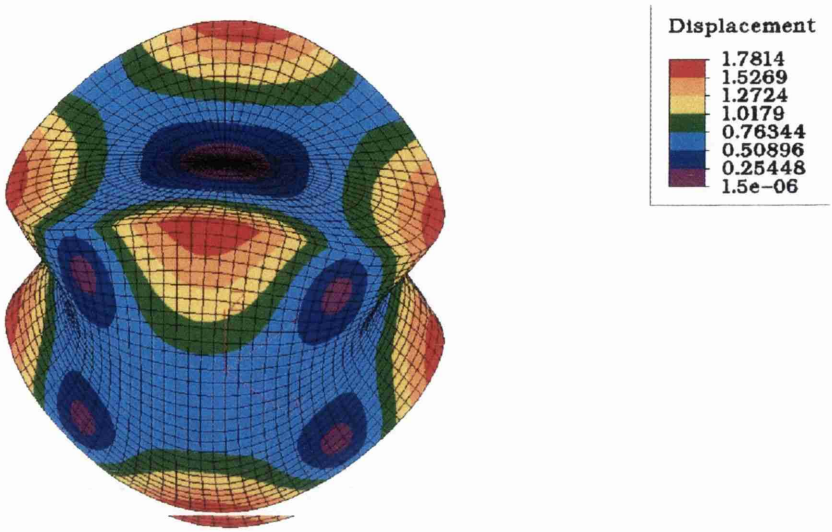

Figure C.4: *Clover 4 mode at 26176 Hz.*

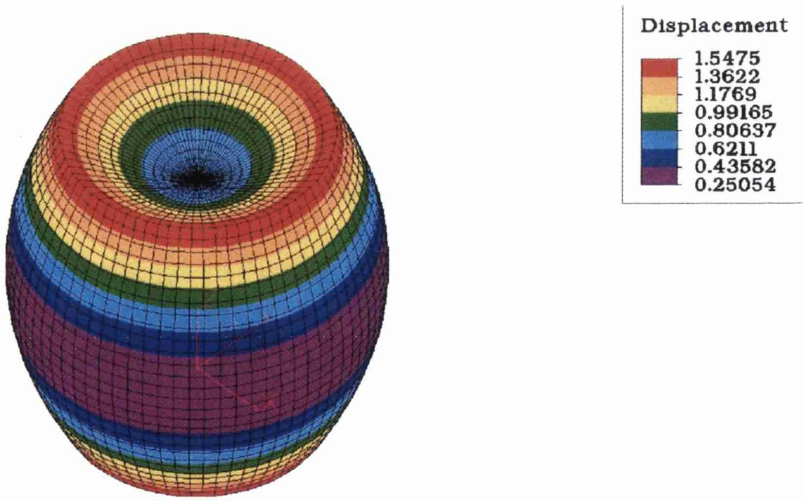

Figure C.5: *Symmetric drum mode at 28388 Hz.*

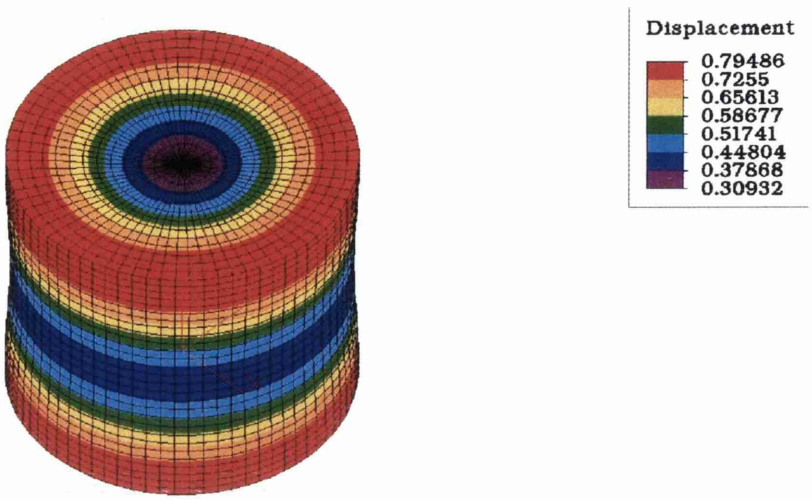

Figure C.6: *Expansion mode at 31710 Hz.*

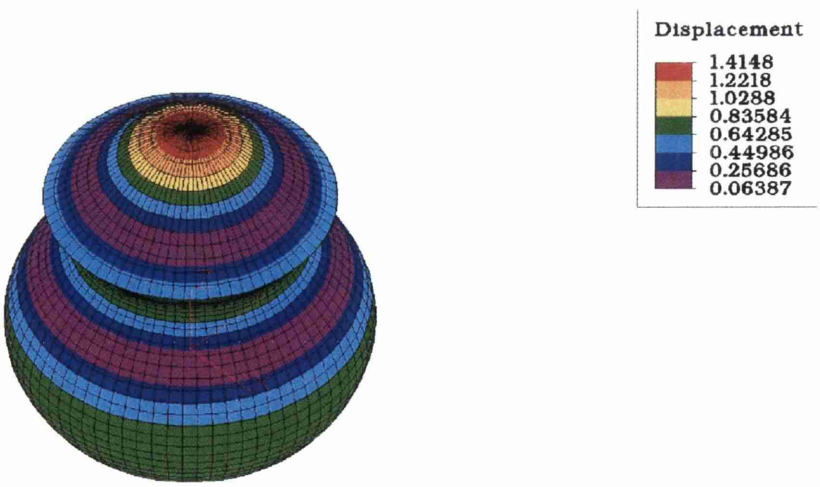

Figure C.7: *2nd asymmetric drum mode at 36045 Hz.*

Appendix D

Strain Energy

In Chapter 5, energy ratios are used to determine the losses associated with dielectric mirror coating of test masses in addition to other factors. To obtain these ratios, the energy in the coating and substrate are required. These energies are due to strain within the coating and substrate. Here, some aspects of strain as well as strain energy are discussed.

D.1 Definition of Strain

Consider a one dimensional bar, as shown in figure D.1. If a force is exerted upon this bar, causing it to extend, then the length of the bar x becomes $x+u$, where u is the extension. Similarly, a section of the bar Δx becomes $\Delta x + \Delta u$. Strain is defined as the ratio of change in length to the original length. If the section of the bar is considered, then

$$\text{strain} = \frac{\text{change in length}}{\text{original length}} = \frac{\Delta u}{\Delta x} \tag{D.1}$$

which tends to $\frac{du}{dx}$ as $x \rightarrow 0$. This can be described as an extension per unit length.

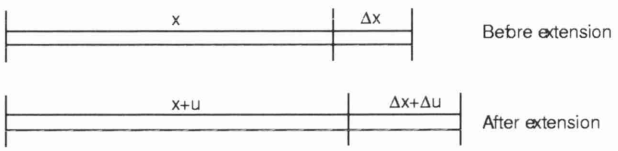

Figure D.1: *Extension of a bar due to an applied force.*

Now consider a two dimensional plate, with two orthogonal vectors $\overrightarrow{AB}_1$ and $\overrightarrow{AB}_2$ defined upon it. If this plate is then rotated, $\overrightarrow{AB}_1$ becomes $\overrightarrow{A'B'}_1$ and $\overrightarrow{AB}_2$ becomes $\overrightarrow{A'B'}_2$. (See figure D.2.) Using the notation of figure D.2, the extension per unit length parallel to x_1 is $\frac{du_1}{dx_1}$ and that parallel to x_2 is $\frac{du_2}{dx_2}$. There are also two cross terms, $\frac{du_1}{dx_2}$ and $\frac{du_2}{dx_1}$.

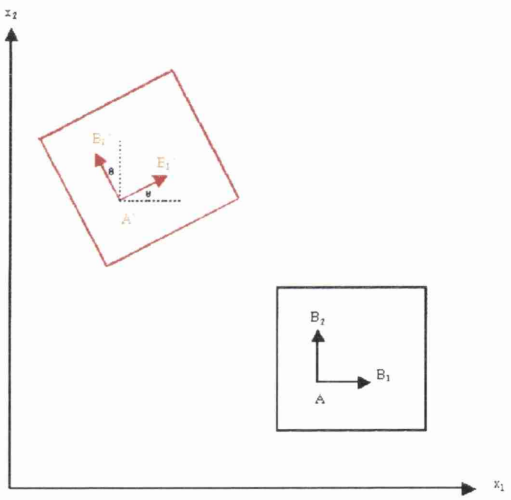

Figure D.2: *Rotation of a 2-dimensional plate.*

From this, an initial first strain tensor could take the following form:

$$\begin{pmatrix} \frac{du_1}{dx_1} & \frac{du_1}{dx_2} \\ \frac{du_2}{dx_1} & \frac{du_2}{dx_2} \end{pmatrix}$$

which for the case of pure rotation becomes

$$\begin{pmatrix} 0 & -\theta \\ \theta & 0 \end{pmatrix}$$

since it can be seen from figure D.2 that

$$\frac{du_2}{dx_1} = -\frac{du_1}{dx_2} = tan\theta \approx \theta \tag{D.2}$$

for small displacements. So, $\frac{du_1}{dx_2}$ and $\frac{du_2}{dx_1}$ signify a strain and a rotation. Pure rotation, though, should not result in any strain since no length change is produced. A better definition for strain is therefore required, one that will not confuse rotation and strain. The above tensor is antisymmetric implying that antisymmetry can be associated with pure rotation. So it is necessary to define a strain tensor as symmetric, and therefore be zero upon pure rotation (as required). A suitable definition is therefore

$$\begin{pmatrix} \frac{du_1}{dx_1} & \frac{1}{2}\left(\frac{du_1}{dx_2} + \frac{du_2}{dx_1}\right) \\ \frac{1}{2}\left(\frac{du_2}{dx_1} + \frac{du_1}{dx_2}\right) & \frac{du_2}{dx_2} \end{pmatrix}$$

The full definition of strain, which is true for small displacements, is given by equation D.3 [99]:

$$u_{ij} = \frac{1}{2}\left(\frac{du_i}{dx_j} + \frac{du_j}{dx_i}\right) \tag{D.3}$$

D.2 Strain Energy

The full energy density is given by equation D.4

$$F = \frac{Y}{1-2\sigma}\left(u_{ik}^2 + \frac{\sigma}{1+\sigma}u_{ll}u_{mm}\right) \tag{D.4}$$

Here the summation is implied, Y is the Young's modulus and σ is the Poisson's ratio of the substance under consideration. In an FEA model (in this work, Algor [81]), this equation is evaluated at each node and then integrated over the whole volume [99]. It is useful to consider the terms in this equation with respect to their physical relevance.

Two sources of energy are introduced:

- Bulk energy
- Shear energy

Bulk Energy

Consider a small cuboidal volume with sides of length L_x, L_y and L_z. The volume of this is $L_x L_y L_z$. If this volume is deformed, then the principal strains will be those in the x, y and z directions. These are

$$u_{xx} = \frac{\Delta x}{L_x}$$

$$u_{yy} = \frac{\Delta y}{L_y}$$

$$u_{zz} = \frac{\Delta z}{L_z} \tag{D.5}$$

The new volume, V', is now

$$\begin{aligned} V' &= (L_x + \Delta x)(L_y + \Delta y)(L_z + \Delta z) \\ &= (L_x + L_x u_{xx})(L_y + L_y u_{yy})(L_z + L_z u_{zz}) \\ &= L_x(1 + u_{xx})L_y(1 + u_{yy})L_z(1 + u_{zz}) \\ &= V + V u_{ll} \end{aligned} \tag{D.6}$$

Higher order terms have been ignored in this expression for the new volume. Now, since $\Delta V = V' - V$,

$$\frac{\Delta V}{V} = u_{ll} \tag{D.7}$$

Hence, the second term in equation D.4 refers to the volume change of the object.

Shear Energy

The first term in equation D.4, involving the term u_{ik}, includes the off diagonal terms. These are of the form $u_x y$, $u_y z$ and so on. These refer to shear strain, the concept of which is illustrated by figure D.3.

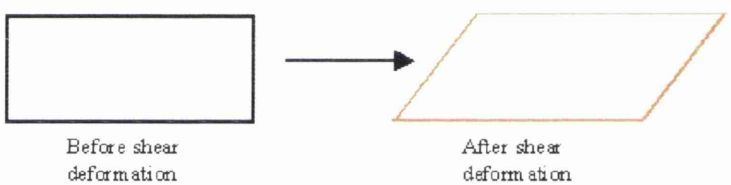

Figure D.3: *Typical shear deformation.*

This first term therefore refers to shear. However, it also has a contribution from the diagonal elements of the strain tensor because it sums over the entire tensor. In order to be able to separate the bulk and shear energies, a new term is needed, defined in equation D.8

$$S_{ij} = u_{ij} - \frac{1}{3}\delta_{ij} u_{ll} \tag{D.8}$$

This has a zero trace and allows for a new definition of energy:

$$F = \frac{1}{2} K u_{ll} u_{mm} + \mu S_{ij} S_{ij} \tag{D.9}$$

Here, K is the bulk modulus and μ is the shear modulus. These are related to the Young's modulus and Poisson's ratio by the following expressions:

$$K = \frac{1}{3}\left(\frac{Y}{1-2\sigma}\right) \tag{D.10}$$

$$\mu = \frac{1}{2}\left(\frac{Y}{1+\sigma}\right) \tag{D.11}$$

This definition is due to Landau and Lifshitz [99].

Appendix E

Creating Fused Silica Suspension Fibres

In the work discussed in Chapter 6, a sapphire test mass to which a fused silica post had been bonded was suspended by means of a monolithic fused silica suspension. In these suspensions there was at least one, and sometimes two, stages that consisted of fused silica fibres. In this appendix, the various techniques employed to create these are discussed.

All fibres are drawn from thicker, fused silica rods. These rods are heated and then pulled, increasing their length and therefore reducing their diameter. Initially, this was done by hand, using a hydrogen burning torch. This torch is shown in figure E.1. Thin rods, typically 1 mm in diameter would be held in the flame until white hot, then pulled to either side, producing thin fibres, 100 μm thick and roughly 2 cm in length. Using this technique, though, it was hard to produce fibres of consistent cross-section and length. It was also dangerous, since it required a close proximity of hand to flame. This technique was therefore abandoned in favour of the use of a manual fibre puller (figure E.2), constructed by S. McIntosh and G. Cagnoli [100].

Figure E.1: *Photo of hydrogen burner.*

To create fibres here, the initial rod was held at either end by clamps which were attached to a pulley. Nozzles spaced in a ring about the centre of the clamped rod then directed the flames (hydrogen/oxygen) to a common point, heating the rod once more. When it was white hot, the clamps were pulled apart to the required length and then the flame ring was moved aside. This produced fibres of around 25 cm in length. Typically, the fibres were pulled from 5 mm rod, leading to fibres that were around 200 μm thick. From these long fibres, small pieces could be cut (with the hydrogen torch) to the right length, then welded into the suspension, again with the torch.

A variation on this manual puller has been designed by S. McIntosh and G. Cagnoli [100] for use in creating the fused silica fibres that will suspend the test masses in GEO 600. This puller is automated - a computer programme controls the heating time and pulls the fibres. This machine has been shown to produce reproducible fibres for a given set of parameters (such as heating

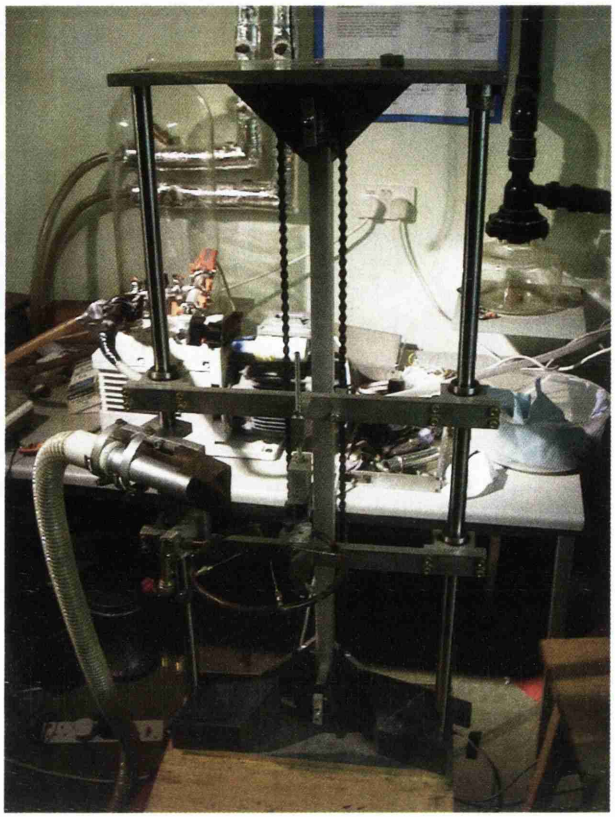

Figure E.2: *Photo of manual pulling machine.*

time and pulling strength). This is shown in figure E.3.

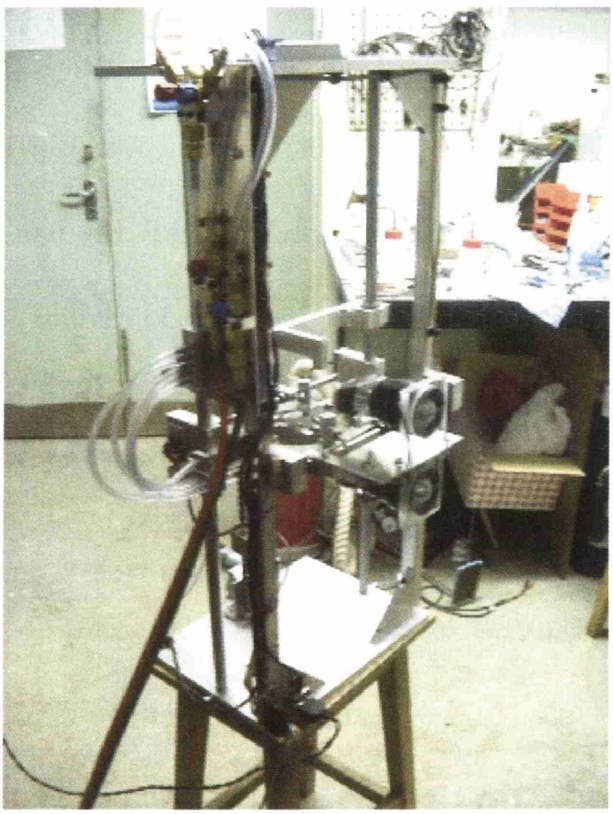

Figure E.3: *Photo of automated pulling machine.*

Bibliography

[1] A. Einstein. *Annalen der Physik*, 49:769, 1916.

[2] J. Weber. *Physical Review*, 117:306, 1960.

[3] R.A. Hulse and J.H. Taylor. *Astrophysical Journal*, 195:L51, 1975.

[4] J.A. Lobo. Sources of Gravitational Waves. *General Relativity, Proceedings of the 46th Scottish Universities Summer School in Physics, Aberdeen, Ed. G.S. Hall and J.R. Pullman*, page 203, 1995.

[5] B.F. Schutz. The Detection of Gravitational Waves. *Proceedings of the 1995 Houches School on Astrophysical Sources of Gravitational Radiation, Ed. J.A. Marck, J.P. Lasota, Springer Berlin*, 1996.

[6] B.F. Schutz. *Nature*, page 310, 1986.

[7] V. Kalogera, R. Narayan, D.N. Spergel, and J.H. Taylor. *Astrophysical Journal*, 556, 2001.

[8] K.S. Thorne. Gravitational Waves. *Proceedings of the 1994 Snowmass Summer Study on Particle and Nuclear Astrophysics and Cosmology, Ed. E.W. Kolb, R. Peccei, Word Scientific, Singapore*, 1995.

[9] R.V. Wagoner. *Astrophysical Journal*, 278:345, 1984.

[10] L. Bildsten. *Astrophysical Journal*, 501:L45, 1998.

[11] J. Hough, H. Walther, B.F. Schutz, J. Ehlers, H. Welling, I.F. Corbett, and V. Kose et al. Proposal for a Joint German-British Interferometric Gravitational Wave Detector. *Max-Planck-Institut fur Quantenoptik Report 147 and GWD/137/JH(89)*, 1989.

[12] M Tinto. *TDA Progress Report 42-132*, 1998.

[13] N.A. Robertson. Detection of Gravitational Waves. *General Relativity, Proceedings of the 46th Scottish Universities Summer School in Physics, Aberdeen, Ed. G.S. Hall, J.R. Pullman*, 1995.

[14] P. Astone, M. Bassan, P. Bonifazi, P. Carelli, E. Coccia, C. Cosmelli, V. Fafone, S. Frasca, A. Marini, G. Mazzitelli, Y. Minenkov, I. Modena, G. Modestino, A. Moleti, G.V. Pallottino, M.A. Papa, G. Pizzella, P. Rapagnani, F. Ricci, F. Ronga, R. Terenzi, M. Visco, and L. Votano. *Astroparticle Physics*, 1997.

[15] http://www.physics.uwa.edu.au/Seminars/previous.html.

[16] http://www.minigrail.nl.

[17] R.L. Forward. *Physics Review D*, 17, 1978.

[18] R. Weiss. *M.I.T. Quarterly Progress Report No. 105*, 1972.

[19] P. Saulson. *Fundamentals of Interferometric Gravitational Wave Detectors.* World Scientific, Singapore, 1994.

[20] W. Winkler. *A Michelson Interferometer Using Delay Lines in The Detection of Gravitational Waves, Ed. D.G. Blair.* Cambridge University Press, Cambridge, 1991.

[21] D. Shoemaker, R. Schilling, L. Schnupp, W. Winkler, K. Maischberger, and A. Rudiger. *Physics Review D*, 38, 1988.

[22] R.W.P. Drever, G.M. Ford, J. Hough, I.M. Kerr, A.J. Munley, J.R. Pugh, N.A. Robertson, and H. Ward. A Gravity-Wave Detector Using Optical Cavity Sensing. *Proceedings of the 9th International Conference on General Relativity and Gravitation, Jena 1980, Ed. E. Schmutzer, VEB Deutscher Verlag der Wiussenschaften, Berlin*, page 306, 1983.

[23] D. Sigg, N. Mavalvala, J. Giaime, P. Fritschel, and D. Shoemaker. *Applied Optics*, 37:5687, 1998.

[24] D.I. Robertson, E. Morrison, J. Hough, S. Killbourn, B.J. Meers, G.P. Newton, N.A. Robertson, K.A. Strain, and H. Ward. *Review of Scientific Instruments*, 66(9):4447, 1995.

[25] M. Casey. *Developments Towards Autonomous Operation of Laser Interferometric Gravitational Wave Detectors.* PhD thesis, University of Glasgow, 1999.

[26] A. Lazzarini. LIGO Project Status Update. *Rencontres de Moriond, Eds J. Tran Thanh Van, J. Dumarchez, S. Reynaud, C. Salomon, S. Thorsett, J.Y. Vinet*, pages 3–14, 1999.

[27] F. Cavalier. Status of the VIRGO Experiment. *Rencontres de Moriond, Eds J. Tran Thanh Van, J. Dumarchez, S. Reynaud, C. Salomon, S. Thorsett, J.Y. Vinet*, pages 15–20, 1999.

[28] R. Takahashi and the TAMA collaboration. TAMA 300 project: Status. *Rencontres de Moriond, Eds J. Tran Thanh Van, J. Dumarchez, S. Reynaud, C. Salomon, S. Thorsett, J.Y. Vinet*, pages 27–31, 1999.

[29] http://www.icrr.u tokyo.ac.jp/gr/LCGT.pdf.

[30] http://www.gravity.uwa.edu.au/AIGO/AIGO.html.

[31] J. Hough. LISA - the Current Situation. *Rencontres de Moriond, Eds J. Tran Thanh Van, J. Dumarchez, S. Reynaud, C. Salomon, S. Thorsett, J.Y. Vinet*, pages 45–50, 1999.

[32] K. Danzmann, A. Rudiger, R. Schilling, W. Winkler, and J. Hough et al. Max-Planck-Institut fur Quatenoptik Report MPQ 177. 1993.

[33] W.A. Edelstein, J. Hough, J.R. Pugh, and W. Martin. *Journal of Physics E: Scientific Instruments*, 11, 1978.

[34] P.R. Saulson. *Physics Review D*, 42:2437, 1990.

[35] M.V. Plissi, C.I. Torrie, M.E. Husman, N.A. Robertson, K.A. Strain, H. Ward, H. Luck, and J. Hough. *Review of Scientific Instruments*, 71(6), 2000.

[36] P.R. Saulson. *Physics Review D*, 30, 1984.

[37] R. Spero. Proceedings Los Alamos Conference 1982, ed. M.M. Nieto et al. (AIP New York). *Science Underground*, 1983.

[38] S.A. Hughes and K.S. Thorne. *Physical Review D*, 58, 1998.

[39] K.D. Skeldon, K.A. Strain, A.I. Grant, and J. Hough. *Review of Scientific Instruments*, 67:2443, 1996.

[40] B.J. Meers. *Physical Review D*, 38:2317, 1988.

[41] R.W.P. Drever. *Gravitational Radiation, Ed. N. Dereulle, T. Piran.* North Holland Publishing Co., 1983.

[42] R.Brown. *Ann. Phys. Chem.*, 14:294, 1828.

[43] A. Einstein. *Investigations on the Theory of Brownian Movement.* Dover, New York, 1956.

[44] H.B. Callen and T.A. Welton. *Physical Review*, 83:34, 1951.

[45] H.B. Callen and R.F. Greene. *Physical Review*, 86:702, 1952.

[46] S. Rowan, R. Hutchins, A. McLaren, N.A. Robertson, S.M. Twyford, and J. Hough. *Physics Leters A*, 227:153–158, 1997.

[47] C. Zener. *Elasticity and Anelasticity in Metals.* University of Chicago Press, 1948.

[48] A.P. French. *Vibrations and Waves.* M.I.T. Introductory Physics Series. Van Nostrand International, 1965.

[49] A. Gillespie. *Thermal Noise in the Initial LIGO Interferomters.* PhD thesis, California Institute of Technology, 1995.

[50] K. Yamamoto. *Study of the thermal noise caise by inhomogeneously distributed loss.* PhD thesis, University of Tokyo, 2000.

[51] Y. Levin. *Physics Review D*, 57:659, 1998.

[52] Y.T. Liu and K.S. Thorne. *Physics Review D*, 62:12202, 2000.

[53] V.B. Braginsky, M.L. Gorodetsky, and S.P. Vyatchanin. *Physics Letters A*, 264, 1999.

[54] G. Cagnoli, J. Hough, D. Debra, M.M Fejer, E. Gustafson, S. Rowan, and V. Mitrofanov. *Physics Letters A*, 272:39–45, 2000.

[55] J.E. Logan, J. Hough, and N.A. Robertson. *Physics Letters A*, 183:145, 1993.

[56] G.I. Gonzalez and P.R. Saulson. *Journal of Acoustic Society of America*, 96:207, 1994.

[57] S. Rowan, S.M. Twyford, J. Hough, D.-H. Gwo, and R. Route. *Physics Leters A*, 246:471–478, 1998.

[58] Sheila Rowan, private communication.

[59] J.E. Logan, N.A. Robertson, and J. Hough. *Physics Letters A*, 170:352–358, 1992.

[60] V.B. Braginsky, V.P. Mitrofanov, and V.I. Panovo. *Systems with Small Dissipations.* University of Chicago Press.

[61] A.S. Nowick and B.S. Berry. *Anelastic Relaxation in Crystalline Solids.* Materials Science Series. Academic Press, 1972.

[62] W. Winkler, K. Danzmann, A. Ruediger, and R. Schilling. *Physical Review A*, 44(11):7022–7036, 1991.

[63] S.M. Twyford. PhD thesis, University of Glasgow, University of Glasgow, University Avenue, G12 8QQ, September 1998.

[64] W.J. Startin, M.A. Beilby, and P.R. Saulson. *Review of Scientific Instruments*, 69:3681, 1998.

[65] S.D. Penn, G.M. Harry, A.M. Gretarsson, S.E. Kittelberger, P.R. Saulson, J.J. Schiller, J.R. Smith, and S.O. Swords. *Review of Scientific Instruments*, 72(9):3670, 2001.

[66] H. Luck. The status of GEO 600. *Rencontres de Moriond, Eds J. Tran Thanh Van, J. Dumarchez, S. Reynaud, C. Salomon, S. Thorsett, J.Y. Vinet*, pages 21–24, 1999.

[67] C. Boccara and V. Loriette. Virgo note (1993). *VIR-NOT-PCI-1380-65.*

[68] http://www.crysys.com/hem.html.

[69] M. Taniwaki, L. Ju, D.G. Blair, and M.E. Tobar. *Physics Letters A*, 246:37–42, 1998.

[70] L. Ju, M. Notcutt, D. Blair, F. Bondu, and C.N. Zhao. *Physics Letters A*, 218:3–6, 1996.

[71] B. Auld. *Acoustic Fields and Waves in Solids, Vol II.* J. Wiley and sons, 1993.

[72] RS Components Limited, PO Box 99, Corby, Northamptonshire, NN17 9RS.

[73] Corning Incorporated, 3997 McMann Road, Cincinnati, OH 45245.

[74] Heraeus Silica and Metals Limited, 1 Craven Court, Canada Road, Byfleet, Surrey KT14 7JL.

[75] Sheila Rowan, private communication.

[76] Crystal Systems, 27 Congress Street, Salem, MA 01970.

[77] Jim Hough, private communication.

[78] General Optics Inc. now WavePrecision Inc., 5390 Kazuko Court, Moorpark, CA USA 93021.

[79] Goodfellow Cambridge Limited, Cambridge Science Park, Cambridge, CB4 4DJ.

[80] G.W. McMahon. *Journal of Accoustical Society of America*, 36:85, 1964.

[81] Algor Inc., 159 Beta Drive, Pittsburgh, PA 15238-2932 USA.

[82] K. Srinivasan, D. Coyne, and R. Vogt. *LIGO document no LIGO-T97016-00-D*, 1997.

[83] Eds. R.W. Waynant and M.N. Ediger. *Electro-optics Handbook.* McGraw Hill Inc., 1994.

[84] S. Musikant. *Optical Materials.* Marcel Dekker Inc., 1985.

[85] D. Crooks, P. Sneddon, G. Cagnoli, J. Hough, S. Rowan, M. Fejer, E. Gustafson, R. Route, and N. Nakagawa. *In press.*

[86] N. Nakagawa, B.A. Auld, E.K. Gustafson, and M.M. Fejer. *Review of Scientific Instruments*, 68:3553, 1997.

[87] F. Bondu, P. Hello, and J.-Y. Vinet. *Physics Letters A*, 246:227–236, 1998.

[88] N. Nakagawa, A.M. Gretarsson, E.K. Gustafson, and M.M. Fejer. *submitted to Phys. Rev. D.*

[89] Advanced LIGO Systems Design, LIGO Scientific Collaboration, ed. P. Fritschel, LIGO-T010075-00-D, 27 June 2001.

[90] Jim Hough, private communication.

[91] Research Electro-optics Inc, 1855 South 57th Court, Boulder, Colorado, US.

[92] David Crooks, private communication.

[93] S. Buchman, F. Everitt, B. Parkinson, J. Turneaure, M. Keiser, M. Taber, D. Bardas, J. Lockhart, B. Muhlfelder, J. Mester, Y.M. Xiao, G. Gutt, D. Gill, R. Brumley, and B. Didonna. *Classical and Quantum Gravity*, 13, 1996.

[94] D.H. Gwo. *Proceedings of SPIE - The International Society for Optical Engineering*, 3435, 1998.

[95] Jim Hough, private communication.

[96] Stanford Research Systems Inc, 1290-D Reamwood Avenue, Sunnyvale California 94089.

[97] Graphtec (GB)Ltd, Suite 3i Redwither Tower, Redwither Business Park, Wrexham LL13 9XT.

[98] http://www.ni.com.

[99] L.D. Landau and E.M. Lifshitz. *Theory of Elasticity.* Pergamon, Oxford, 3rd edition, 1986.

[100] S. McIntosh. PhD thesis, University of Glasgow, University of Glasgow, University Avenue, G12 8QQ, In preparation.